ABSTRACT

Title of dissertation: Modeling strong-field laser-atom interactions with nonlocal potentials

T. C. Rensink, Doctor of Philosophy, 2017

Dissertation directed by: Professor T. M. Antonsen, Jr.
Department of Physics

Atom-field interactions in the ionization regime give rise to a wide range of physical phenomena, and their study continues to be an active field of research. However, simulation of atom-field dynamics is time-consuming and computationally expensive. In this thesis, a nonlocal model potential is used in place of the Coulomb potential in the time dependent Schrodinger equation, and examined for suitability of modeling strong field-atom dynamics while offering significant reduction in computation cost.

Nonlocal potentials have been used to model many physical systems, from multi-electron molecular configurations to semiconductor theory. Despite their relative success, nonlocal potentials have been largely unexplored for modeling high field laser-gas interactions in the ionizing regime. This work explores the theory and numerical results of a single state gaussian nonlocal model in intense, femtosecond laser pulses, with the main findings: nonlocal potentials are useful for obtaining the photoionization rate in the tunnel and multiphoton regimes, and qualitatively characterize the wavefunction dynamics of irradiated atoms. The model is also examined

in the context of the two-color technique for producing Terahertz (THz) frequency radiation.

Modeling strong-field laser-atom interactions with nonlocal potentials

by

Thomas C. Rensink

Dissertation submitted to the Faculty of the Graduate School of the
University of Maryland, College Park in partial fulfillment
of the requirements for the degree of
Doctor of Philosophy
2017

Advisory Committee:
Professor T. M. Antonsen, Jr., Chair/Advisor
Professor Ki-Yong Kim, Dean's Representative
Professor Philip Sprangle
Professor Rajarshi Roy
Professor Mohammad Hafezi

Dedication

To my wife, Iris, and my family. I am fortunate to have such warm, passionate, and talented people in my life.

Acknowledgments

This work could not have been done without the help and support of several people to whom I owe a debt of gratitude.

To my advisor, Professor Tom Antonsen: I could not have completed this work without your wisdom, and seemingly boundless technical skill. It was a privilege to have access to your thoughts, time, and colossal talent, balanced only by your patience and accessibility. Thanks Tom!

To my colleagues, with whom I learned alongside and from whose inspiration I benefitted: in the classroom and in the office, I am reminded that we walk the path faster together than alone. A special thanks to John Palastro, Luke Johnson, Prof. Phil Sprangle, Chenlong Miao, Jasmine (Wenxi) Zhu, and the other faculty and students at the Institute for Research Electronics and Applied Physics (IREAP).

To Dan Gordon at the Naval Research Laboratory, a thank you for providing the turboWAVE code for the *ab initio* simulations that were crucial for this work.

And finally, to my "Seven Seas and associates" friends and fellow graduates: your camaraderie, wit, humor, and morale helped make the graduate experience at the University of Maryland what it was - singular and memorable!

Sincerest thanks to all of you.

Table of Contents

List of Tables

List of Figures

List of Abbreviations

ADK:	Ammosov, Delaine, and Krainov (ionization rate model, [1])
$\mathscr{F}\{\}$:	Fourier transform
FDTD:	finite-difference time-domain (numerical technique)
HHG:	high harmonic generation
PCM:	photocurrent model (of THz radiation generation)
PMPB:	Poprhuzhenko, Mur, Popov, and Bauer (ionization rate model, [2])
SFA:	strong field approximation
TDSE:	time-dependent Schrödinger equation
turboWAVE:	*ab initio* finite-difference time-domain (FDTD) numerical time-dependent S

Chapter 1: Introduction

With the invention of the laser in 1960 and later chirped pulse amplification (CPA) in 1985 [5], research in the domain of matter interacting with intense electromagnetic radiation increased dramatically. In recent decades, continued refinements in lasers systems have given rise to increased peak field and power (now at petawatt class), decreased pulse durations (now at attosecond timescales), and ever wider lasing frequencies, including growing interest in the mid-infrared regime and frequency tunable lasers (e.g. the free electron laser). Active areas of research currently being pursued with such experimental apparatus are too broad to summarize, but a few examples include: electron and ion acceleration [6–8], THz frequency radiation generation [3, 9–11], high harmonic generation [12, 13], and the attosecond atom-field dynamics [14, 15], among many others. Interest in this research is driven by applications that range just as widely, from military defense and radiation detection to medical imaging. Theoretical modeling and simulation work in the strong field regime have progressed alongside such experimental systems. Usually, strong-field phenomena are explored in two distinct regimes: the "microscopic" regime, where the detailed description of a single atom or molecule is examined in the presence of a prescribed strong electromagnetic field with no back-reaction, and a "macro-

scopic" regime, concerned with modeling the large scale dynamical evolution of the laser pulse in a (usually) transparent medium that responds to and modifies the laser pulse. Phenomena within each regime are usually categorized according to the electric field strength: nonlinear optics giving a perturbative description of material in the (relatively) weak electric field strength regime, while photo-ionization often becomes a dominant process in the strong (electric) field regime. Owing to the disparity in length and time scales between the two regimes are generally not treated in a unified manner. The approach presented in this thesis is a first step in this direction.

1.1 Microscopic description of atom-field interactions

Modeling microscopic atom-field interactions can be studied using various quantum mechanical formalisms. The time-dependent Schrödinger (TDSE) equation is one of the most employed models, providing a quantum mechanical description of the (spinless) electron wavefunction interacting with a classical laser potential ($\Phi(\mathbf{x},t)$, $\mathbf{A}(\mathbf{x},t)$) and atomic potential V_{atom}:

$$i\hbar\partial_t\psi(\mathbf{x},t) = \left(-\frac{\hbar^2}{2m_e}\left(\nabla + q_e\mathbf{A}(\mathbf{x},t)\right)^2 - q_e\Phi(\mathbf{x},t) + V_{atom}(\mathbf{x})\right)\psi(\mathbf{x},t). \qquad (1.1)$$

At intensities of 10^{12} to 10^{15} W cm^{-2} the TDSE gives an accurate description of processes such as photo-ionization, atomic polarization, and electron rescattering. Many numerical treatments exist for solution of the TDSE, including finite-difference time domain (FDTD) numerical solutions [4] and Floquet and eigenfunction expansion schemes [16, 17]. At ultraviolet frequencies, or intensities above $\sim 10^{15}$ W

cm^{-2}, double ionization becomes important. Relativistic effects become important at intensities of 10^{18} W cm^{-2}. In these regimes different wave mechanical descriptions are more appropriate, such as the Lorentz invariant Klein-Gordon equation. Density Functional Theory (DFT) and time-dependent Density Functional Theory (TDDFT) are often used for modeling more complex molecular geometries, and electron-electron interactions [17, 18]. For the purpose of this thesis, we restrict our interest to the non-relativistic, single active electron regime, corresponding roughly to intensities from 10^{13}-10^{15} W cm^{-2}, from infrared through ultraviolet frequencies.

1.2 Macroscopic description of atom-field interactions

The macroscopic temporal and spatial evolution of the electric field $\mathbf{E}(\mathbf{x}, t)$ and magnetic field $\mathbf{B}(\mathbf{x}, t)$ are determined by Maxwell's equations in SI:

$$\nabla \cdot \mathbf{E}(\mathbf{x}, t) = \rho(\mathbf{x}, t)/\epsilon_0 \tag{1.2a}$$

$$\nabla \cdot \mathbf{B}(\mathbf{x}, t) = 0 \tag{1.2b}$$

$$\nabla \times \mathbf{E}(\mathbf{x}, t) = -\partial_t \mathbf{B}(\mathbf{x}, t) \tag{1.2c}$$

$$\nabla \times \mathbf{B}(\mathbf{x}, t) = \mu_0(\mathbf{J}(\mathbf{x}, t) + \epsilon_0 \partial_t \mathbf{E}(\mathbf{x}, t)) \tag{1.2d}$$

where the response of the medium enters through the source terms of the charge density ρ and current density $\mathbf{J}$. In the macroscopic regime, the time and space varying (microscopically averaged) source terms are the key quantities to calculate. Relevant effects are often characterized by a spatially local, frequency dependent polarizability. In the weak field limit, the response of the medium is represented by

an expansion in powers of the electric field, where

$$\begin{aligned}\mathbf{P}_j(\omega) = {} & \epsilon_0\chi^{(1)}_{jk}(-\omega;\omega)\mathbf{E}_k(\omega)+ \\ & \epsilon_0\chi^{(2)}_{jkl}(-\omega;\omega_1,\omega_2)\mathbf{E}_k(\omega_1)\mathbf{E}_l(\omega_2)+ \\ & \epsilon_0\chi^{(3)}_{jklm}(-\omega;\omega_1,\omega_2,\omega_3)\mathbf{E}_k(\omega_1)\mathbf{E}_l(\omega_2)\mathbf{E}_m(\omega_3)+\ldots .\end{aligned} \tag{1.3}$$

where we have used indices j, k, l, m to represent cartesian indices for the susceptibility tensors $\chi^{(n)}$, and the frequency components of each field amplitude $\mathbf{E}(\omega_n)$ are required to sum to the frequency ω. Equation (1.3) is written generally; the second order term is zero for media composed of centro-symmetric (atomic) potentials. The third order nonlinearity is responsible for many phenomena, including third harmonic generation, self-phase modulation (optical Kerr effect, or nonlinear index of refraction), and two-photon absorption [19]. In addition to the rapid electronic contribution to the polarizability, there is a slower "delayed" Raman polarization associated with the motion of the nuclei. Provided the power of the laser pulse is above the "critical power", the Kerr effect causes self-focusing to occur, dynamically balancing the defocussing plasma response; the resulting filamentation permits high intensity radiation to propagate much farther than a diffraction limited pulse. Excellent summaries of propagation effects and numerical methods for treating propagation can be found in several sources, [19–25].

In principle, Eqs.(1.1) and (1.2) are coupled and should be solved simultaneously. This requires expressing the macroscopic current density, $\mathbf{J}(\mathbf{x}, t)$, as a function of space and time. Here we assume this can be represented by the microscopic current generated by the single electron wavefunction of an atom centered at

$\mathbf{x}_0$ weighted by the local gas density n_0:

$$\mathbf{J}(\mathbf{x}_0, t) = n_0(\mathbf{x}_0)\langle \mathbf{j}(\mathbf{x}_0, t)\rangle = n_0(\mathbf{x}_0) q_e \partial_t \int d^3\mathbf{x}' \; \mathbf{x}' |\psi(\mathbf{x}', t)|^2 \tag{1.4}$$

where $\mathbf{x}'$ is the coordinate system for an atom centered at $\mathbf{x}_0$. In principle, an averaging process should be employed to express the contribution of an ensemble of microscopic currents as a reasonably smooth macroscopic current density. This will not be addressed here and is discussed elsewhere [26, 27].

In practice, however, although there have been a few attempts [27, 28], a coupled Maxwell-Schrödinger solver with the equations above is largely beyond the scope of current computing capabilities at the time of this writing. The system (1.1), (1.3), and (1.2) represent a 6 + 1 dimensional vector integro-differentiation equation with disparate time scales. Relevant time scales of atomic processes and typical laboratory parameters are summarized in table 1.1 and 1.2. Performing such simulations over a macroscopic simulation domain with temporal resolution needed for both the atomic and optical time scales renders the problem computationally intractable using the Schrödinger solvers previously mentioned.

Despite the inability to simulate the atomic response with a field equation, the quantum mechanical nature of ionization must be taken into account, as tunnel ionization is intrinsically quantum mechanical. This is usually facilitated with one of various ionization rate formulas. The earliest work is credited to Landau, who solved for the tunneling rate of the electron in a strong DC electric field. In 1964 Keldysh published a seminal work on ionization [29], whereby he identified the two relevant regimes as tunnel and multiphoton, characterized by an adiabaticity

Table 1.1: Atomic units (a.u.)

Quantity	Value	Formula
Bohr radius (a_0)	5.3×10^{-11} m	$\hbar/(m_e c\alpha)$
Hartree energy (E_h)	27.2 eV	$\alpha^2 m_e c^2$
atomic timescale	2.4×10^{-17} s	$\hbar/E_h$
atomic field	5.14×10^{11} V/m	$E_h/(ea_0)$

parameter (Keldysh parameter)

$$\gamma \equiv \omega_0 (2m_e E_0)^{1/2}/e|\mathbf{F}_0| \tag{1.5}$$

in terms of the laser frequency ω_0, ionization potential E_0, and electric field magnitude $|\mathbf{F}_0|$. This can be understood as the ratio of the tunnel time to the laser period; for $\gamma << 1$ (the adiabatic regime), ionization is dominated by the tunneling process, while $\gamma >> 1$ is the multi-photon regime in which the ionization rate has strong dependence on the number of absorbed photons to overcome the ionization potential. These have characteristic field dependence $\exp\left(-2(2E_0)^{3/2}/(3\,|\mathbf{F}_0|)\right)$ and $\mathbf{F}_0^{2n}$, where $n \equiv \text{floor}\,(E_0/(\hbar\omega_0)) + 1$ respectively. Further refinements were made by Perelomov, Popov, and Terent'ev [30], with expressions for photoelectron momentum and energy spectra. A "Coulomb corrected" tunnel ionization rate model was given by Ammosov Delone and Krainov (ADK) in the 1980s [1], providing a prefactor to account for ionization enhancement of the Coulomb potential compared with that of short range potentials, as originally considered in Keldysh's work. Current

Table 1.2: (micro) simulation scale (I = 2×10^{14} W/cm^2, λ = 800 nm, τ = 40 fs)

Dimension	Value	Formula
free electron excursion	1.2×10^{-9} m	$q_e\|\mathbf{F}_0\|/(m_e\omega_0^2)$
energy (800 nm photon)	1.55 eV	$\hbar\omega$
laser pulse duration	4×10^{-14} s	-
field strength	4×10^{10} V/m	-

ionization rates are valid for any value of the Keldysh parameter, connecting the tunnel and multi-photon regimes [2] for a monochromatic field. To the knowledge of the author, there are no current ionization models capable of describing multi-color or broadband frequency content.

1.3 Nonlocal potentials in the Schrödinger equation

Nonlocal potentials (sometimes referred to as pseudo-potentials) were first examined by Fermi and others in the early years of quantum mechanics. They have since become a useful tool for modeling quantum mechanical systems in a variety of fields, including: quantum chemistry, semiconductor theory, nuclear theory, and solid-state physics. Although nonlocal potentials appear in various forms throughout the literature, the basic form of a nonlocal potential acting on an electron

wavefunction, as it would appear in the Hamiltonian of the Schrödinger equation is:

$$\hat{V}_{nl}\psi(\mathbf{x},t) = u(\mathbf{x})\int d^3\mathbf{x}' u(\mathbf{x}')\psi(\mathbf{x}',t), \tag{1.6}$$

often written bra-ket notation,

$$\hat{V}_{nl}|\psi\rangle = \langle u|\psi\rangle|u\rangle \tag{1.7}$$

where u is an introduced shape function that must be specified.

In the context of strong field atom interactions, we examine the Schrödinger equation in which the Coulomb potential is replaced with a model gaussian nonlocal potential. One of the main benefits is that this permits, for reasons discussed later, rapid evaluation of the wavefunction and expectation values, thus providing an efficient tool that characterizes many quantum mechanical atom-field phenomena in the microscopic regime. Such a tool is, for practical considerations, a significant step towards creating an integrated framework for solving the Maxwell-Schrödinger system of equations that would contain a complete description of the microscopic quantum phenomena as well as the macroscopic laser-pulse evolution effects.

Although there are formal connections between the nonlocal potential and local potentials, which will be explored towards the end of this work, the model presented in this thesis is largely a heuristic tool that captures many of the desired properties of atomic potentials if properly tuned. The efficiency the model provides for investigating a wide array of atom-field interactions must be weighed against the reality that there some properties of a local potential are not closely reproduced with the heuristic model introduced here.

1.4 Thesis overview

Chapter 2 is devoted to introducing the gaussian nonlocal model in configuration space, proceeding with analysis using the Green's function method to find expressions for the bound probability, ionization rate, and dipole moment. Results are compared against an ionization rate model and a finite difference time-domain *ab initio* Schrödinger simulation. Chapter 3 explores the effect of the gauge dependence of this model, and explores analytical and numerical results produced by the model in different gauges. Analysis is done in momentum space, greatly simplifying algebraic manipulation to arrive at useful expressions. Predictions of the model are explored for a wider range of laser frequency and intensity values. The nonlocal binding potential is used in Ch. 4 to examine the microscopic theory of two-color THz generation, which is compared with a semiclassical photocurrent model and *ab initio* TDSE simulation. This provides additional insight into the gaussian model features and limitations. A formal connection between local and nonlocal potentials is investigated in Ch. 5, as well as some extensions of the simple gaussian model previously examined. Chapter 6 gives a closer look at the numerical treatment of the nonlocal model that allows for rapid and accurate evaluation. Chapter 7 concludes this work, giving a summary of the most important findings of using nonlocal potentials to investigate high-field phenomena.

Chapter 2: Introduction to the gaussian nonlocal potential

2.1 Formulation

The work that follows in this chapter is summarized in the peer-reviewed publication [31]. For a more straightforward algebraic introduction to the nonlocal model, see chapters 3 and 5. The 3D TDSE for a single electron under the influence of a Coulomb potential and subject to a time varying electric field $\mathbf{E}(t)$ in the dipole approximation is:

$$i\hbar\frac{\partial}{\partial t}\psi(\mathbf{r},t) = \left[-\frac{\hbar^2}{2m_e}\nabla^2 - \frac{Ze^2}{|\mathbf{r}|} + e\mathbf{E}(t)\cdot\mathbf{r}\right]\psi(\mathbf{r},t). \tag{2.1}$$

The gaussian nonlocal potential model is formulated by replacing the Coulomb potential in Eq.(2.1) with a nonlocal potential term:

$$-\frac{Ze^2}{|\mathbf{r}|}\psi(\mathbf{r},t) \to -Vu(\mathbf{r})S(t),$$

where

$$u(\mathbf{r}) \equiv \left(\pi\sigma^2\right)^{-3/4}\exp\left(-\mathbf{r}^2/2\sigma^2\right), \tag{2.2a}$$

$$S(t) \equiv \int \mathrm{d}^3\mathbf{r}\; u(\mathbf{r})\psi(\mathbf{r},t). \tag{2.2b}$$

Here $u(\mathbf{r})$ defines the spatial extent of the binding potential, while $S(t)$, being the overlap of the wavefunction with $u(\mathbf{r})$ is the "nonlocal" portion of the potential.

Using the shorthand notation $\langle f(\mathbf{r})|g(\mathbf{r})\rangle \equiv \int \mathrm{d}^3\mathbf{r}\, f(\mathbf{r})g(\mathbf{r})$, it can be seen from Eq.(2.2a) that $u(\mathbf{r})$ is a normalized function such that $|\langle u|u\rangle|^2 = 1$ and $S(t) = \langle u(\mathbf{r})|\psi(\mathbf{r},t)\rangle$ is the projection of the time-dependent wavefunction onto $u(\mathbf{r})$. We have introduced two free parameters with the above definitions: V, the normalized binding energy, used to change the overall strength of the binding potential, and σ, the spatial extent of the binding potential. These may be chosen to match the ionization properties of atomic Hydrogen, as will be seen later.

It is not immediately apparent that an electron in a nonlocal potential responds in a similar way to applied fields as one in a local potential, and a few comments are in order to motivate this substitution. In the limit $\sigma \to 0$, $u(\mathbf{r})$ becomes a delta function and the nonlocal potential recovers the familiar local potential term, $-\lambda\delta^3(\mathbf{r})\psi(\mathbf{r},t)$; while the delta potential has been considered in 1D treatments of Eq.(2.1) [32], the 3D extension produces solutions to $\psi(\mathbf{r})$ that are singular at the origin. The nonlocal potential can be considered one modification of the 3D delta function that permits normalizable solutions of the wavefunction. The nonlocal model retains many essential properties of local potential systems: it is Hermitian, norm-preserving, and linear in $\psi(\mathbf{r},t)$. However, the system no longer exhibits gauge invariance in the usual interpretation that is exhibited by local potentials; this is an important difference that is addressed at length in chapter 3. For simplicity, all equations and mathematical expressions in this chapter use the following normalization convention unless otherwise specified: $\mathbf{r}/\sigma \to \mathbf{r}$, $\hbar t/m_e\sigma^2 \to t$, $m_e\sigma^2 V/\hbar^2 \to V$, and $\sigma^3 m_e e\mathbf{E}(t)/\hbar^2 \to \mathbf{E}(t)$. These are identical to atomic units, except that all dimensions of length are scaled to the introduced gaussian width,

σ, in place of the Bohr radius (as used in atomic units); this convention produces the simplest algebraic expressions. It should be noted that standard atomic units (scaled to the Bohr radius) are used in later chapters. Below are the previously defined quantities in the normalized coordinates, as well as the modified TDSE; together, these define the system we wish to solve for a general time-dependent electric field, $\mathbf{E}(t)$:

$$u(\mathbf{r}) = \pi^{-3/4} \exp\left(-\mathbf{r}^2/2\right), \tag{2.3a}$$

$$S(t) = \int \mathrm{d}^3\mathbf{r}\, u(\mathbf{r})\psi(\mathbf{r},t), \tag{2.3b}$$

$$i\frac{\partial}{\partial t}\psi(\mathbf{r},t) = \left[-\frac{1}{2}\nabla^2 + \mathbf{r}\cdot\mathbf{E}(t)\right]\psi(\mathbf{r},t) - Vu(\mathbf{r})S(t). \tag{2.3c}$$

2.2 Green's function solution

In principle, the system given by Eqs.(2.3) could be simulated directly by time evolving the modified Schrödinger equation with a finite-difference [33], finite-volume[4], spectral method [17] or a variety of other numerical treatments, and quantities of interest could be obtained through the usual prescription of operators acting on the wavefunction. This would be a computational task essentially equal to solving the original TDSE, with no advantage gained by using the modified binding potential; the gaussian nonlocal potential, however, offers a considerably more efficient method for obtaining such quantities. Specifically, we reduce the system given by Eqs.(2.3) to an integral equation in time for $S(t)$ without explicitly calculating $\psi(\mathbf{r},t)$. Quantities of interest, such as the dipole moment $\mathbf{d}(t)$ and the bound probability of the electron can, in turn, be derived directly in terms of $S(t)$,

thereby eliminating the need to solve for the wavefunction altogether.

The computational savings of the nonlocal model are a direct result of the fact that no spatial representation for $\psi(\mathbf{r}, t)$ is required to be calculated to obtain information about the system. By contrast, a typical finite volume treatment of the TDSE calculates $\psi(\mathbf{r}, t)$ on a spatial grid and evolves it at each point in space over time. Accurate calculation of $\langle \mathbf{r}(t) \rangle$ requires the spatial domain to be large enough to capture free-wavefunction excursions on the order of the quiver radius $r_q = e|E_L|/m_e\omega_L^2$ (where ω_L and E_L are the frequency and amplitude of the applied field respectively) while maintaining sufficient spatial resolution to resolve the wavefunction of large momentum states. The time domain must resolve the period of the quantum bound state (typically sub-femtosecond), while extending over the duration of the laser pulse simulation, often on the order of hundreds of femtoseconds. While still subject to the same time domain constraints, the nonlocal approach lifts the restrictions in the spatial domain entirely, as will be seen.

A Green's function (or propagator) approach will be used to obtain the integral equation for $S(t)$. We first define $G(\mathbf{r}, t; t')$ as the solution to the equation

$$\left[i\frac{\partial}{\partial t} + \frac{1}{2}\nabla^2 - \mathbf{r} \cdot \mathbf{E}(t) \right] G(\mathbf{r}, t; t') = iu(\mathbf{r})\delta(t - t'), \tag{2.4}$$

where we have taken Eq.(2.3c) and replaced $-VS(t)$ by an impulse in the time domain, $i\delta(t - t')$, and the boundary condition is taken to be $G(\mathbf{r}, t < t'; t') = 0$. Because the electric potential term $-\mathbf{r} \cdot \mathbf{E}(t)$ is linear in space, Eq.(2.4) admits a

closed form solution,

$$G(\mathbf{r},t;t') = \frac{1}{\pi^{3/4}\left[1+i(t-t')\right]^{3/2}}\times \\ \exp\left[i\mathscr{S}_0 + i\mathbf{v}_0\cdot(\mathbf{r}-\mathbf{r}_0) - \frac{|\mathbf{r}-\mathbf{r}_0|^2}{2+2i(t-t')}\right]. \tag{2.5}$$

The function $G(\mathbf{r},t;t')$ depends on the trajectories of a classical electron, designated with subscript "o", subject to field $\mathbf{E}(t)$. Here, $\mathbf{r}_0(t;t')$, $\mathbf{v}_0(t;t')$, and $\mathscr{S}_0(t;t')$, represent the position, velocity, and action of a classical electron, related through the coupled ordinary differential equations with associated initial conditions:

$$\frac{\mathrm{d}\mathbf{r}_0}{\mathrm{dt}} = \mathbf{v}_0(t), \tag{2.6a}$$

$$\frac{\mathrm{d}\mathbf{v}_0}{\mathrm{dt}} = -\mathbf{E}(t), \tag{2.6b}$$

$$\mathscr{S}_0(t,t') \equiv \int_{t'}^{t} \mathrm{dt}''\left[\,\tfrac{1}{2}\mathbf{v}_0^2(t'') - \mathbf{r}_0(t'')\cdot\mathbf{E}(t'')\right], \tag{2.6c}$$

where

$$\mathbf{v}_0(t=t';t') = \mathbf{r}_0(t=t';t') = 0. \tag{2.6d}$$

Conceptually, these trajectories describe the path of an electron "born" at the origin with zero initial velocity at t' and subsequently moving under the force of the electric field until t. With the function $G(\mathbf{r},t;t')$ defined by Eq.(2.4) and Eq.(2.5) we can express the wavefunction as a convolution,

$$\psi(\mathbf{r},t) = iV\int_{-\infty}^{t} \mathrm{dt}' G(\mathbf{r},t;t')S(t'). \tag{2.7}$$

To make use of this expression for $\psi(\mathbf{r},t)$, $S(t')$ must be known on the interval $-\infty < t' \leq t$. For problems of interest, we will assume that the wavefunction is in the bound state and $\mathbf{E}(t) = 0$ for $t \leq 0$: this constraint is sufficient to obtain an

analytic expression for $S(t' < 0)$, as shown in the next section. For $t > 0$ (after the field is present) values of $S(t')$ are calculated with a general expression, obtained in the following way: on inserting Eq.(2.7) into Eq.(2.3b) and integrating over all space, an integral equation in time for $S(t)$ for general field $\mathbf{E}(t)$ is given by

$$S(t) = i2^{3/2}V\int_{-\infty}^{t} \mathrm{d}t' S(t') \frac{\exp\left[i\mathscr{S}_0(t,t') + \Lambda(t,t')\right]}{\left[2 + i(t-t')\right]^{3/2}}, \tag{2.8}$$

where

$$\Lambda(t,t') \equiv \frac{1 + i(t-t')}{2 + i(t-t')} \frac{|\mathbf{r}_0 - i\mathbf{v}_0|^2}{2} - \frac{1}{2}|\mathbf{r}_0|^2.$$

Equation (2.8) will be used to calculate the time dependence of all quantities of interest, including the dipole moment and $\psi(\mathbf{r}, t)$ via Eq.(2.7), and as such is the primary computational task in the nonlocal model. The time savings over typical TDSE treatments is manifest by the absence of any spatial dependence in Eq.(2.8). One might protest that we've traded the problem of a large spatial simulation domain for an infinite time integral, but solving for $S(t)$ via Eq.(2.8) is more tractable than it might seem: as with Eq.(2.7), the explicit form of $S(t')$ on $-\infty < t' \leq 0$ is obtained with the condition that the electron is bound on this interval, while subsequent values of $S(t)$ can be calculated numerically via Eq.(2.8).

2.3 Properties of the nonlocal model

2.3.1 field free system

To better understand the nonlocal potential, we first examine the system in the absence of an applied field. For $\mathbf{E}(t) = 0$, the nonlocal potential admits a

single bound state $\psi_0(\mathbf{r})$ with energy E_0 that can be determined as follows: With no applied field, classical variables $\mathbf{r}_0(t,t')$, $\mathbf{v}_0(t,t')$ and $\mathscr{S}_0(t,t')$ in Eqs.(2.6) are identically zero, and Eq.(2.8) simplifies to a convolution whose kernel depends only on the time difference $(t-t')$,

$$S(t) = i2^{3/2}V \int_{-\infty}^{t} \mathrm{dt}' \frac{S(t')}{[2+i(t-t')]^{3/2}}. \tag{2.9}$$

Solutions of Eq.(2.9) are of the form $S(t) = S_0 e^{-iE_0 t}$, where S_0 is a complex constant. Inserting this expression into Eq.(2.9) results in a transcendental equation for the energy E_0 given by

$$V = \frac{1}{4}\left[1 - \sqrt{2\pi|E_0|}e^{2|E_0|}\mathrm{erfc}(\sqrt{2|E_0|})\right]^{-1}. \tag{2.10}$$

The expression in Eq.(2.10) is plotted in Fig.2.1(a). Sufficiently large values of V correspond to a single bound state wavefunction of the form $\psi(\mathbf{r},t) = \psi_0(\mathbf{r})e^{-iE_0 t}$ and eigenvalue E_0. An expression for the bound state wavefunction can be found by inserting Eq.(2.5) into Eq.(2.7) with $\mathbf{r}_0, \mathbf{v}_0, \mathscr{S}_0 = 0$ and $S(t) = S_0 e^{-iE_0 t}$ to give

$$\psi_0(\mathbf{r}) = i\frac{S_0 V}{\pi^{3/4}} \int_0^{\infty} \mathrm{dt}' \, \frac{e^{iE_0 t'}}{[1+it']^{3/2}} \exp\left[\frac{-|\mathbf{r}|^2}{2+2it'}\right]. \tag{2.11}$$

The profile of $\psi_0(\mathbf{r})$ is plotted in Fig.2.1 (b) alongside $u(\mathbf{r})$ for comparison.

2.3.2 atomic dipole moment

With the ultimate goal of finding the polarization density in mind, we seek a computationally efficient expression for the atomic dipole $\mathbf{d}(t) = -\langle \mathbf{r}(t) \rangle$ expressed in terms of $S(t)$ without explicit reference to $\psi(\mathbf{r},t)$. We start with the definitions

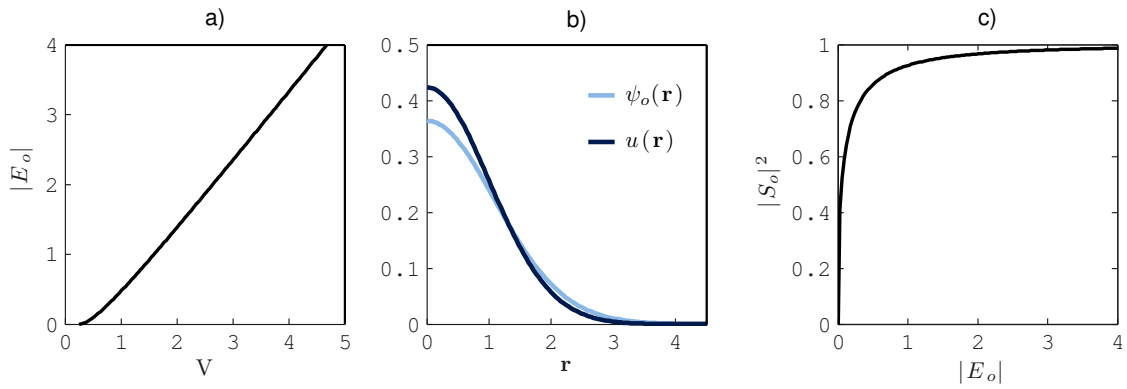

Figure 2.1: (Color online) (a) Normalized bound state energy E_0 as a function of normalized potential strength V. Sufficiently small V does not admit a bound state. Figure 1. (b) Normalized profiles for the bound state wavefunction $\psi_0(\mathbf{r})$ and the nonlocal function $u(\mathbf{r})$ for parameter values $V = 3.77$, $\sigma = 2.494a_0$ used for modeling atomic Hydrogen. Figure 1. (c) The quantity $|S_0|^2 = |\langle u(\mathbf{r})|\psi_0(\mathbf{r})\rangle|^2$ as a function of normalized bound state energy: $\psi_0(\mathbf{r})$ approaches $u(\mathbf{r})$ in the high energy limit.

of the expectation values for normalized position and momentum,

$$\langle \mathbf{r}(t) \rangle \equiv \int \mathrm{d}^3\mathbf{r}\ \psi^*(\mathbf{r},t)\,\mathbf{r}\,\psi(\mathbf{r},t), \tag{2.12}$$

and

$$\langle \mathbf{p}(t) \rangle \equiv -i\int \mathrm{d}^3\mathbf{r}\ \psi^*(\mathbf{r},t)\nabla\psi(\mathbf{r},t), \tag{2.13}$$

noting that both $\langle \mathbf{r}(t) \rangle$ and $\langle \mathbf{p}(t) \rangle$ are real. A set of ordinary differential equations relating $\langle \mathbf{r}(t) \rangle$ and $\langle \mathbf{p}(t) \rangle$ is obtained by following the steps used to derive the Ehrenfest relations. The result is similar to Eqs.(2.6) with additional terms resulting from the nonlocal binding potential:

$$\frac{\mathrm{d}\langle \mathbf{r(t)} \rangle}{\mathrm{dt}} = \langle \mathbf{p(t)} \rangle - 2V\ \mathrm{Im}\{S(t)\nabla_0 S^*(t)\}, \tag{2.14a}$$

and

$$\frac{\mathrm{d}\langle \mathbf{p(t)} \rangle}{\mathrm{dt}} = -\mathbf{E}(t) - 2V\ \mathrm{Re}\{S(t)\nabla_0 S^*(t)\}, \tag{2.14b}$$

where

$$\begin{aligned}\nabla_0 S(t) \equiv i2^{3/2}V \int_{-\infty}^{t} \mathrm{dt}'\ S(t')\ \frac{\mathbf{r}_0 + (i-t+t')\mathbf{v}_0}{[2+i(t-t')]^{5/2}} \times \\ \exp\left[i\mathscr{S}_0(t,t') + \Lambda(t,t')\right].\end{aligned} \tag{2.14c}$$

Using definitions for $\mathscr{S}_0(t,t')$ and $\Lambda(t,t')$ given in Eq.(2.6c) and Eq.(2.8) respectively. After $S(t)$ has been found via Eq.(2.8), Eqs.(2.14) can be integrated in time to compute $\mathbf{d}(t)$. Eqs.(2.14) depend only on time, having performed the integration over all space analytically. Calculating the dipole moment in this way prevents any

error introduced by considering a finite simulation domain, and is computationally more efficient than representing the wavefunction on a grid or with basis modes and computing $\mathbf{d}(t)$ directly with Eq.(2.12).

2.3.3 Bound Probability and Ionization Rate

A time-dependent measure of the bound probability is given by the projection of $\psi(\mathbf{r},t)$ onto the electron's bound state wavefunction, $\psi_0(\mathbf{r})$:

$$\rho_0(t) = |\langle\psi_0(\mathbf{r})|\psi(\mathbf{r},t)\rangle|^2. \tag{2.15}$$

The bound probability is related to the ionization rate w through the equation

$$\rho_0(t) = \rho_0(t_0)\exp\left[-\int_{t_0}^{t} \mathrm{dt}'\ w(t')\right], \tag{2.16}$$

or

$$w(t) \equiv -\frac{\mathrm{d}}{\mathrm{dt}}\ln\left[\rho_0(t)/\rho_0(t_0)\right]. \tag{2.17}$$

While this is the most natural expression for the bound probability, it is not always the easiest to calculate. For this reason, we introduce two additional definitions for the electron bound probability. A particularly convenient measure of the bound probability for the nonlocal model is defined by projecting onto $u(\mathbf{r})$ in place of $\psi_0(\mathbf{r})$ and normalizing to unity:

$$\rho_u(t) \equiv \frac{|\langle u(\mathbf{r})|\psi(\mathbf{r},t)\rangle|^2}{|\langle u(\mathbf{r})|\psi(\mathbf{r},t=0)\rangle|^2} = \frac{|S(t)|^2}{|S(0)|^2}, \tag{2.18}$$

with associated ionization rate

$$w_u(t) \equiv -\frac{\mathrm{d}}{\mathrm{dt}}\ln\left[\rho_u(t)\right] = -\frac{\mathrm{d}}{\mathrm{dt}}\ln\left[\frac{|S(t)|^2}{|S(0)|^2}\right]. \tag{2.19}$$

The values of $\rho_0(t)$ and $\rho_u(t)$ (and hence $w(t)$, $w_u(t)$) are exactly equal when the electron is entirely bound, i.e., before the laser field is introduced. As the atom undergoes ionization, some fraction of the bound electron wavefunction will transition to the continuum of free states, during which the projection of $\psi(\mathbf{r},t)$ onto $u(\mathbf{r})$ and $\psi_0(\mathbf{r})$ won't in general give the same result. After the pulse has passed, free components of the wavefunction continue to spread out in space, leaving only the remaining bound wavefunction to project significantly onto $u(\mathbf{r})$; free state contributions to $\rho_u(t)$ are accordingly reduced, and $\rho_u(t) \to \rho_0(t)$ in the long time limit.

The extent that $\rho_u(t) \approx \rho_0(t)$ for intermediate times (i.e., during the simulation) depends on the similarity of the spatial profiles of $u(\mathbf{r})$ and $\psi_0(\mathbf{r})$. For parameters used to model atomic Hydrogen, the spatial profiles of $u(\mathbf{r})$ and $\psi_0(\mathbf{r})$ are compared in Fig.2.1(b). The similarity in profiles suggests that $\rho_u(t)$ should be a good approximation of $\rho_0(t)$ - this is later confirmed with simulation results in section 2.4.1. Moreover, the accuracy of $\rho_u(t)$ improves for larger values of the bound state energy; if E_0 is increased (achieved by increasing V), the bound wavefunction $\psi_0(\mathbf{r})$ more closely conforms to $u(\mathbf{r})$, and $|S_0|^2 = |\langle u(\mathbf{r})|\psi_0(\mathbf{r})\rangle|^2$ approaches unity, as seen in Fig.2.1(c). In the limit $E_0 \to \infty$, $\rho_u(t) = \rho_0(t)$ exactly. For the profile shown in Fig.2.1(b), $|\langle u(\mathbf{r})|\psi_0(\mathbf{r})\rangle|^2 \approx .98$.

The last measure of bound probability considered here does not directly relate the nonlocal model but is included here for organizational purposes and used exclusively in the *ab initio* simulation. Here, an approximate measure of the bound probability is given by the cumulative probability density of the electron wavefunc-

tion integrated out to radius $|\mathbf{r}| = \mathrm{r_c}$ and normalized to unity at $t = 0$:

$$\rho_c(t) \equiv \frac{\int\limits_{|\mathbf{r}|<\mathrm{r_c}} \mathrm{d}^3\mathbf{r}\ |\psi(\mathbf{r},t)|^2}{\int\limits_{|\mathbf{r}|<\mathrm{r_c}} \mathrm{d}^3\mathbf{r}\ |\psi(\mathbf{r},0)|^2}. \tag{2.20}$$

This definition is convenient if the value of $\psi(\mathbf{r},t)$ is known, but requires a value of $\mathrm{r_c}$ to be chosen. Ideally, the value $\mathrm{r_c}$ is large enough to include the bound electron wavefunction and small enough to exclude free wavefunction components as they propagate outward; as these cannot be simultaneously satisfied (bound wavefunctions are generally infinite in spatial extent, and low momenta free states propagate slowly), there is some flexibility in the choice of $\mathrm{r_c}$ and hence the value of $\rho_c(t)$. As with the quantity $\rho_u(t)$, normalizing to the initial integrated probability ensures that $\rho_c(t)$ will match $\rho_0(t)$ at $t = 0$ and in the long time limit.

Each of these definitions is included in this work for separate reasons: While $\rho_0(t)$ is the most desirable measure of bound probability, it requires spatial integration of the wavefunction and is generally time consuming. By contrast, $\rho_u(t)$ is an approximate measure of bound probability, but efficiently obtained for the nonlocal model. Finally, the available data for the *ab initio* simulation is $\rho_c(t)$, and is used to calibrate the nonlocal model for suitable choice of $\mathrm{r_c}$.

2.4 Comparison with hydrogen

Having presented some of the basic properties of the nonlocal model, we now attempt to simulate the strong field atomic response of Hydrogen. In particular, we would like to replicate the dipole response and ionization properties of atomic Hydrogen for typical laboratory ultrashort laser pulse parameters.

We proceed by comparing simulations of the nonlocal model against two established models; an *ab initio* TDSE simulation, and a modified version of the well known Keldysh ionization model [29]. Comparison with each of these provides a different type of validation. The *ab initio* simulation [4] numerically simulates the electron wavefunction time evolution via Eq.(2.1), and provides the highest fidelity treatment of the system we consider in this thesis. While such a comparison is invaluable, the computational demands of full TDSE simulations allow a limited number of runs for comparison. To investigate the accuracy of the nonlocal model over a range of different parameters, we turn to the Popruzhenko, Mur, Popov, and Bauer (PMPB) [2] ionization rate model. In contrast to the TDSE simulation, the PMPB model does not simulate the time dynamics of the electron wavefunction. Rather, it only predicts the atomic ionization rate for a monochromatic electric field. While the PMPB model offers significantly less information than a full TDSE simulation, it can be used to validate the nonlocal model over a large range of laser frequencies and intensities in relatively short computation time.

To compare the nonlocal model with those mentioned above, values must be determined for V and σ. The value for V was determined by Eq.(2.10) such that $E_0 = -13.6$ eV; in as far as we wish to simulate Hydrogen, this is the most logical choice. This value was modified slightly for comparison with the *ab initio* simulation, so as to match the numerical ground state eigenenergy. The value of σ was determined by matching the total drop in bound probability of the nonlocal model with that of the *ab initio* simulation (Fig.2.3), and used for all comparisons in this thesis.

2.4.1 *ab initio* TDSE simulation comparison

A brief summary of the the *ab intio* TDSE simulation is as follows: the Coulomb potential in Eq.(2.1) is replaced with a soft-core potential, $|\mathbf{r}|^{-1} \to (|\mathbf{r}|^2 + \delta\mathbf{r}^2)^{-1/2}$, where $\delta\mathbf{r} = .05$ a.u. is a small constant to accommodate the divergent Coulomb potential on a finite spatial grid. The Schrödinger equation is put into conservative form and $\psi(\mathbf{r}, t)$ is propagated via the finite volume method. The spatial domain consists of $4096 \times 32,768$ ($\mathrm{r}_\perp \times \mathrm{z}$) cells of size 0.04×0.04 a.u., and the time domain consists of $40,000 \times 0.04$ a.u. time steps (approximately 40 fs). Use of the soft-core potential and finite spatial resolution results in a similar eigenspectrum as Hydrogen for the first several bound states. The numerical ground state energy is equal to $E_0 = -13.385$ eV.

In the simulation, a single Hydrogen atom initially in the ground state is subjected to a 14.1 fs (fwhm) linearly polarized laser pulse of 800 nm light with a maximum intensity $\mathrm{I_{max}} = 2.12 \times 10^{14}$ W/cm^2. The exact form of the field is $E(t) \equiv -\partial A_L/\partial t$ with $A_L(t) = A_0 \sin^2(\pi t/\tau)\cos(\omega_L t)$, where $A_0 = 1.37$, $\omega_L = .057$, and $\tau = 800$ in atomic units.

For the *ab initio* simulation, $\rho_c(t)$ was calculated for $\mathrm{r_c} = 3, 10$, and 100 a.u., corresponding to initial integrated probabilities (numerator of Eq.(2.20)) of .934, .9999994, and ~ 1, respectively. The results are plotted in Fig.2.2 (with $\mathbf{E}(t)$ for reference), with some notable differences: The $\mathrm{r_c} = 100a_0$ curve is still decreasing at 40 fs, indicating that free components of the wavefunction are still propagating out of the integration region, and therefore not a good measure of bound probability.

To a lesser extent, this same effect smoothes out the features in the $r_c = 10a_0$; the $3a_0$ curve is therefore the most appropriate of the three to use for comparison with the nonlocal model. The oscillatory features seen in the $3a_0$ curve are a result of the electric field distorting the (total) potential. As the applied field translates the minimum of the potential well, the "bound" portion of the wavefunction shifts against the fixed integration region, resulting in the observed minima. While this detail is largely absent in the $r_c = 10a_0$ curve, both curves give approximately the same bound probability by the end of the simulation, indicating that approximately 47% of the wavefunction has transitioned to free states and dispersed beyond $r_c = 10a_0$.

This data provides one means of calibrating the nonlocal model. On performing the analogous nonlocal simulation, the free parameter σ is adjusted such that the value of $\rho_u(t_f)$ matches that of $\rho_c(t_f)$ for the *ab initio* run. The value $\sigma = 2.494a_0$ was determined as a best fit for the $r_c = 3a_0$ *ab initio* run, shown in Fig.2.3. Agreement of these curves demonstrates that the nonlocal model can produce an ionization rate similar to that obtained by the *ab initio* simulation as defined by Eq.(2.17) for laser these parameters. Later comparison with PMPB ionization theory demonstrates more generally that a single value of σ can be used to reproduce predicted ionization rates over a range of laser pulse intensities and frequencies.

Although this agreement suggests that $\rho_u(t)$ can be used as a measure of bound probability, it is worth examining how accurately $\rho_u(t)$ represents $\rho_0(t)$ as defined in Eq.(2.15) for the nonlocal model. Figure 2.4 compares $\rho_u(t)$ and $\rho_0(t)$ for several runs

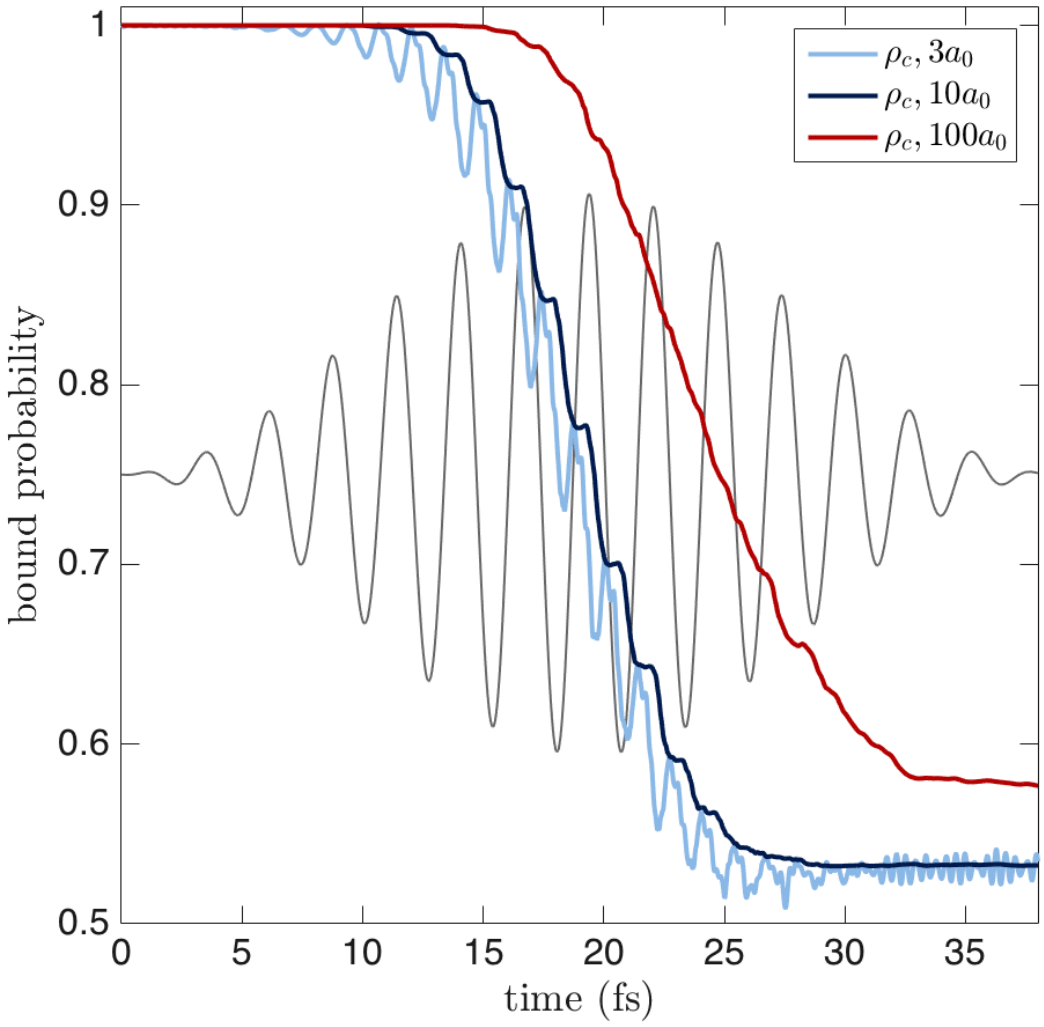

Figure 2.2: (Color online) Measures of the bound probability given by Eq.(2.20) for three different radii in the *ab initio* simulation.

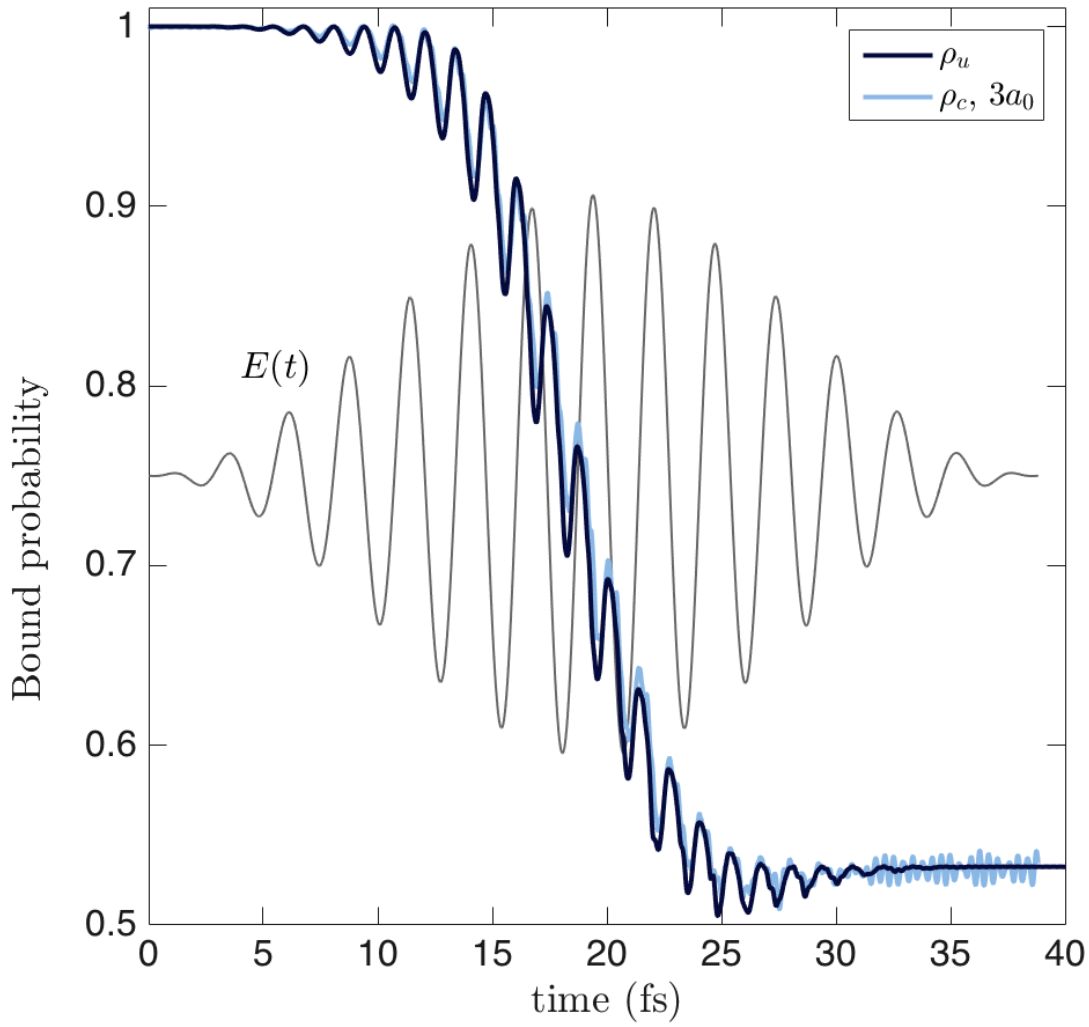

Figure 2.3: (Color online) A comparison of the $r_c = 3a_0$ integrated probability (*ab initio* simulation) with the approximate bound probability $\rho_u(t)$ (nonlocal model).

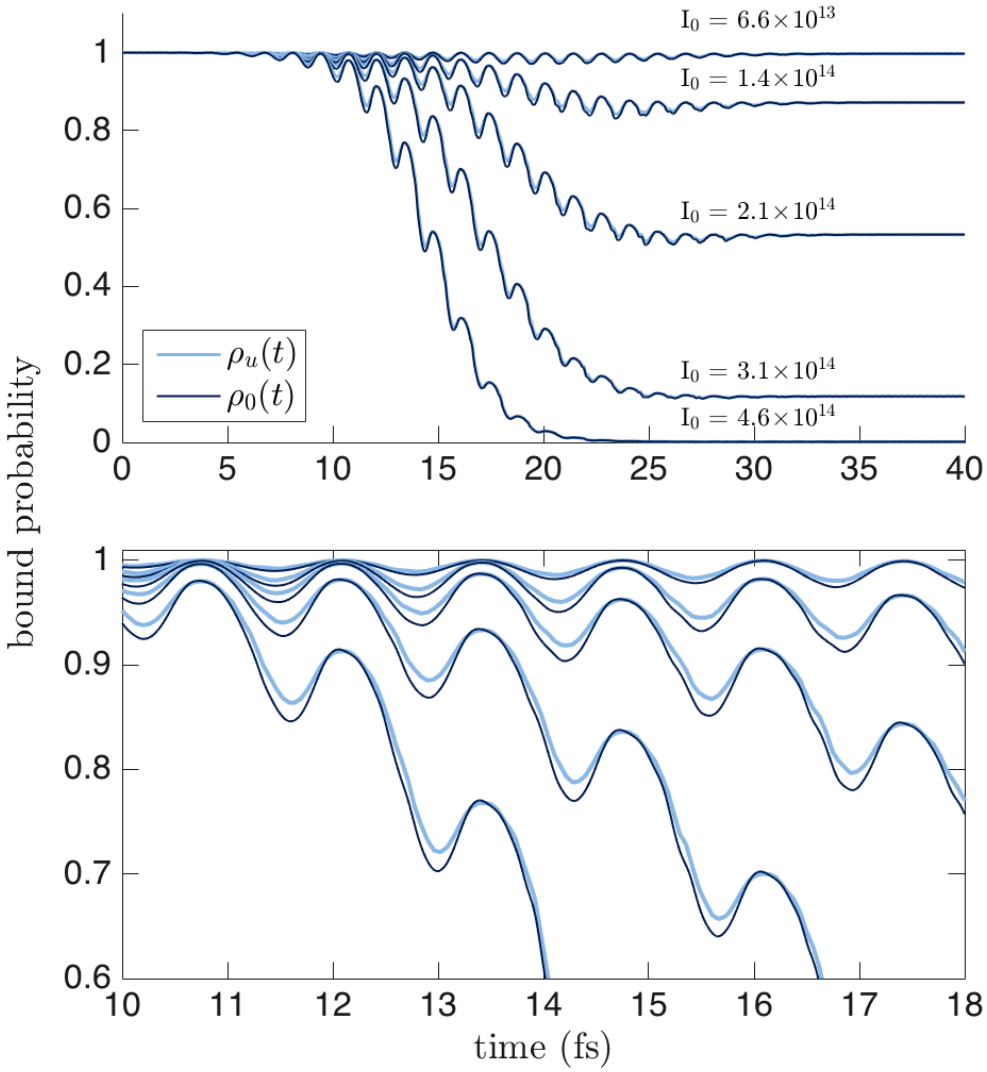

Figure 2.4: (Color online) Top: a direct comparison of $\rho_u(t)$ (dark blue) with $\rho_0(t)$ (light blue) for the nonlocal model for five different laser intensities of a 14.1 fs 800 nm light laser pulse. The quantity $\rho_0(t)$ is produced by calculating $\psi_0(\mathbf{r})$ and $\psi(\mathbf{r},t)$ via Eq.(2.11) and Eq.(2.7), respectively. These are then numerically integrated on a spatial grid $\mathrm{r}_\perp \times \mathrm{z}$ $(30a_0 \times 30a_0)$ and normalized to the numerical value of $|\langle\psi_0(\mathbf{r})|\psi_0(\mathbf{r},t=0)|^2 = .95$. Bottom: an inset of the data is shown for greater detail. On the completion of each laser cycle (relative maxima), the plots agree to within .06%, the order of error in the normalization of $|\langle\psi_0(\mathbf{r})|\psi(\mathbf{r},t)\rangle|^2$.

of various laser intensity. Values for $\psi_0(\mathbf{r})$ and $\psi(\mathbf{r},t)$ were calculated via Eqs.(2.7) and (2.11) on a spatial grid in $\mathrm{r}_\perp \times \mathrm{z}$ ($30a_0 \times 30a_0$), and numerically integrated to obtain $\rho_0(t)$. For the data provided, the accuracy of $\rho_0(t)$ is limited by integrating on a spatial grid and truncation of the integral in Eq.(2.7). This plot demonstrates the efficiency of the nonlocal model: a $\sim 1000\times$ increase in computation time required to compute $\rho_0(t)$ gives essentially the same result as given by $\rho_u(t)$.

Nevertheless, rendering $\psi(\mathbf{r},t)$ can be an aid to understanding the time dynamics of the system. Figure 2.5 shows a time series of the nonlocal electron wavefunction responding to $\mathbf{E}(t)$ (Fig.2.3). Here, the probability density $|\psi(\mathbf{r},t)|^2$ is calculated in the $\mathrm{r}_\perp \times \mathrm{z}$ ($167a_0 \times 167a_0$) plane and plotted on a natural log scale. The first pane (0 fs) shows the bound state probability density profile, the following six frames show the evolution over approximately one laser cycle from 10.5 to 13.8 fs, and the last frame shows the wavefunction shortly after the pulse has passed. The free components still in view at 41.7 fs do not contribute significantly to the bound probability (see Fig.2.3) and continue to disperse from the region as time progresses. For these simulation parameters, the ionized wavefunction continues to interact with the binding potential over the course of the laser period, and interference patterns in the free wavefunction are observed. Such effects are accounted for in the nonlocal quantities $\rho_u(t)$ and $\langle\mathbf{r}(t)\rangle$, and are not included in ionization rate models. For this simulation, $\rho_u(t)$ and $\langle\mathbf{r}(t)\rangle$ can be calculated in less than a minute on a typical laptop computer.

The last quantity compared with the *ab initio* simulation is the dipole moment, $\mathbf{d}(t)$ $(-\langle\mathbf{r}(t)\rangle)$, shown in Fig.2.6. Again, agreement is observed. One feature of

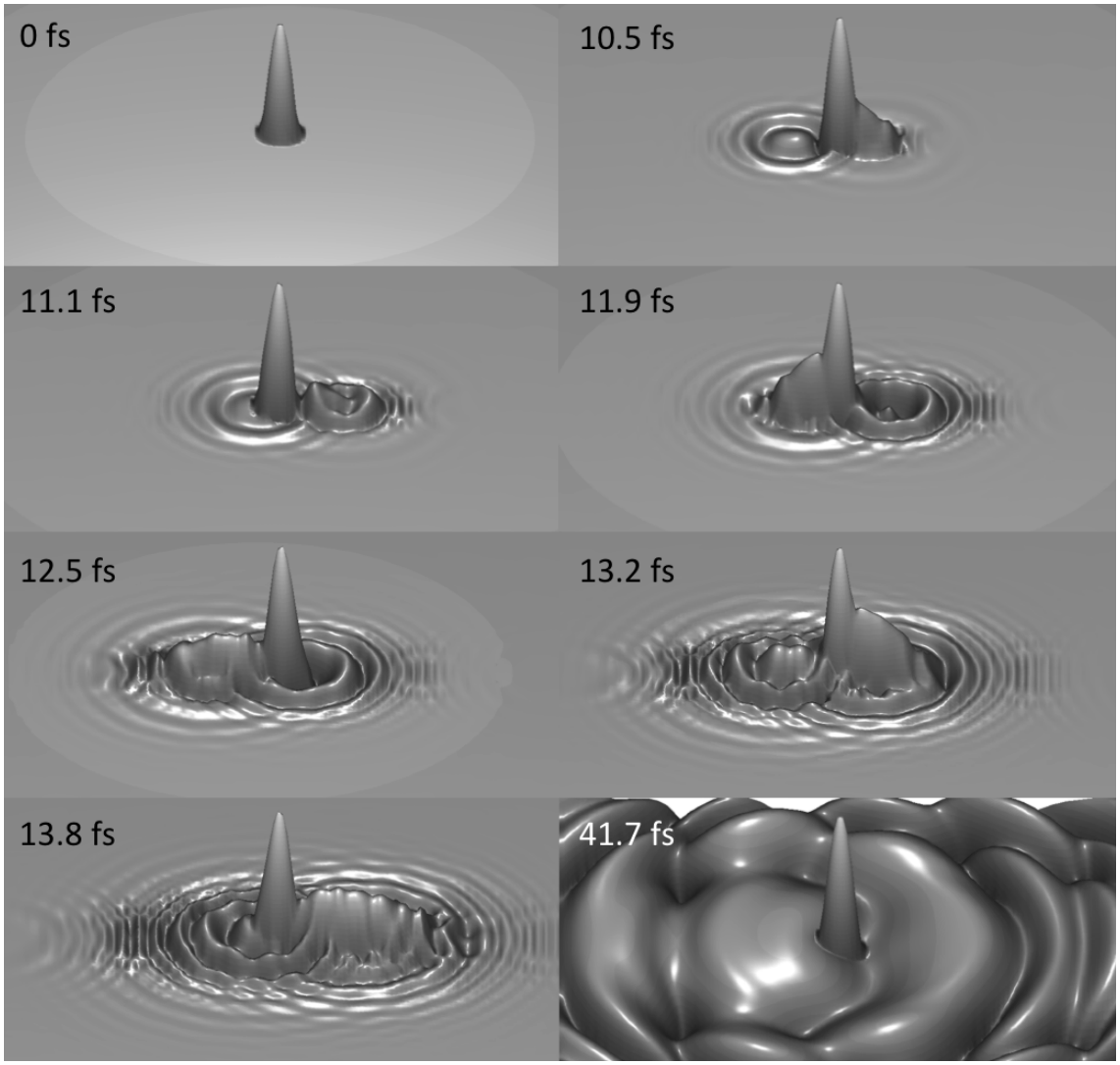

Figure 2.5: The nonlocal wavefunction density in the $r_\perp \times z$ plane ($167a_0 \times 167a_0$), plotted on a natural log scale. The frames depict the bound state profile (0 fs), approximately one laser cycle of evolution (10.5 - 13.8 fs), and a frame shortly after the laser pulse has passed (41.7 fs). Throughout, rescattering is observed as free components of the electron make subsequent passes across the binding potential.

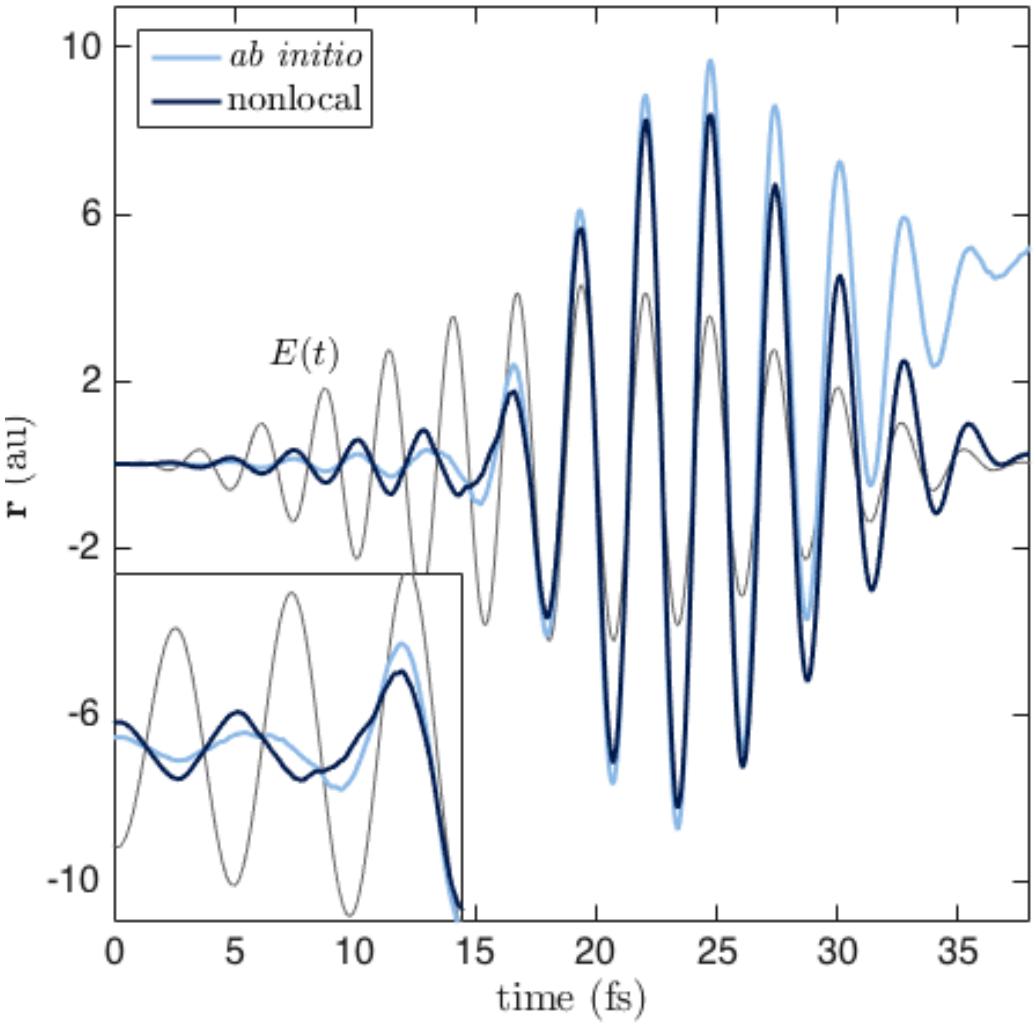

Figure 2.6: (Color online) The predicted *ab initio* hydrogen and nonlocal dipole moments are compared. The inset (10 - 18 fs) shows the point at which the dipole transitions from a "bound" to "free" response. The dipole shown in the first half of the inset corresponds to the wavefunction depicted in Fig.2.5.

interest occurs at approximately 13 fs, shown in the inset, at which point $\mathbf{r}(t)$ changes relative phase with the applied field, $\mathbf{E}(t)$. Prior to 13 fs, both plots of $\langle \mathbf{r}(t) \rangle$ are seen to be out of phase with the electric field, and afterwards largely in phase. This can be understood in the following way: the "bound" electron response is largely out of phase with the field and initially dominates. As $\mathbf{E}(t)$ increases in strength, some of the electron wavefunction is excited to continuum states, leaving the vicinity of the ion and contributing as a "free" response to the dipole moment. Because the spatial excursions of the free wavefunction are large compared to the wavefunction in the ground state, a comparatively small fraction of unbound wavefunction will dominate the atomic dipole, causing the net dipole moment to change sign with respect to the field.

2.4.2 PMPB ionization theory comparison

In this section we compare the ionization rate predicted by the PMPB model with that of the nonlocal model as given by Eq.(2.19). The PMPB ionization model predicts the probability of ionization of a Coulomb bound electron in the presence of a low field amplitude ($\max|\mathbf{E}(t)| < |E_0|/a_0$) sinusoidally varying electric field. The rate shares the same exponential dependence on the electric field amplitude as the rate predicted by Keldysh, but includes an improved field-dependent Coulomb correction. Direct comparison with the PMPB model is complicated by the fact that it only predicts a cycle averaged rate for monochromatic fields. Since nonlocal simulations are performed in the time domain and require that $E(t) = 0$ on the

semi-infinite range of $t < t_0$, any electric field is necessarily enveloped and therefore contains a range of intensities and frequency components.

For this reason, it is easier to perform laser pulse simulations in the time domain and compare the net ionization predicted by the nonlocal and PMPB models. We define an effective ionization rate in terms of the total drop in bound probability and full-width half-maximum pulse time as:

$$w_{\text{eff}} \equiv -\frac{1}{T_{\text{fwhm}}} \ln\left[\rho(t_f)/\rho(t_0)\right]. \tag{2.21}$$

To compute w_{eff} for the PMPB model, the PMPB rate is first converted to a bound probability via Eq.(2.15) based on the field envelope, which is then evaluated after the pulse has passed to generate w_{eff}. The analogous quantity for the nonlocal model is given by calculating $\rho_u(t)$ (Eq.(2.18)), and again evaluating after the pulse has passed. For all the nonlocal data compared with the PMPB rate model, a best fit value is used $\sigma = 2.45a_0$ (2% different than the value used to match the *ab initio* simulation), and V was chosen via Eq.(2.10) such that $|E_0| = 13.6$ eV for both the PMPB and nonlocal models.

2.4.2.1 Frequency dependence

Comparison of the frequency dependence is a crucial test for the nonlocal model. The PMPB model predicts a strong dependence of ionization rate on the laser frequency, with local maxima in the rate w occurring for each N-photon resonance, when $N\hbar\omega_{laser} \approx |E_0|$. This expression is only approximate because the laser field distorts the effective binding potential energy (i.e., there are AC stark shifts

[34]). To compare the frequency dependence of the PMPB and nonlocal ionization rates, simulations were performed in which a Hydrogen atom is subject to a single frequency laser pulse, and w_{eff} computed for both models. The electric field envelope and its derivative are piecewise continuous and defined to have a 15 fs $\sin^2(t)$ ramp to a constant amplitude of 1×10^{13} W/cm^2 for 55 fs before symmetrically ramping back down to zero; this profile was chosen to minimize dependence of the ionization rate on intensity and isolate frequency dependence in w_{eff}. Figure 2.7 shows the results for several simulations of varied carrier frequency. The nonlocal model is seen to reproduce each N-photon resonance predicted by the PMPB model; the highest peak occurs at the single photon ionization rate, where $\hbar\omega_{\text{laser}} \approx 1.2|E_0|$. Above this frequency, the ionization rate drops off as the electron cannot respond quickly enough to the laser field oscillations. On increasing the intensity of the laser to 1.9×10^{13} W/cm^2, the procedure was repeated for typical laboratory laser frequencies, shown in the bottom pane of Fig. 2.7.

2.4.2.2 Intensity Dependence

The intensity dependences of the nonlocal and PMPB models were also compared. Here, a Hydrogen atom is subject to an 14.6 fs, 800 nm laser pulse with a $\sin^2(t)$ envelope, and w_{eff} calculated for both models. This procedure was repeated while varying peak laser intensity and plotted in Fig. 2.8. The lower limit of ionization rate detection is limited by the accuracy of measuring changes in $\rho_u(t)$, while agreement at high intensity is limited by the effect of depletion: at 1x10^{15} W/cm^2,

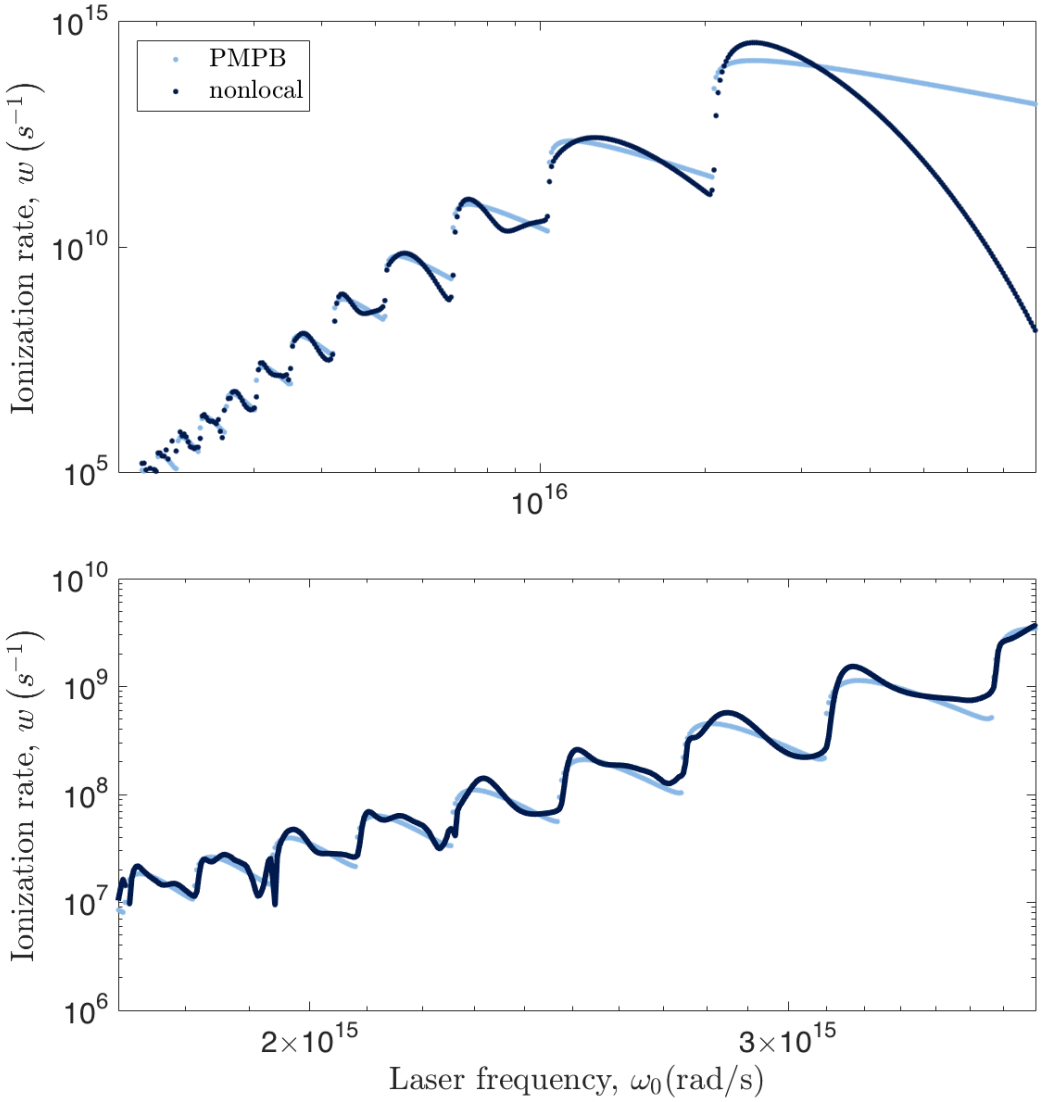

Figure 2.7: (Color online) Top: the PMPB and nonlocal effective ionization rates (w_{eff}) show agreement when compared over a range of frequencies. Bottom: the same result for optical frequencies, with the laser intensity increased to $\mathrm{I}_0 = 1.9 \times 10^{13}$ W/cm^2.

the electron is (almost) completely ionized before the end of the pulse. Residual wavefunction in the vicinity of $u(\mathbf{r})$, either from rescattering events or of numerical origin, eventually suppresses the nonlocal effective rate when compared with the PMPB effective rate.

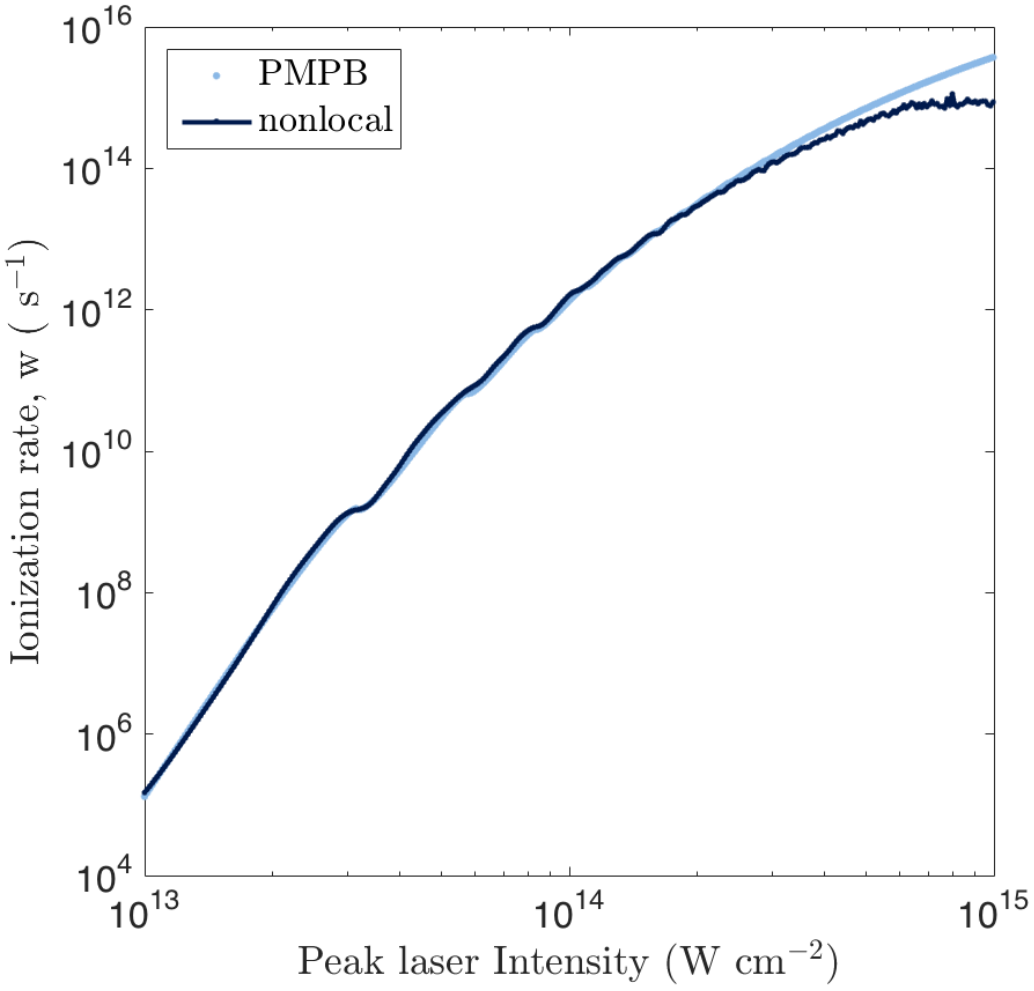

Figure 2.8: (Color online) Intensity dependence of the nonlocal and PMPB effective ionization rate for a 14.6 fs pulse of 800 nm light.

2.5 Chapter 2 summary

This chapter examines a model Schrödinger equation with a nonlocal gaussian potential for modeling high field-atom interactions. It is shown that this model can successfully reproduce some features of the Schrödinger equation with a Coulomb potential, and allows for efficient computation. Specifically, it is shown that, when compared with a finite-difference time-domain *ab initio* simulation of atomic hydrogen subject to a strong 800nm wavelength electric field, the nonlocal model can accurately reproduce the atomic bound probability (and hence ionization rate). The quantity $|S(t)|^2$ is a useful proxy for calculating the bound probability or ionization rate and yields nearly identical results to the ground state projection ($|\langle\phi_0(\mathbf{x})|\phi(\mathbf{x},t)\rangle|^2$). Comparison with the analytic PMPB ionization rate model demonstrates strong agreement of the intensity and frequency dependence of the applied laser field spanning a wide range of parameters from the multiphoton to tunnel ionization regime. It was noted, however, that nonlocal potentials do not generally exhibit gauge independence, a feature shared by all local potential formulations. This is examined in some detail in the next chapter.

Chapter 3: Gauge dependence

Chapter 2 demonstrated that the length gauge formulation of the nonlocal potential gives good agreement with established models for the photoionization rate as a function of laser intensity and laser frequency. It was noted that, while many fundamental properties are retained for nonlocal potentials in the Schrödinger equation - including local flux conservation, norm conservation and self-adjointness - nonlocal potentials do not generally satisfy the gauge independence that local potentials exhibit; thus, the numerical results will depend on which gauge is chosen to represent the Schrödinger equation. Gauge dependence has been considered by many authors [35], as this can be problematic for local potentials when approximations are invoked. In this chapter, we examine the linear polarizability and photoionization rates predicted by the nonlocal gaussian model in the length and velocity gauges. This work is summarized in the peer-reviewed publication [36].

3.1 Gauge invariance of local potentials

We briefly examine the gauge invariance of local potential formulations of the time-dependent Schrödinger equation. Specifically, we consider the TDSE for the wavefunction of a single electron in the presence of an atomic potential $V(\mathbf{x})$ and

a classical electromagnetic field $\mathbf{F}(t)$ in the dipole approximation with no back-reaction. The time-dependent electric field is represented in the Schrödinger equation via the electromagnetic potential terms, defined through the relation $\mathbf{F}(t) = -\partial_t \mathbf{A}(t) - \nabla\Phi(\mathbf{x}, t)$, noting that, for simplicity we require $\mathbf{A}(t)$ depend only on time and that $\Phi(\mathbf{x}, t)$ be linear in $\mathbf{x}$. The magnetic field is ignored. In this chapter we use a signed convention for atomic units (a.u.), where $\hbar = m_e = 1$, $q_e = -1$. The general form of the Schrödinger equation is then:

$$i\partial_t \psi(\mathbf{x}, t) = \left[\frac{1}{2}\left(-i\nabla + \mathbf{A}(t)\right)^2 - \Phi(\mathbf{x}, t) - V(\mathbf{x})\right]\psi(\mathbf{x}, t). \tag{3.1}$$

The choice of $\mathbf{A}$ and Φ is not unique; one may define a new set of potentials $\mathbf{A}', \mathbf{\Phi}'$ with the addition of a gauge term

$$\mathbf{A}'(t) \equiv \mathbf{A}(t) + \nabla\chi(\mathbf{x}, t) \tag{3.2}$$

$$\Phi'(\mathbf{x}, t) = \Phi(\mathbf{x}, t) - \partial_t \chi(\mathbf{x}, t) \tag{3.3}$$

that produce the same field $\mathbf{F}(t)$, noting that the gauge term takes the form $\chi(\mathbf{x}, t) = \mathbf{x} \cdot \Delta\mathbf{A}(t)$ for this system.

On defining a new wavefunction that is modified by a local phase factor,

$$\psi'(\mathbf{x}, t) = \exp\left[-i\chi(\mathbf{x}, t)\right]\psi(\mathbf{x}, t), \tag{3.4}$$

we express the original Schrödinger equation in terms of the primed variables, and operate on the gauge term, i.e. $i\partial_t\psi = \exp(i\chi)(i\partial_t - \partial_t\chi)\psi'$, and $(-i\nabla + \mathbf{A}(t))\exp(i\chi)\psi' = \exp(i\chi)(-i\nabla + \mathbf{A}(t) + \nabla\chi)\psi'$, leading to a Schrödinger equation of equivalent form in the transformed variables

$$i\partial_t \psi'(\mathbf{x}, t) = \left[\frac{1}{2}\left(-i\nabla + \mathbf{A}'(t)\right)^2 - \Phi'(\mathbf{x}, t) - V(\mathbf{x})\right]\psi'(\mathbf{x}, t). \tag{3.5}$$

Both the original and gauge-transformed Schrödinger equations reproduce the same set of observables and are therefore said to be gauge invariant.

3.2 Gauge dependence of nonlocal potentials

If we allow the potential to take the form of an operator acting on the the wavefunction $V(\mathbf{x})\psi(\mathbf{x},t) \to \hat{V}\psi(\mathbf{x},t)$, we may define a nonlocal potential [31] as:

$$\hat{V}\psi(\mathbf{x},t) \equiv V_0 u(\mathbf{x}) S(t) \tag{3.6}$$

$$S(t) \equiv \int d^3\mathbf{x}' u^*(\mathbf{x}')\psi(\mathbf{x}',t) \tag{3.7}$$

$$u(\mathbf{x}) = \sigma^{-3} \exp\big(-\mathbf{x}^2/(2\sigma^2)\big) \tag{3.8}$$

where we have chosen to use a gaussian shape function for $u(\mathbf{x})$. Specifically, the nonlocal potential term is comprised of the function $u(\mathbf{x})$ scaled by the projection of the wavefunction onto $u^*(\mathbf{x})$. Projecting onto the complex conjugate ensures the non-local potential remains self-adjoint. Loosely speaking, the positive real valued constant V_0 controls the "strength" of the potential ($V_0 > 0$ is attractive) and σ, with dimension of length, controls the width of the potential. On performing the same gauge transformation as done in the previous section (and dividing through by an overall phase factor $\exp(i\chi)$) the nonlocal potential term appears in the gauge-transformed Schrödinger equation as:

$$\hat{V}\psi(\mathbf{x},t) \to \exp(-i\chi)u(\mathbf{x}) \int d^3\mathbf{x}' u^*(\mathbf{x}') \exp(i\chi)\psi'(\mathbf{x}',t) \tag{3.9}$$

and it can be seen that the potential term is modified by the phase factor χ.

A form of gauge invariance can be introduced if we treat $u(\mathbf{x})$ as a field that

undergoes the same transformation as $\psi(\mathbf{x},t)$, namely $u'(\mathbf{x},t) \equiv \exp(-i\chi)u(\mathbf{x})$; the transformed Schrödinger equation is of the same form as the original and will yield the same observables. This implies that $u(\mathbf{x})$ depends on the gauge, and $u'(\mathbf{x},t)$ (the gauge transformed shape function of the atomic potential) now depends on the introduced field.

Alternative nonlocal potential formulations may be derived directly from local potentials, e.g. the Coulomb potential; this approach has been examined in previous works [37–39]. If the nonlocal representation is exact, the system will be gauge independent.

However, if the nonlocal potential has no local equivalent (like the model gaussian potential investigated in this work) the question naturally arises: is there a natural gauge for introducing a nonlocal potential? We examine two obvious choices, setting either $\mathbf{A} = 0$ or $\Phi = 0$ in Eq.(3.1), defining the electric field through a single potential term.

The analysis in the remainder of this chapter will use the k-space (momentum) representation for convenience via the Fourier transform definitions,

$$\phi(\mathbf{k}) = \frac{1}{(2\pi)^{3/2}} \int d^3\mathbf{x}' \; e^{-i\mathbf{k}\cdot\mathbf{x}'} \psi(\mathbf{x}') \tag{3.10a}$$

$$\psi(\mathbf{x}) = \frac{1}{(2\pi)^{3/2}} \int d^3\mathbf{k}' \; e^{i\mathbf{k}'\cdot\mathbf{x}} \phi(\mathbf{k}') \tag{3.10b}$$

so that the (canonical) momentum is given by $-i\nabla \rightarrow \mathbf{k}$. We examine the Schrödinger equation in the so-called length gauge, where $\mathbf{A}(t) = 0$ in Eq.(3.1), and the velocity gauge, where $\Phi(\mathbf{x},t) = 0$. The momentum-space equations in these

two cases are:

$$\left[i\partial_t - \frac{1}{2}\mathbf{k}^2 + i\partial_t \mathbf{A}(t)\cdot\nabla_{\mathbf{k}}\right]\phi_L(\mathbf{k},t) = -\hat{V}\phi_L(\mathbf{k},t), \tag{3.11a}$$

and

$$\left[i\partial_t - \frac{1}{2}\left(\mathbf{k}+\mathbf{A}(t)\right)^2\right]\phi_V(\mathbf{k},t) = -\hat{V}\phi_V(\mathbf{k},t), \tag{3.11b}$$

where the subscripts designate length and velocity gauge wavefunctions respectively. The nonlocal potential operator is identical in both equations, specifically

$$\hat{V}\phi(\mathbf{k},t) \equiv V_0 u(\mathbf{k}) \int d^3\mathbf{k}' u^*(\mathbf{k}')\phi(\mathbf{k}',t), \tag{3.12}$$

$$u(\mathbf{k}) \equiv \exp(-\sigma^2\mathbf{k}^2/2). \tag{3.13}$$

We note that the electric potential is written in terms of a single variable $\mathbf{A}(t)$ in both equations, where the electric field is defined as $\mathbf{E}(t) = -\partial_t\mathbf{A}(t)$.

Although we have represented the electric field using a common potential, Eqs.(3.11a), (3.11b) are not equivalent. We substitute the explicit expressions for the nonlocal potential in Eqs.(3.11a) and (3.11b), introduce integrating factors, and obtain:

$$\phi_L(\mathbf{k},t) = iV_0 \int_{-\infty}^{t} dt' \exp\left[-\frac{i}{2}\int_{t'}^{t} dt''\left(\mathbf{k}-\mathbf{A}(t)+\mathbf{A}(t'')\right)^2\right]\ldots$$

$$u(\mathbf{k}-\mathbf{A}(t)+\mathbf{A}(t'))S_L(t') \tag{3.14a}$$

$$\phi_V(\mathbf{k},t) = iV_0 \int_{-\infty}^{t} dt' \exp\left[-\frac{i}{2}\int_{t'}^{t} dt''\left(\mathbf{k}+\mathbf{A}(t'')\right)^2\right]\ldots$$

$$u(\mathbf{k})S_V(t') \tag{3.14b}$$

where

$$S_{V,L}(t) = \int d^3\mathbf{k} u^*(\mathbf{k})\phi_{V,L}(\mathbf{k}), \tag{3.15}$$

which follows from Eq.(3.7).

3.3 Field free system properties

If $\mathbf{A}(t) = 0$, the length and velocity gauge systems are equivalent. The time independent system is found to have a single bound state which can be represented explicitly in momentum space:

$$\phi_0(\mathbf{k}) = \frac{2V_0 S_0 u(\mathbf{k})}{|\mathbf{k}|^2 + k_0^2} \tag{3.16}$$

$$S_0 \equiv \int d^3\mathbf{k}' u^*(\mathbf{k}')\phi_0(\mathbf{k}') \tag{3.17}$$

where $k_0 \equiv \sqrt{2E_0}$ is real and positive defined for a state with total energy $-|E_0|$. Multiplying both sides of Eq.(3.16) by $u^*(\mathbf{k})$, integrating over all momenta, and dividing both sides by S_0, we obtain the consistency relation

$$1 = 2V_0 \int d^3\mathbf{k}' \frac{|u(\mathbf{k}')|^2}{|\mathbf{k}'|^2 + k_0^2}. \tag{3.18}$$

Equation (3.18) relates E_0, σ, and V_0, which can be integrated to give

$$1 = \frac{4\pi^{3/2} V_0}{\sigma}\left[1 - \sqrt{\pi}\sigma k_0 \exp\left(\sigma^2 k_0^2\right) \mathrm{erfc}\left(\sigma k_0\right)\right]. \tag{3.19}$$

Here, erfc is the complimentary error function. The integral in Eq.(3.18) is a monotonically decreasing function of k_0^2, implying that only a single bound state is supported by the nonlocal potential (in contrast to a gaussian local potential [40]); for a

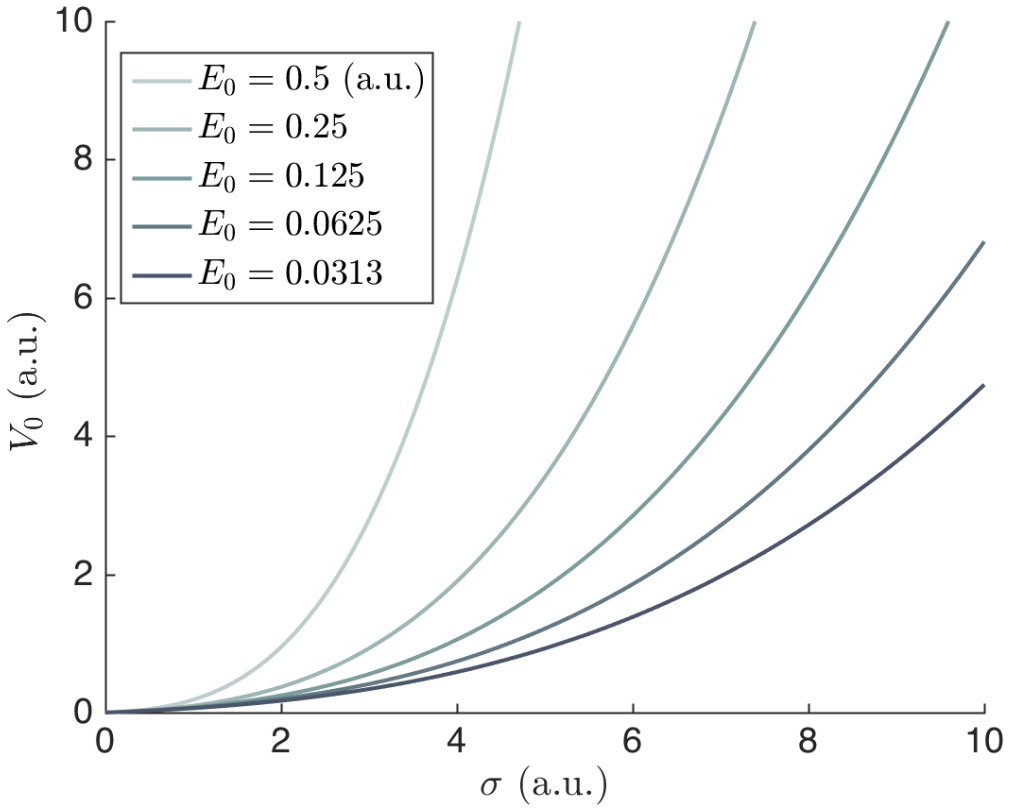

Figure 3.1: (Color online) Curves relating V_0 and σ for constant values of E_0 that satisfy Eq.(3.19). Shown here for the first five hydrogen states, the gaussian nonlocal potential supports a (single) bound state of arbitrary energy.

chosen value of V_0 and σ, only a single value of $E_0 = k_0^2/2$ will satisfy the consistency relation Eq. (3.18).

Figure 3.1 shows the values of V_0 vs σ for the energies corresponding to the first five states of the hydrogen eigen-spectrum, $E_n = .5/n^2$. Once the bound state energy is specified, σ is used as a fitting parameter that determines V_0 via Eq.(3.19). Figure 3.2 shows a comparison of the nonlocal wavefunction, $\psi_0(\mathbf{x})$, for various values of σ ($E_0 = .5$); the hydrogen 1s orbital is provided for comparison.

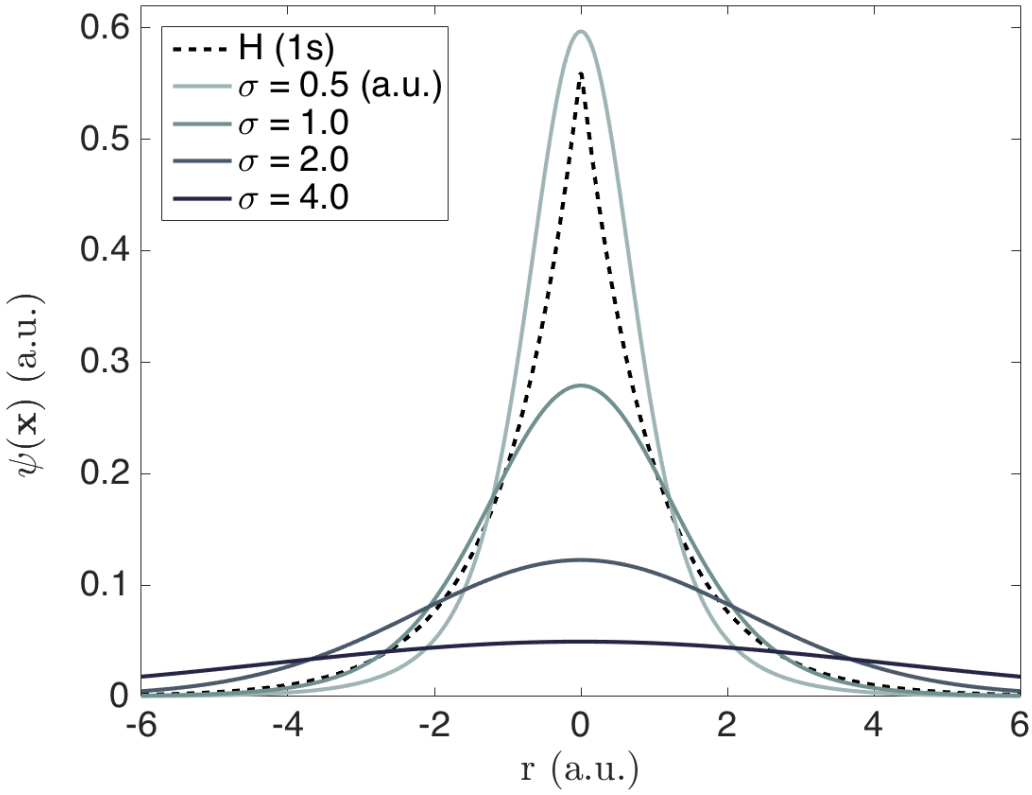

Figure 3.2: (Color online) The normalized configuration space wavefunction $\psi(|\mathbf{r}|)$ is given by the Fourier transform of Eq.(3.16) (shown here for $E_0 = .5$). The variable σ is used as a fitting parameter.

3.4 Field response in the length and velocity gauges

Equations (3.14a) and (3.14b) show that the time-dependent wavefunction, in the presence of a time varying field, can be recovered if the (gauge dependent) overlap functions $S_L(t)$, $S_V(t)$ are known. These in turn depend on integrals of the wavefunctions (see Eq.(3.7)). The advantage of the nonlocal potential model is that these integrals can be carried out analytically, resulting in Volterra (type II) integral equations for the functions $S_{L,V}(t)$.

This method reduces a 3+1 dimensional calculation of $\psi(\mathbf{x}, t)$ typically needed to find values of the wavefunction and observables of interest to a series of $\sim$ 2D calculations (the number of operations required to solve the integral equation in time grows like t^2). Further, since the wavefunction has been integrated analytically, the approach is not limited by spatial (or momentum) resolution or extent, which can present difficulties for finite difference solvers. Loosely speaking, the spatial/momentum dependence has been "integrated out" while encoding the wavefunction evolution through the time evolution of the complex variable $S(t)$.

The integral equation for $S_{L,V}(t)$ is found by multiplying Eqs.(3.14a), (3.14b) by $u(\mathbf{k})$ and integrating over all momenta. The resulting equation can be written in terms of a kernel function that depends on known quantities:

$$S_{L,V}(t) = \int_{-\infty}^{t} dt' K_{L,V}(t, t') S_{L,V}(t'). \tag{3.20}$$

The kernel $K_{L,V}$ is different in the length and velocity gauges:

$$K_L = iV_0 \left[\frac{2\pi}{\alpha(t,t')}\right]^{3/2} \ldots \tag{3.21}$$
$$\exp\left[-\sigma^2(\mathbf{A}^2 + \mathbf{A}'^2) + \frac{1}{2\alpha(t,t')}\left(i\Delta\mathbf{x} + \sigma^2(\mathbf{A}+\mathbf{A}')^2\right)\right],$$

$$K_V = iV_0 \left[\frac{2\pi}{\alpha(t,t')}\right]^{3/2} \exp\left[\frac{i\Delta\mathbf{x}}{2\alpha(t,t')}\right], \tag{3.22}$$

where

$$\alpha(t,t') \equiv 2\sigma^2 + i(t-t'), \tag{3.23}$$

and

$$\Delta\mathbf{x} \equiv \int_{t'}^{t} \mathbf{A}(t'')dt'' = \mathbf{x}(t) - \mathbf{x}(t'). \tag{3.24}$$

The variable $\Delta\mathbf{x}$ corresponds to the displacement of a classical electron in the presence of $\mathbf{A}$ from time t' to t (assuming the initial velocity $\mathbf{v}(t') = 0$). In obtaining (3.20)-(3.24), we have absorbed an overall spatially independent phase factor $\exp(\int_{t'}^{t} dt''\mathbf{A}^2(t''))$ into the definition of the wavefunction, which will not affect any results. The velocity gauge and length gauge kernels differ due to the explicit appearance of the potential, $\mathbf{A}(t), \mathbf{A}(t')$ in the length gauge kernel; all the field-dependence in the velocity gauge expression appears through the variable $\Delta\mathbf{x}$ (as was true for Eqs.(3.14a), (3.14b)).

3.4.1 Atomic dipole moment

The average momentum and time-dependent atomic dipole moment are defined as

$$\langle \mathbf{k} \rangle \equiv \int d^3\mathbf{k}' \phi^*(\mathbf{k}', t) \mathbf{k}' \phi(\mathbf{k}', t) \tag{3.25}$$

and

$$\begin{aligned} \langle \mathbf{p}(t) \rangle &\equiv -\int d^3\mathbf{x}' \psi^*(\mathbf{x}', t) \mathbf{x} \psi(\mathbf{x}', t) \\ &= -i \int d^3\mathbf{k}' \phi^*(\mathbf{k}', t) \nabla \phi(\mathbf{k}', t) \end{aligned} \tag{3.26}$$

In principle, the nonlinear dipole moment, including the effects of ionization, can be determined from the wavefunction given as the solution of Eqs.(3.14a), (3.14b). However, as shown in [31], it is computationally less intensive to solve for the dipole moment using the Ehrenfest relations. These are written as two first-order coupled ODE's with integral expressions for $S(t)$. In both length and velocity gauges:

$$\partial_t \langle \mathbf{k} \rangle = 2\mathrm{Im} \left[V S^*(t) \int_{-\infty}^{t} \mathbf{M}(t, t') S(t') \right] \tag{3.27}$$

$$\partial_t \langle \mathbf{p} \rangle = -\langle \mathbf{k} \rangle - \mathbf{A}(t) + 2\mathrm{Re} \left[V S^*(t) \int_{-\infty}^{t} \mathbf{L}(t, t') S(t') \right] \tag{3.28}$$

provided we use the definitions for the kernel terms $\mathbf{L}, \mathbf{M}, \mathbf{n}$,

$$\mathbf{L}_L(t, t') \equiv \sigma^2 \Big(\mathbf{n}_L(t, t') - \mathbf{A}(t) \Big) K_L(t, t') \tag{3.29}$$

$$\mathbf{M}_L(t, t') \equiv -\Big(\mathbf{n}_L(t, t') - \mathbf{A}(t) \Big) K_L(t, t') \tag{3.30}$$

$$\mathbf{n}_L(t, t') \equiv \frac{i\Delta\mathbf{x}(t, t') + \sigma^2 \Big(\mathbf{A}(t) + \mathbf{A}(t') \Big)}{\alpha(t, t')} \tag{3.31}$$

and

$$\mathbf{L}_V(t,t') \equiv \sigma^2 \mathbf{n}_V(t,t') K_V(t,t') \tag{3.32}$$

$$\mathbf{M}_V(t,t') \equiv -\mathbf{n}_V(t,t') K_V(t,t') \tag{3.33}$$

$$\mathbf{n}_V(t,t') \equiv \frac{i\Delta\mathbf{x}(t,t')}{\alpha(t,t')} \tag{3.34}$$

where subscript L, V indicate the length and velocity gauges respectively, using previous definitions for $\Delta\mathbf{x}$, α, and σ in Eqs.(3.23), (3.24). The velocity gauge expressions are again reductions of the length gauge expression where explicit appearances of the potential $\mathbf{A}(t)$ and $\mathbf{A}(t')$ are absent.

3.4.2 linear polarizability

In the low field regime, the (total) dipole moment in Eq.(3.26) can be characterized by the frequency dependent polarization

$$\hat{\mathbf{p}}(\omega) = \alpha(\omega)\hat{\mathbf{F}}(\omega) \tag{3.35}$$

where $\alpha(\omega)$ is the dynamic polarizability. Although generally a tensor, $\alpha(\omega)$ can be represented here by a scalar function because the nonlocal potential is isotropic in $\mathbf{k}$, $\mathbf{x}$ and is related to the electric susceptibility tensor $\chi^{(1)}(\omega)$ through the Clausius-Mossotti relation ([19]).

To obtain the expression for $\alpha(\omega)$ for the nonlocal potential model, we define

the following:

$$\mathbf{F}(t) = \hat{\mathbf{F}} e^{-i\omega t} + c.c.,$$

$$\mathbf{A}(t) = \frac{\hat{\mathbf{F}}}{i\omega} e^{-i\omega t} + c.c.,$$

$$\mathbf{p}(t) = \hat{\mathbf{p}} e^{-i\omega t} + c.c.,$$

$$\phi(\mathbf{k}, t) \rightarrow \left(\phi_0(\mathbf{k}) + \delta\phi(\mathbf{k}, t)\right) e^{iE_0 t},$$

$$\delta\phi(\mathbf{k}, t) \equiv \phi_-(\mathbf{k}) e^{-i\omega t} + \phi_+(\mathbf{k}) e^{i\omega t},$$

$$S_0 \rightarrow \left(S_0 + \delta S(t)\right) e^{iE_0 t},$$

and

$$\delta S(t) \equiv \int d^3\mathbf{k}' u^*(\mathbf{k}') \delta\phi(\mathbf{k}', t) = S_- e^{-i\omega t} + S_+ e^{i\omega t},$$

where ω is the frequency of the applied field, and we require $\mathbf{F}(t)$, $\mathbf{A}(t)$, and $\mathbf{p}(t)$ to be real quantities. The expressions above are inserted in a perturbative expansion of the Schrödinger equation (Eq. (3.11b)) and solved for $\delta\phi$ (discarding all higher order terms). The result is used in Eq.(3.26) to obtain the first order, frequency dependent dipole moment. For a linearly polarized monochromatic field $\mathbf{F}(t) = F_0 e^{-i\omega t} \hat{\mathbf{z}}$, one obtains the following for the velocity gauge treatment:

$$\phi_- = D(-\omega) \left[V_0 u(\mathbf{k}) S_- - \phi_0 \frac{k_z}{i\omega} \hat{F} \right],$$

$$\phi_+ = D(\omega) \left[V_0 u(\mathbf{k}) S_+ + \phi_0 \frac{k_z}{i\omega} \hat{F}^* \right],$$

where

$$D(\pm\omega) \equiv \left(E_0 + \mathbf{k}^2/2 \pm \omega\right)^{-1}.$$

With some algebraic manipulation one finds expressions for $\hat{\mathbf{p}}_{\pm}$, e.g:

$$\hat{\mathbf{p}}_{-} = -\int d^3\mathbf{k}\; D(-\omega)\phi_0\left(\partial_{k_z}\phi_0\right)\frac{k_z}{\omega}\hat{F} + \int d^3\mathbf{k}\; D(\omega)\phi_0\left(\partial_{k_z}\phi_0\right)\frac{k_z}{\omega}\hat{F}.$$

A similar expression can be found for $\hat{\mathbf{p}}_{+}$. The polarizability is then given by the expression:

$$\alpha_V(\omega) = \int d^3\mathbf{k}\left[D(\omega) - D(-\omega)\right]\phi_0\left(\partial_{k_z}\phi_0\right)\frac{k_z}{\omega}, \tag{3.36}$$

and the length gauge polarizability is found by the same method to be

$$\alpha_L(\omega) = \int d^3\mathbf{k}\left[D(\omega) + D(-\omega)\right]\left(\partial_{k_z}\phi_0\right)^2. \tag{3.37}$$

Equations (3.36) and (3.37) are evaluated in the limit $\omega \to 0$ in Fig 3.3 to show the static (DC) polarizability as a function of the fitting parameter σ. In the limit $\sigma \to 0$, the gaussian nonlocal potential is equivalent to an attractive delta function potential, and the polarizability is observed to limit to a non-zero gauge-independent value. If σ is increased, the length gauge static polarizability is observed to be much greater than that in the velocity gauge formulation. For comparison, the established (non-relativistic) values of the static polarizability for several atomic species are as follows, all in atomic units (a.u.): hydrogen: 4.5, helium: 1.38, neon: 2.68, and argon: 11.10 [41].

In Figs.3.4 and 3.5, $\alpha(\omega)$ is evaluated via Eqs.(3.36) and (3.37) (solid lines) and plotted as a function of laser frequency for various values of sigma. The polarization is real for $\omega < E_0$ but complex for $\omega > E_0$. To evaluate $\alpha(\omega)$ for $\omega \geq E_0$ the

laser frequency, previously defined as real, is allowed to become slightly complex, $\omega \to \omega + i\delta$ accounting for causality. It should be noted that systems with additional eigenstates would have additional resonances for coupling to excited states, e.g. for hydrogen: $\omega_{res} = E_0(1-1/n^2)$. These are not present in a single bound state system. The cross marks in Figs. 3.5 and 3.4 represent the $\alpha(\omega)$ calculated from numerical simulation via Eqs.(3.25) and (3.26). Each cross represents the atomic dipole calculated for a 50 femtosecond low intensity pulse ($I_{\max} = 1 \times 10^{10}$ W/cm^2), and the ratio taken of Fourier transform coefficients $\hat{\mathbf{p}}(\omega), \hat{\mathbf{F}}(\omega)$. Agreement is observed between the predicted and simulated values.

3.4.3 Ionization

The time-dependent bound-electron probability is defined as

$$\rho(t) \equiv \left| \int d^3\mathbf{x}' \; \psi_0^*(\mathbf{x}')\psi(\mathbf{x}', t) \right|^2 = \left| \int d^3\mathbf{k}' \; \phi_0^*(\mathbf{k}')\phi(\mathbf{k}', t) \right|^2 ; \tag{3.38}$$

we may use this to define the time-dependent ionization rate $\nu(t)$ through the relation

$$\rho(t) = \rho(t_0) \exp\left[- \int_{t_0}^{t} \nu(t')dt' \right], \tag{3.39}$$

that depends functionally on the field $\mathbf{F}(t)$.

In practice, it is often easier to use functions other than $\rho(t)$ that are approximately equal to the bound probability defined by Eq. (3.38). For the nonlocal potential, we use the quantity

$$\rho_u(t) \equiv \left| \frac{S(t)}{S_0} \right|^2 \propto \left| \int d^3\mathbf{k}' \; u^*(\mathbf{k}')\phi(\mathbf{k}', t) \right|^2 \tag{3.40}$$

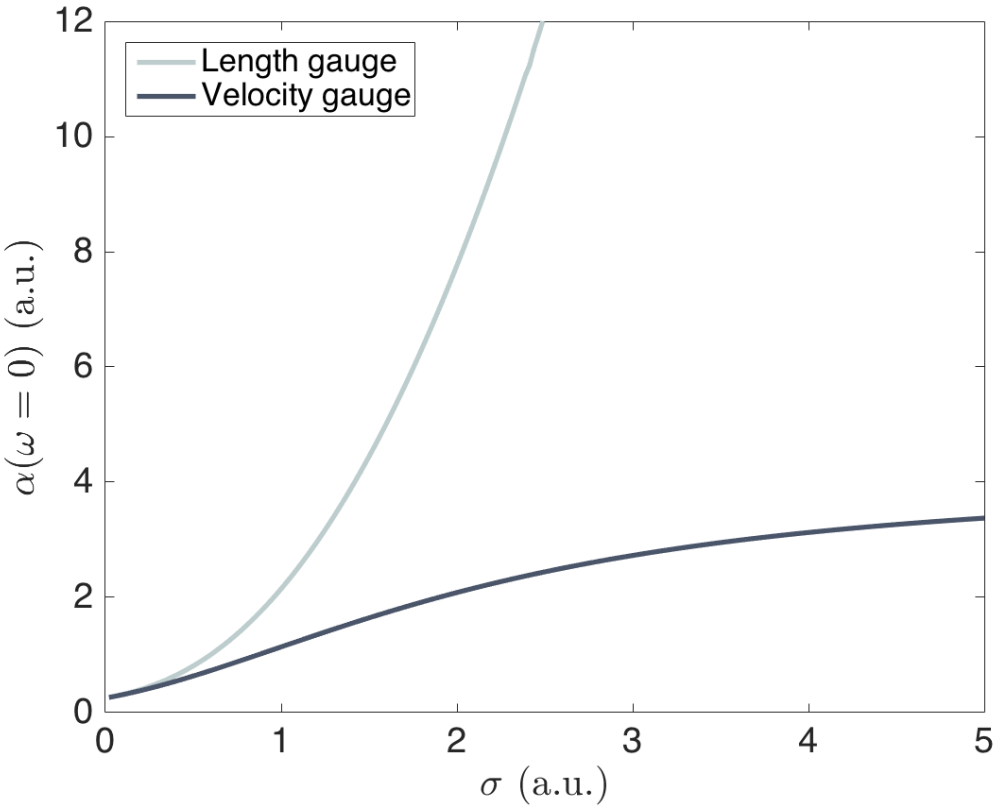

Figure 3.3: (Color online) The static polarizability $\alpha(\omega = 0)$ as calculated from Eqs. (3.36) and (3.37). In the limit $\sigma \to 0$, the nonlocal potential is equivalent to a (local) delta potential, and the polarizability is gauge-independent. For positive values of σ, the length-gauge system is more easily polarized by a (DC) applied electric field.

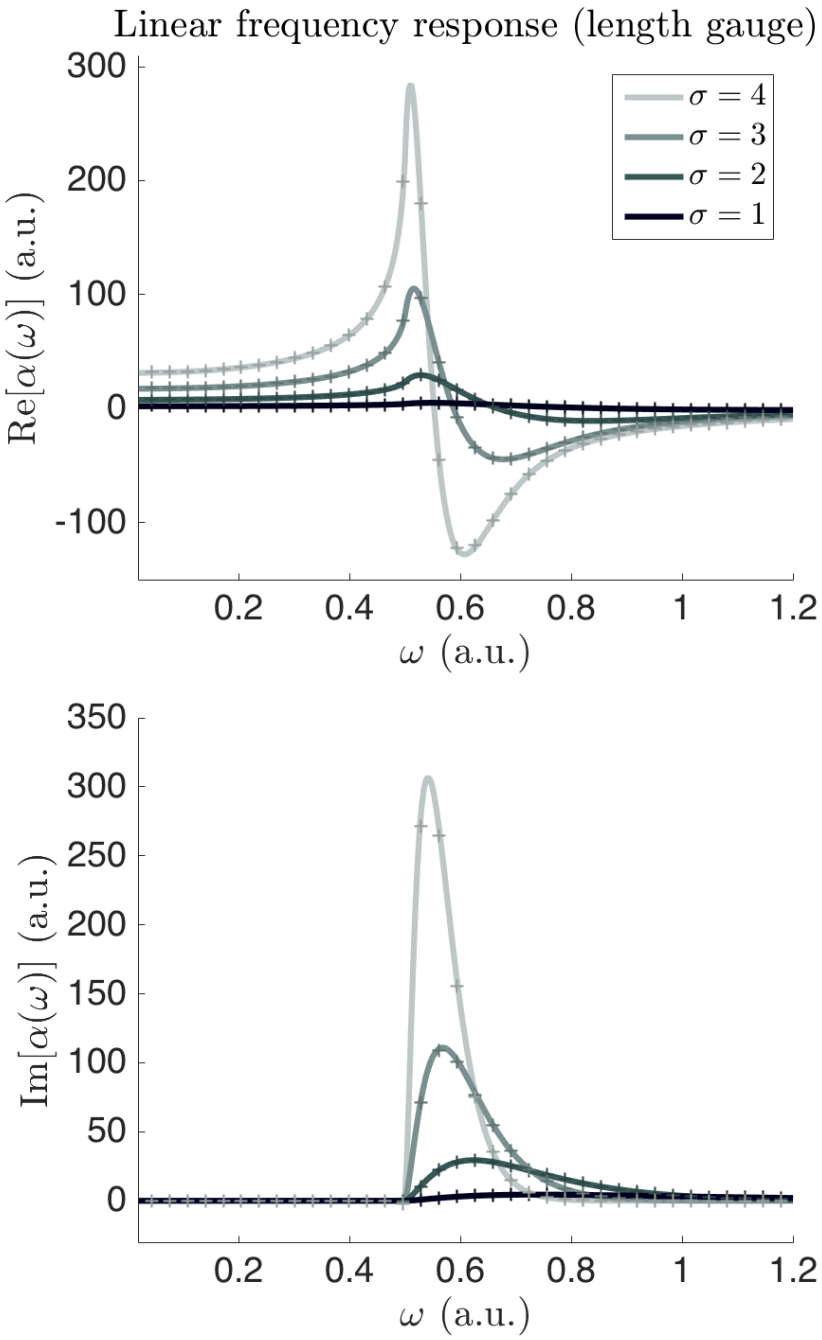

Figure 3.4: The dynamic polarizability in the length gauge, with a single photon resonance at $\omega = E_0$ The solid lines represent the $\alpha(\omega)$ given by Eq. (3.37) ($\omega \geq E_0 \rightarrow \omega + i\delta$), and the crosses represent the simulated low field response via the total dipole (Eq.(3.26)).

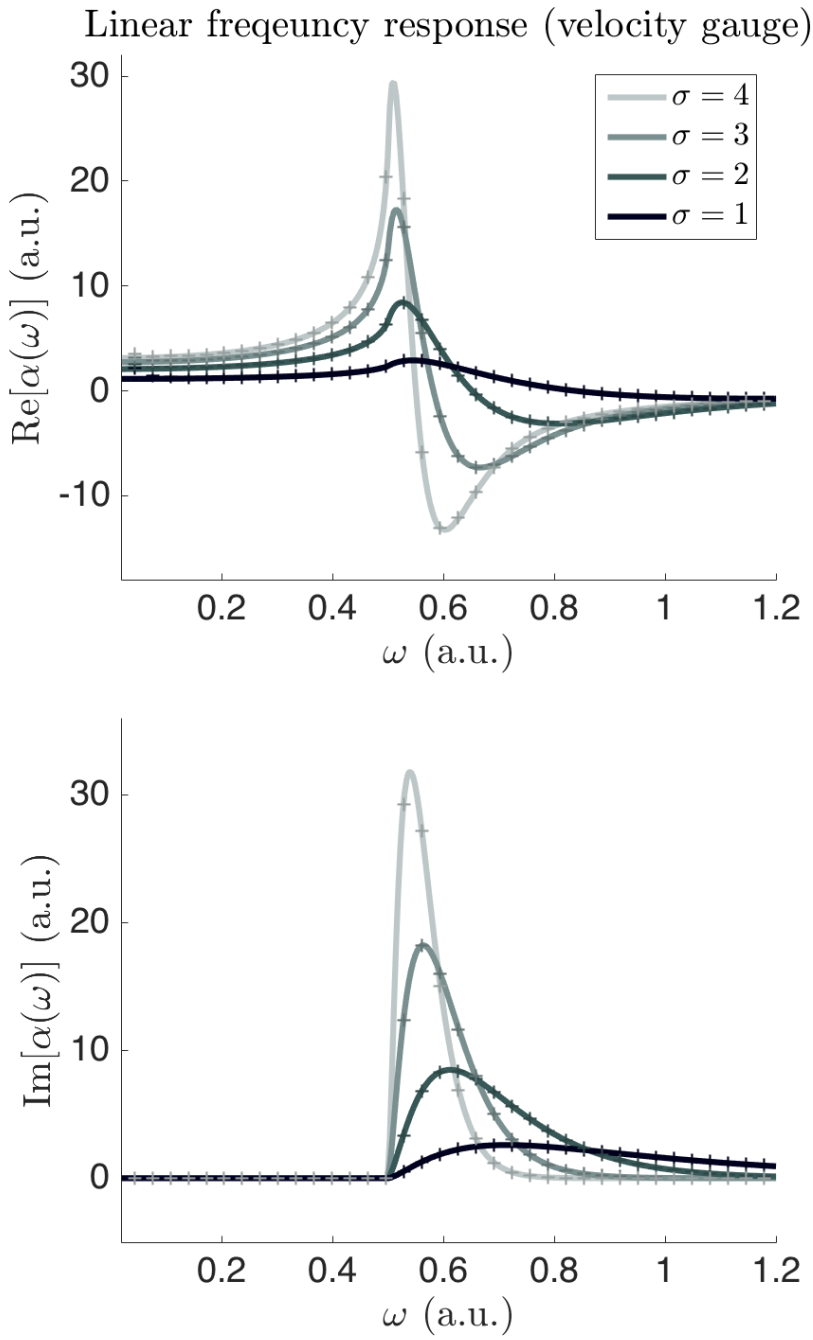

Figure 3.5: The dynamic polarizability in the velocity gauge, with a single photon resonance at $\omega = E_0$ The solid lines represent the $\alpha(\omega)$ given by Eq.(3.36) ($\omega \geq E_0 \rightarrow \omega + i\delta$), and the crosses represent the simulated low field response via the total dipole (Eq.(3.26)).

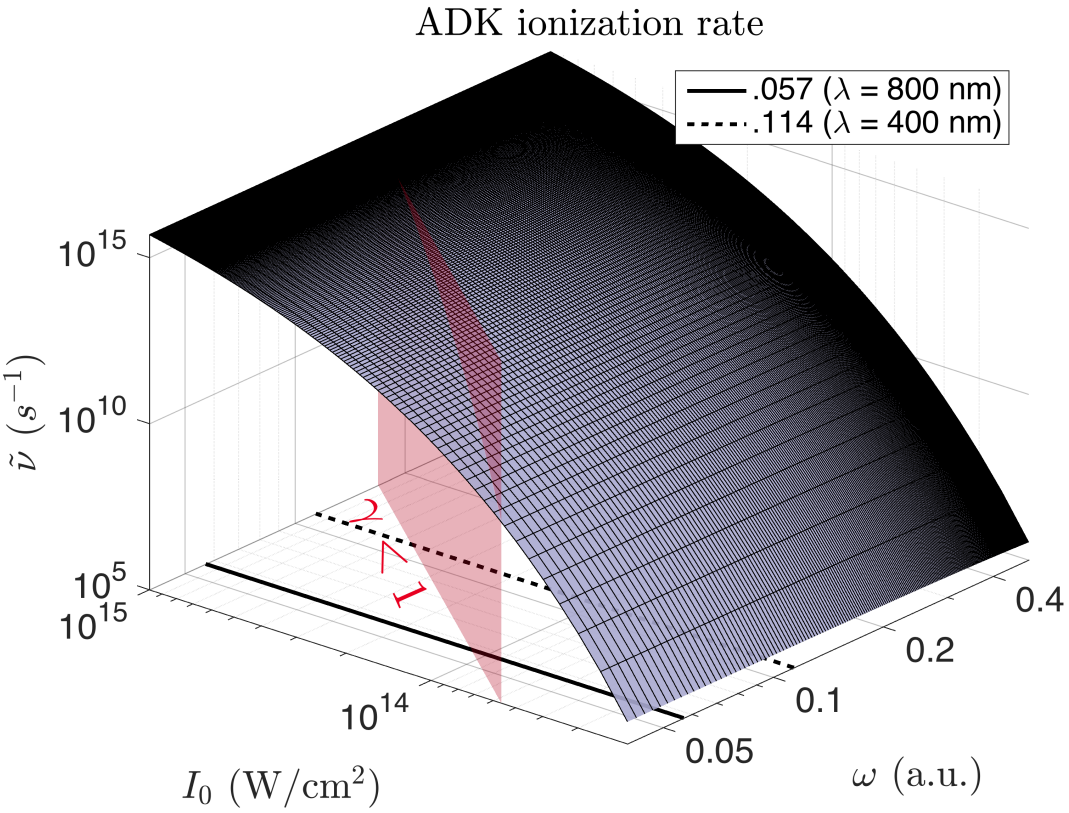

Figure 3.6: The ADK tunnel rate [1] plotted as a function of laser frequency and intensity. Although the ADK rate includes a rate correction for the Coulomb potential, and therefore increased accuracy in the tunnel regime ($\gamma << 1$), it does not account for the frequency dependence, and underestimates the ionization rate for $\gamma >> 1$ by orders of magnitude.

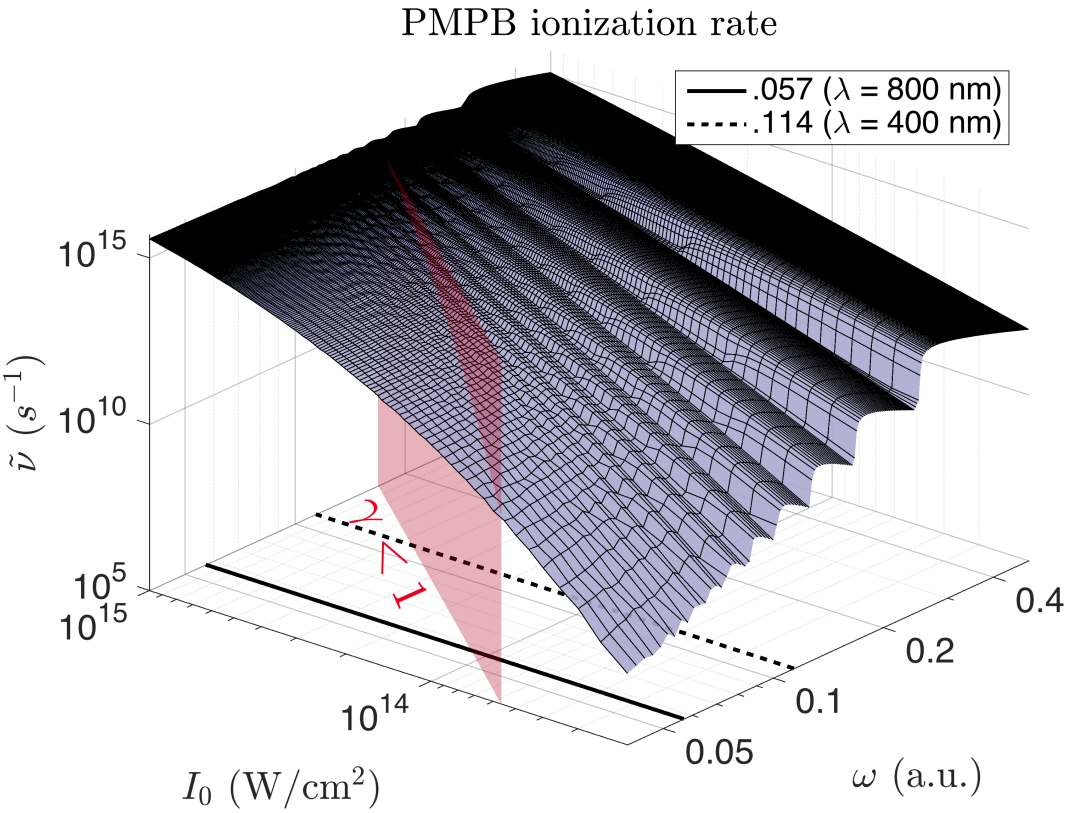

Figure 3.7: The PMPB ionization rate [2] as a function of laser frequency and intensity (100×100 data points, interpolated). The PMPB rate is designed to be valid in the (non-relativistic) single active electron approximation for any value of the Keldysh parameter, γ.

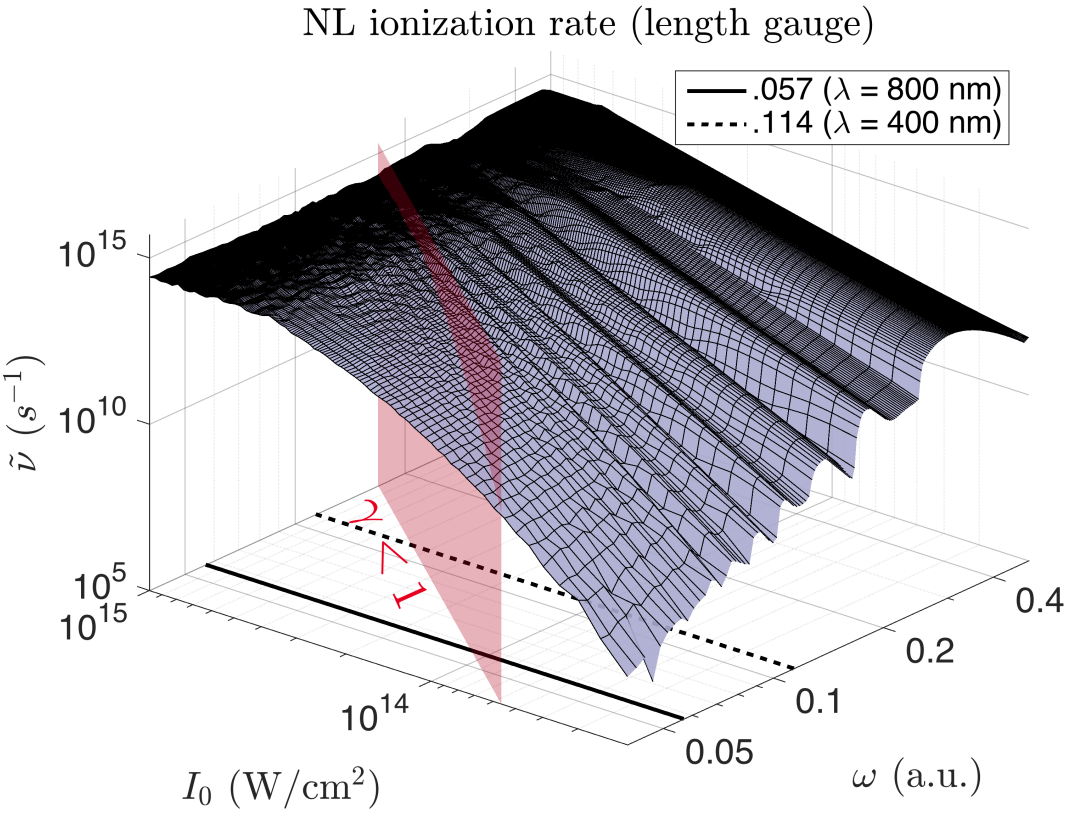

Figure 3.8: The ionization rate predicted via the nonlocal potential length gauge formulation as a function of laser frequency and intensity (100 × 100 data points, interpolated). The length gauge formulation compares favorably with the rate predicted by the PMPB rate model.

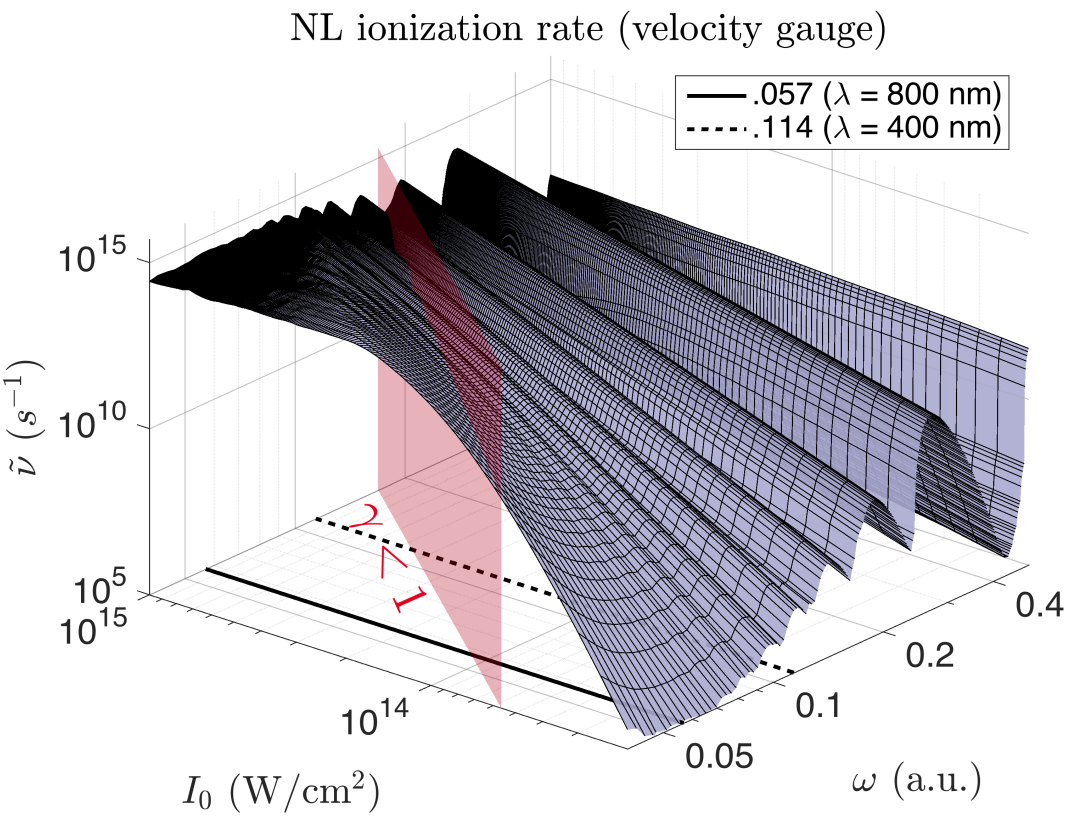

Figure 3.9: The ionization rate predicted by the nonlocal velocity gauge formulation as a function of laser frequency and intensity (100 × 100 data points, interpolated). The velocity gauge ionization rate generally underestimates in the multiphoton regime and overestimates in the tunnel regime. Slices along constant intensity and frequency are shown in Figs.3.11 and 3.10 for direct comparison.

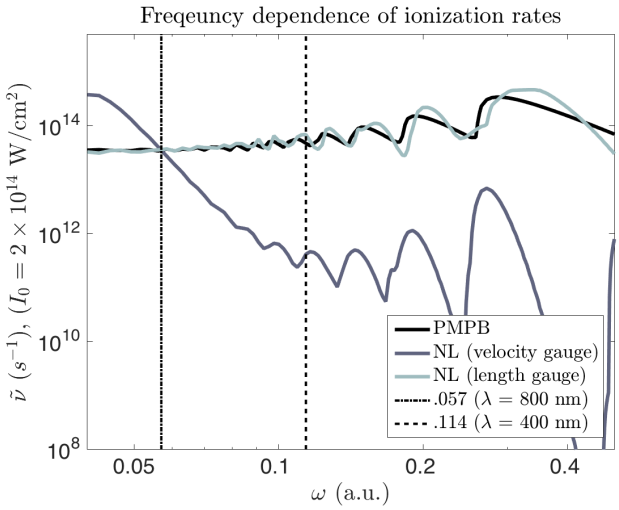

(a)

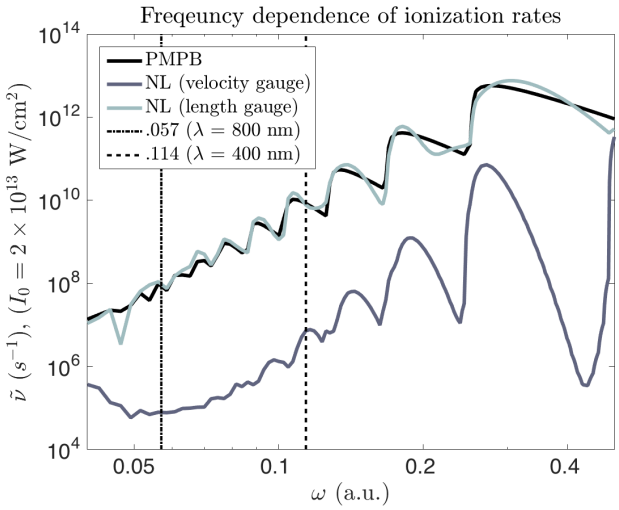

(b)

Figure 3.10: The ionization rate as a function of intensity for $I_0 = 2 \times 10^{14}$ W cm^{-2} (3.10(a)); the values of σ for the length and velocity gauge potentials were calibrated at this intensity, at 800 nm (visible here as the crossing point for all rates). The velocity gauge overestimates the rate towards tunnel regime and underestimates it in the multiphoton regime, while the PMPB and length gauge rates predict similar rates. The rates are also plotted for $I_0 = 2 \times 10^{13}$ W cm^{-2} (3.10(b)).

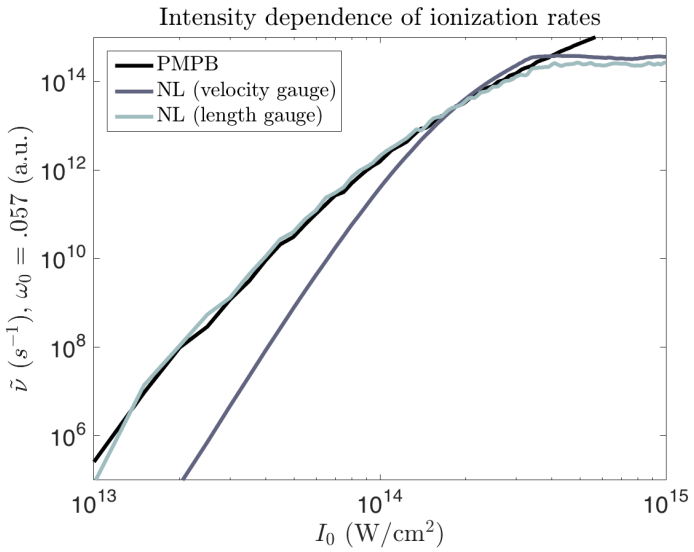

(a)

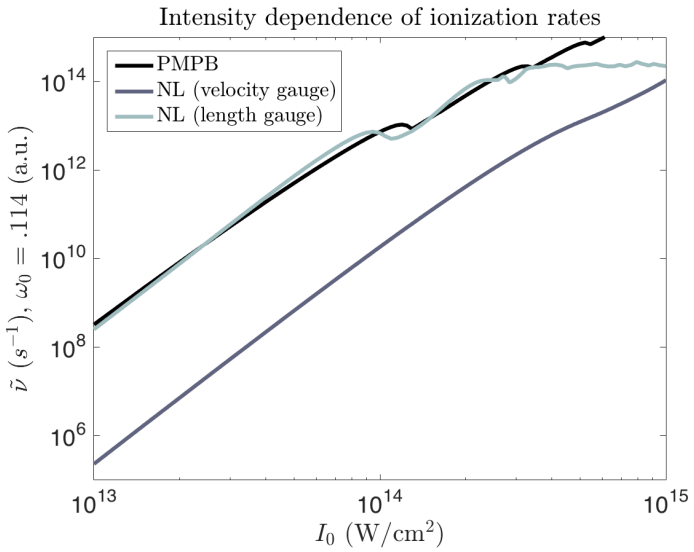

(b)

Figure 3.11: The PMPB photoionization rate and nonlocal (length gauge) rate also show agreement as a function of intensity for 800 nanometer light; the velocity gauge ionization rate does not (3.11(a)). At 400 nm (3.11(b)), the velocity gauge ionization rate has the same power dependence as the length gauge and PMPB rates, but strongly underestimates the magnitude for the chosen fitting parameter ($\sigma = 4.785$).

for convenience, noting that the functions $u(\mathbf{k})$ and $\phi_0(\mathbf{k})$ are similar in functional form, and note the limit $E_0 \to \infty$, $\rho_u(t) \to \rho(t)$. Although these measures are not identical, any wave density that escapes the nonlocal potential region quickly propagate away from the origin, making $\rho_u(t)$ a very good approximation of the bound probability. A comparison of these quantities was rather carefully examined in previous work [31] which demonstrated $\rho_u(t)$ and $\rho(t)$ were in agreement in the length gauge formulation. The quantity $\rho_u(t)$ does not offer such a straightforward interpretation in the velocity gauge, but can be used as a measure of bound probability for times when $\mathbf{A}(t) = 0$, and can be used for measuring pulse averaged ionization rates.

We compare the length and velocity gauge predicted ionization rates using a flat-top laser pulse of form $\mathbf{E}(t) \equiv F(t)\cos(\omega t)\hat{\mathbf{z}}$ with a 15 femtosecond ramp-time (t_r) of the form

$$F(t) \equiv \begin{cases} F_0 \sin^2(\frac{\pi}{2t_r}t) & \text{for } 0 \le t \le t_r \\ F_0 & \text{for } t_r < t \le t_p - t_r \\ F_0 \cos^2(\frac{\pi}{2t_r}(t - t_p + t_r)) & \text{for } t_p - t_r < t \le t_p \end{cases} \tag{3.41}$$

where t_r is the ramp time to maximum and t_p is the total pulse length, with values of 15 and 90 femtoseconds respectively. This pulse profile was used in place of a gaussian or $\sin^2(t)$ envelope to maximize the time the electric field amplitude was at a fixed value while still maintaining a narrow bandwidth to prevent frequency dependent structure in the ionization rate from being averaged out. The total drop in bound probability $\rho_u(t_f)$ (Eq. (3.40)) is used to calculate a pulse averaged

ionization rate

$$\tilde{\nu} = -\frac{ln\left[\rho(t_f)\right]}{t_p - t_r}. \tag{3.42}$$

Figures 3.7, 3.8, 3.9 show the ionization rate $\tilde{\nu}$ landscape as a function of the near infrared to near ultraviolet laser frequency at ionizing intensities, spanning the multiphoton and tunnel ionization regimes. The length gauge and velocity gauge rates are compared with an ionization rate model introduced by Popruzhenko, et. al. in 2008 [2], here referred to as the "PMPB" rate, in reference to the authors' names. The PMPB rate used for comparison here is preferable to Keldysh or ADK models [1, 29, 42] which are known to underestimate the multiphoton ionization rate by several orders of magnitude; the PMPB model is valid in both the tunneling and multiphoton regimes and was shown to give good agreement with both Floquet and *ab initio* TDSE solver simulations [2].

To compare the ionization rate predicted by the nonlocal potential, the tuning parameter σ was fixed by matching the ionization rate of a single run with typical laboratory parameters $\omega = .057$ [a.u.] (800 nm), and $F_0 = .01$ [a.u.] (Intensity of 2×10^{14} W/cm^2), seen as the crossing point of all rates in Fig. 3.10(a). The values $\sigma = 2.482$ for the length gauge and $\sigma = 4.785$ for the velocity gauge were used in all ionization plots shown.

A glance at Figs. 3.7 and 3.8 reveal that the nonlocal length gauge and PMPB rates share the same general contours across the entire range of intensities and frequencies shown here. Slices taken along lines of constant frequency (3.11(a), 3.11(b)) and constant intensity (3.10(b), 3.10(a)) give a more direct comparison

and show strong agreement in the PMPB and length gauge ionization rates for all frequencies examined and intensities up to $I_0 \sim 4 \times 10^{14}$ W/cm^2. The deviation above this intensity is only apparent; calculation of the $S(t)$ always leaves residual traces which artificially decrease $\tilde{\nu}$. The PMPB and nonlocal length gauge predict similar ionization rates for all laser parameters shown. It should be stated that the agreement in ionization rate shown in these plots is, in some cases misleading; neither the PMPB nor the nonlocal model here can account for ionization pathways that include intermediate population of excited electron states, [43].

By contrast, the velocity gauge ionization rate does not agree with the PMPB rate; it underestimates ionization below $I_0 = 2 \times 10^{14}$ W/cm^2 and overestimates it for higher intensities; for this reason, it is unlikely that a different choice of σ could improve the predicted rate in the tunnel and multiphoton regimes (the rate generally changes monotonically with the tuning parameter σ for a specified electric field). This under-prediction at low intensities and over prediction at high-intensities for the velocity gauge formulation is consistent with other work [39] which examined the ionization rate of a similar nonlocal model in the velocity gauge.

3.5 Summary of chapter 3

In this chapter, we examine the gauge dependence of the gaussian nonlocal model atomic potential. We note that the utility of this model is that the atom-field interaction can be computed in the time domain without having to resolve the spatial or momentum space wavefunction, allowing for rapid evaluation of e.g., the

atomic dipole moment and photoionization rate.

Specifically, we consider the linear dipolar field response and photoionization rate predicted by the introduced nonlocal potential in the length and velocity gauges in a time varying electric field. All examined quantities are found to be gauge dependent. At low intensities ($I \sim 10^{10}$ W cm^{-2} and below), both gauge formulations exhibit similar resonant frequency response at photon energies near the ionization threshold, and a static polarizability in the low frequency limit, but differ significantly in magnitude. The photoionization rates predicted in each gauge were compared with the Coulombic photoionization rate model (PMPB) [2], in the frequency (near IR to near UV) and intensity domains ($I \sim 10^{13} - 10^{15}$ W cm^{-2}). It was found that, although gauge formulations demonstrate multiphoton resonance and tunnel features, the velocity gauge formulation generally over estimated the tunnel ionization rate and underestimated the multiphoton ionization rate; the length gauge and PMPB photoionization rates agreed well over the entire parameter range investigated.

Chapter 4: Modeling THz generation

One subject of topical interest that may be examined with the nonlocal model is the two-color method of generating terahertz (THz) frequency radiation. Controlled, coherent THz radiation is of interest in several prospective and current applications, including security and defense imaging, atomic and molecular spin manipulation, environmental monitoring, and ultrafast computing [44, 45]. Such applications continue to drive interest in exploring various mechanisms for producing THz radiation. One such method that generates pulsed broadband (0.3-3mm wavelength) THz frequency radiation is the so-called "two-color" method, relying on laser-gas interaction at ionizing intensities [10, 11, 46, 47]. Although laser pulse evolution and propagation effects also shape factors of the resulting THz radiation, the basic mechanism can be explained in terms of the interaction of a single atom or molecule in the presence of the (ionizing) laser electric field. In this chapter we examine the microscopic theory of THz generation via the nonlocal gaussian atomic model.

4.1 (Classical) photocurrent model of two-color THz generation

We briefly consider the microscopic photocurrent model (PCM) of two-color THz radiation, as originally proposed by Kim, *et. al.* in [9]. For a neutral gas of identical non-interacting atoms or molecules under the influence of a high field (ionizing) time-dependent electric field, we can write the free electron population as:

$$n_e(t') = n_0 \left[1 - \exp\left(- \int_0^{t'} \nu(t'')dt'' \right) \right], \tag{4.1}$$

where n_0 is the neutral gas density before arrival of the laser pulse (here taken to be $t = 0$) and ν is the field dependent ionization rate, n_b is the bound population of electrons, where

$$n_0 = n_e + n_b. \tag{4.2}$$

For the population of electrons ionized in the infinitesimal interval $\delta t'$,

$$\delta n_e(t') = \nu(t') n_b(t') \delta t', \tag{4.3}$$

subsequent motion is assumed to be given by the influence of the applied laser field only, so that electrons ionized at t' have a velocity at t given in terms of the electric field $\mathbf{E}(t)$ and vector potential $\mathbf{A}(t)$ (and $q_e = -1, m_e = 1$ in atomic units)

$$\mathbf{v}(t, t') = \mathbf{v}(t') - \int_{t'}^{t} \mathbf{E}(t'')dt'' = \mathbf{v}(t') + \mathbf{A}(t) - \mathbf{A}(t'), \tag{4.4}$$

and current contribution

$$\delta \mathbf{j}(t, t') = -\delta n_e(t') \mathbf{v}(t, t') = -\delta n_e(t') \left(\mathbf{A}(t) - \mathbf{A}(t') \right), \tag{4.5}$$

where we have assumed the velocity at the moment of ionization, $\mathbf{v}(t')$, to be zero. The total current $\mathbf{J}(t)$ is given by the accumulated current contributions:

$$\mathbf{J}(t) = \int_0^t \delta\mathbf{j}(t,t') = -\int_0^t dt'\nu(t')n_b(t')\left(\mathbf{A}(t) - \mathbf{A}(t')\right). \tag{4.6}$$

In this expression for the total current, the term proportional to $\mathbf{A}(t)$ represents the current of the quiver motion of free electrons at the optical frequency, while the term proportional to $\mathbf{A}(t')$ is a drift current that depends on the initial time of ionization. If conditions are such that this drift current accumulates over a timescale of ($2\pi/\omega_{\mathrm{THz}} >> 2\pi/\omega_0$), this will be a source of radiation in the THz frequency range. A monochromatic pulse alone is inefficient at generating such a drift current. Consider two contributions $\delta\mathbf{j}$ centered about the laser field peak at $t = 0$, where $\mathbf{E}(t) = \mathbf{E}_\omega \cos(\omega t)$, $\mathbf{A}(t) = \mathbf{A}_\omega \sin(\omega t)$. Via Eqs. (4.4) and (4.5), the sum of their contribution is approximately

$$\delta\mathbf{j}(t,-t') + \delta\mathbf{j}(t,t') = -\nu(t')n_b\left(2\mathbf{A}(t) - \mathbf{A}(-t') - \mathbf{A}(t')\right), \tag{4.7}$$

where we have assumed the bound electron population has not depleted significantly, so that $n_b(-t') \approx n_b(t')$. Because the ionization rate is even about the peak, $\nu(-t') = \nu(t')$ and the vector potential odd, $\mathbf{A}(t') = -\mathbf{A}(-t')$, the net effect is the last two terms in Eq.(4.7) cancel, and there is no drift current contribution. Every such pair of currents δj will (approximately) cancel pairwise by the same symmetry argument, such that the drift current for a monochromatic pulse tends to be small, as calculated by the PCM.

In the two-color model, a second harmonic is added to the fundamental, usually achieved with a frequency doubling optic (such as a BBO crystal), so the field is of

form:

$$\mathbf{E}(t) = \mathbf{E}_{\omega}(t)\cos(\omega t + \phi) + \mathbf{E}_{2\omega}(t)\cos\left(2(\omega t + \phi) + \phi_{rel}\right), \tag{4.8}$$

where ϕ_{rel} is the relative phase between the fundamental and second harmonics, and ϕ determines the phase between the first harmonic and the envelope. For phases $\phi_{rel} = n\pi$, the field is still symmetric about the peaks, and the current and ionization rate cancellation argument above will hold. If ϕ_{rel} takes on different values, an asymmetry is introduced in their contribution to Eq. (4.6), and a total drift current will generally accumulate, acting as a source term for THz radiation. The total current $\mathbf{J}(t)$ is depicted in Fig. 4.1 for the scenario of a single color, two-colors with $\phi_{rel} = 0$, and two-colors with $\phi_{rel} = \pi/2$. Additional effects may also play a significant role in creating a drift current in the PCM model, such as carrier-envelope phase, and electron ionization depletion.

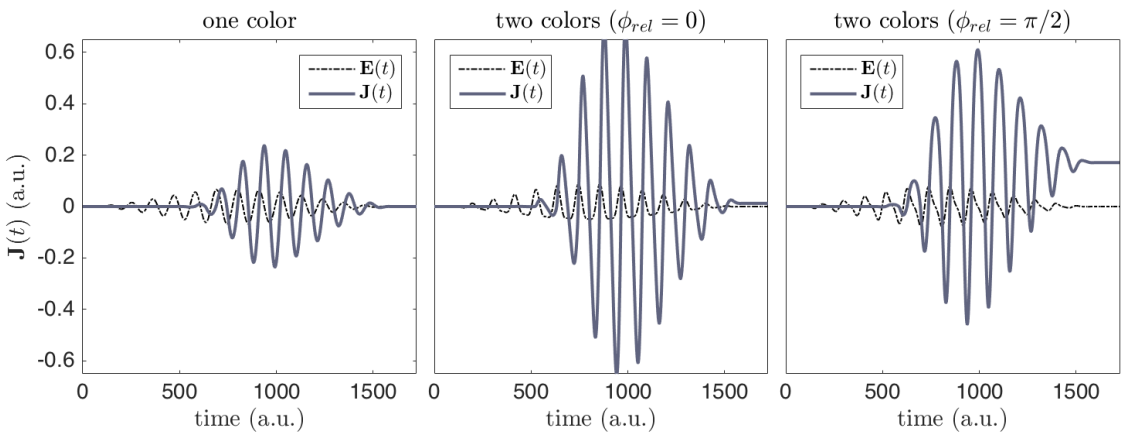

Figure 4.1: Illustration of the photocurrent model (PCM) of two-color THz generation, using the ADK rate [1] to model tunnel ionization. The first two panes depict single color and two-color laser pulses with symmetric peaks with weak residual drift current ($\mathbf{J}(t_f)$); the small residual drift current (RDC) seen in the second pane can be attributed to the effect of depletion that was neglected in the analysis above. The third pane illustrates that a slowly rising drift current can be strongly driven when $\phi_{rel} = \pi/2$, acting as a source for low (THz) frequency radiation.

4.2 Quantum mechanical description of two-color THz generation

The photocurrent model (PCM) above gives a simple and successful explanation for the underlying Terahertz radiation mechanism, but neglects effects that may be significant in the post-ionization dynamics of the electron (or electron wavefunction) including: the initial condition of the classical electrons at the moment of ionization (often assumed to be $\mathbf{v}(t') = 0$), the linear and nonlinear neutral atomic response, and subsequent recollisions with the ion post-ionization. Many of these processes have been the subject of recent examination [10, 48]. Because of the unknowns in patching the quantum mechanical tunneling process to classical electron trajectories, it may be preferable to use a fully quantum mechanical simulation.

In the quantum mechanical picture, the average current from the motion of the electron wavefunction is given by

$$\mathbf{J}(t) \equiv n_0 \partial_t \langle \mathbf{p}(t) \rangle, \tag{4.9}$$

where the current is weighted by the neutral (total) gas density. There is no need to identify the population of free electrons n_e in this case, as the wavefunction (and therefore) average current includes all such contributions.

The plots in figure 4.2 compare the results using the nonlocal potential model with the photocurrent model as described in the previous section. Each grid square represents a simulation of a two-color (800nm, 400nm) 90 fs full-width sine-squared envelope with intensity ratio $I_{2\omega}/I_{\omega} = .1$. The residual drift current (RDC, or J_{drift}) is shown as a function of I_{ω} (vertical axis) and relative phase ϕ_{rel}, normalized by

$|\mathbf{J}_{max}|$ (right). At the intensities plotted (ionization $\geq 1\%$), the RDC (Fig 4.2) is the dominant source of THz radiation (0-100 THz, Fig.4.3). Both the PCM and the nonlocal quantum mechanical results suggest the optimum phase for radiation is given by roughly $\phi_{rel} = \pi/2, 3\pi/2$, slightly decreasing as intensity increases to 1×10^{15} W cm^{-2}.

Many of the features are strongly correlated with the ionization rate. At the lowest intensities, the ADK tunnel under-predicts the ionization rate as it moves into the multi-photon regime $\gamma_{kel} > 1$; this is responsible for the decreased maximum THz yield at low intensities. For the simulations shown, ionization saturates at about $I = 2 \times 10^{14}$ W cm^{-2}. Both the PCM and nonlocal model predict a $\sim 30\times$ enhancement of the THz power compared with a single color pulse at the same intensity and pulse duration (not shown).

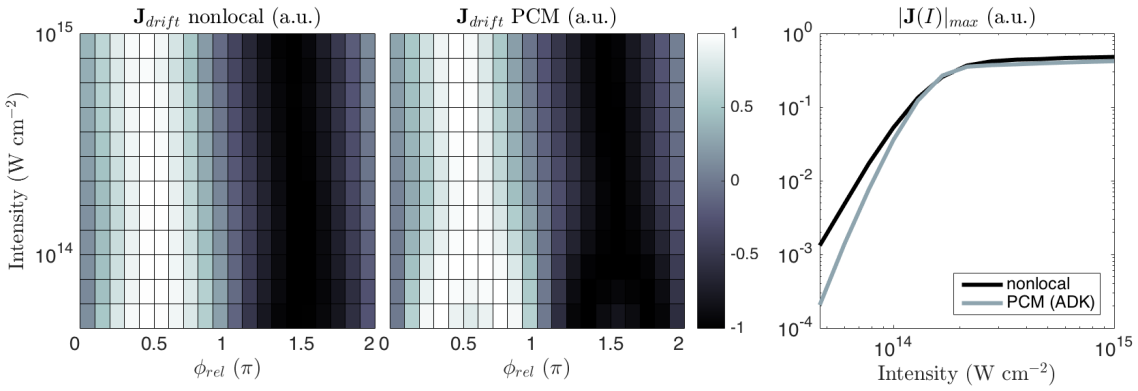

Figure 4.2: Each grid cell represents a simulation for which the final residual current is plotted as a function of relative phase and intensity. In the first pane, results of the nonlocal model are shown, and the PCM using the ADK ionization rate are shown in the second. The color map is normalized along each intensity line to make trends easier to see. Along each row (constant intensity), $|\mathbf{J}|_{max}$ is plotted in the third pane. The PCM and nonlocal model are in general agreement. The PCM predicts a lower drift current for low intensities because the ADK rate model underestimates ionization for low intensities.

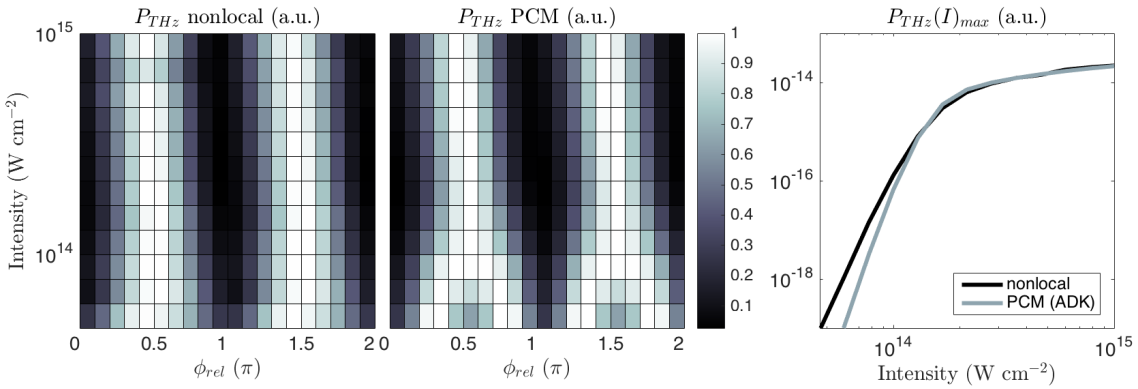

Figure 4.3: For the same data plotted in Fig. 4.2, the radiated power is integrated over (0-100) THz. The value $|\mathbf{J}_{drift}|$ is strongly correlated with the THz radiation. At the lowest intensity (4×10^{13} W cm^{-2}), the ADK tunnel ionization rate is not well justified, and begins to display four peaks in the THz yield that is not observed with the nonlocal model or *ab initio* simulation; the single color Keldysh parameter values are $\gamma_\omega \approx 1.6$, $\gamma_{2\omega} \approx 10.0$, where the the tunnel rate is valid for $\gamma << 1$.

4.3 Electron rescattering in the two-color method

One of the largest omissions of the PCM is the process of electron rescattering. Following ionization, some fraction of electrons (or wavepackets, in the quantum mechanical description) return and make subsequent passes across the parent ion, and continue to make passes in the vicinity of the Coulomb potential under the influence of the applied electric field. The characteristic electrostatic field strength $1(\text{au}) = \sim 5 \times 10^{11}$ V m^{-1} (the Coulomb field value at the Bohr radius) may be up to an order of magnitude larger than the laser field values, even at the onset of ionizing intensities ($|\mathbf{E}| \approx 2.7 \times 10^{10}$ V m^{-1} at I $> 10^{14}$ W cm^{-2}), suggesting that it may play a significant role.

Figure 4.4 depicts the effect of rescattering in a 1D nonlocal potential TDSE simulation (vertical axis position, horizontal axis time). Although the image shown is for a single color, it can be observed that with each half-cycle of the laser pulse, initially ionized wavefunction packets return to the scattering core and interfere on subsequent laser pulses. This may be observed by the striations in the electron probability density depicted in the colormap. To investigate the relevance of this effect, we examine the two-color THz process with *ab initio* simulations that are found throughout this section. The wavefunction is simulated with the turboWAVE FDTD code [4] on a 2D domain, $(r_\perp \times z)$, where $z_{max}(\text{au})$ is given by the classical electron drift distance, $(z_{max} \approx |\mathbf{A}|_{max}\tau_{pulse})$ and comparable value for $r_{\perp,max}$.

The dependence of the RDC on peak laser intensity and second harmonic phase, ϕ_{rel} is examined in Fig. 4.5. There, two-color simulations were performed,

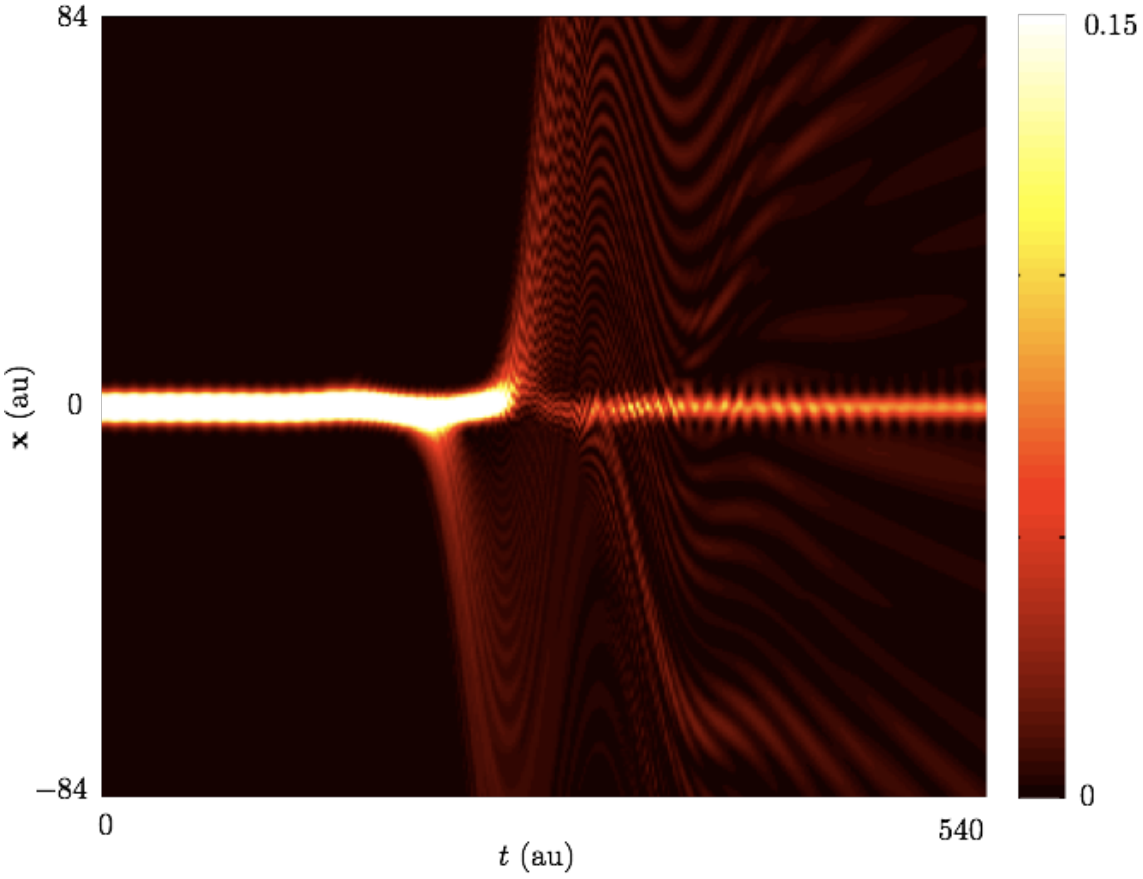

Figure 4.4: This nonlocal model was formulated in one-dimension, and the electron probability density $|\psi(x,t)|^2$ is shown as a function of time (horizontal axis) and displacement (vertical axis), subject to a field at 5×10^{14} W cm^{-2}, few-cycle (single color) pulse. Although the striations demonstrate that scattering occurs when electron wavepackets return to the potential, the scattering cross section is short-range (gaussian radial dependence), weaker than the Coulomb potential.

for a 40 fs sine-squared laser pulse envelope with relative intensity $I_2/I_1 = 0.1$. At high intensities ($> 4\times10^{14}$ W cm^{-2}), the electron wavefunction is almost completely ionized, and the *ab initio*, PCM, and nonlocal models are seen to give approximately the same maximal drift current values. At low intensities ($< 1 \times 10^{14}$ W cm^{-2}), as previously stated, the PCM model predicts lower RDC largely because it underpredicts the ionization rate (as the ADK rate is valid only in the tunnel regime).

The optimal phase of THz generation is shown in Fig. 4.6 for the same simulations shown in Fig. 4.5. The drift towards lower ϕ_{rel} at high intensity is a result of depletion; if the RDC is calculated for an unchanging bound electron density, the phase remains relatively constant ($\approx .5\pi$, PCM) as intensity increases. The discrepancy between the optimal phase for the ab initio simulation and PCM/nonlocal models is explained as the result of the long-range scattering in [3]. Results therein are in general agreement for both PCM and *ab initio* simulations.

Figure 4.7 shows in a 1D of the PCM model the current $\mathbf{J}(t_f)$ dependence on ϕ_{rel} when the influence of the atomic potential is included (recollision). Here, 1D electron trajectories are calculated in the presence of $V_{atom}(\mathbf{x})$ and $\mathbf{E}(t)$, and weighted by the ADK ionization rate, to simulate the photocurrent model with the additional effect of rescattering from the parent ion. The initial condition of the electron bunches is taken to be $\mathbf{v}(t') = 0, \mathbf{x}(t') = x_{tunnel}$, the outside (exit) classical turning point through the potential barrier. The main observation is that the soft-core (long range) potential $V(\mathbf{x}) = -(x^2 + a^2)^{-1/2}$ shifts the phase of the peak generated current, quite substantially, while the gaussian nearly coincides with the collisionless case.

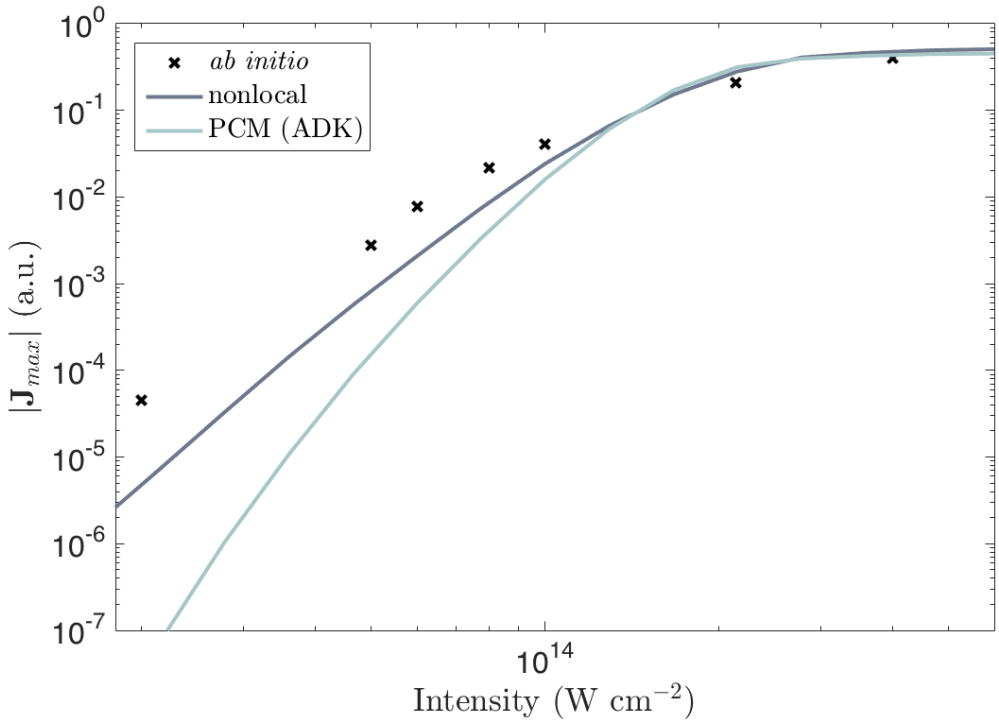

Figure 4.5: The maximal RDC yield ($\mathbf{J}(\phi_{rel})$) as a function of laser intensity and ϕ_{rel} (not pictured). Each black check represents the maximum current yield, for any value of ϕ_{rel}, at the given I_1 intensity. The discrepancies of the RDC yield at low intensity for the PCM model can be attributed to the tunnel-valid ADK rate; there is not a well justified rate model that can be employed for multiple colors in the multi-photon regime. All three models approximately agree at the highest intensity (5×10^{14} W cm^{-2}). Computational demands are significant in this regime, as the electron wavefunction excursion is large.

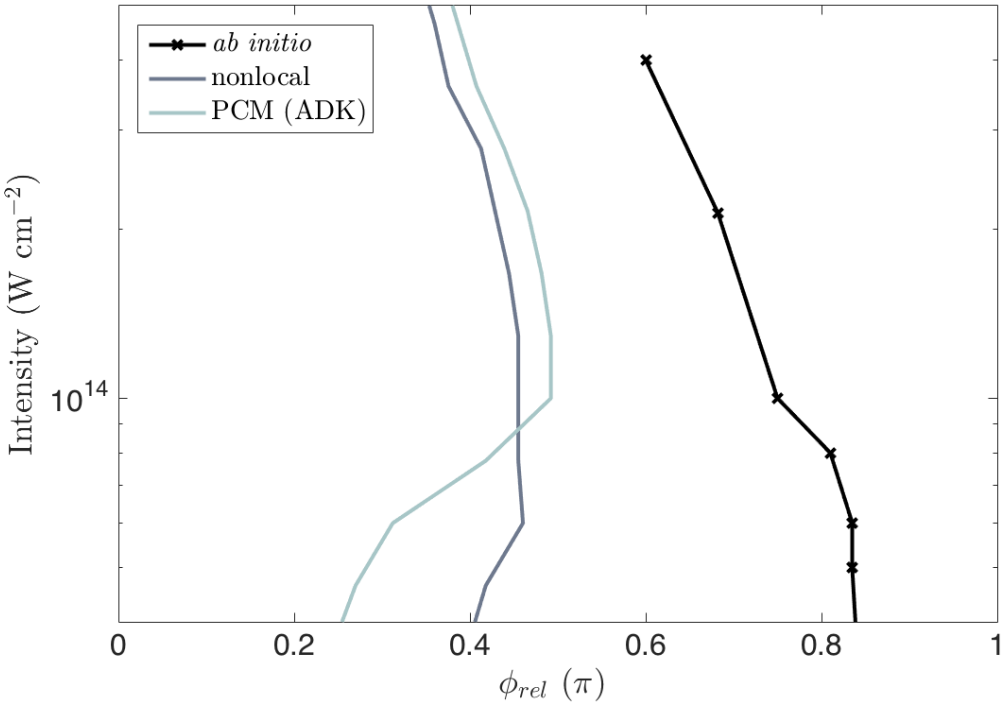

Figure 4.6: The optimal phase of THz generation for each model compared, as a function of first harmonic intensity. The (collisionless) PCM model and gaussian nonlocal model report nearly the same optimal phase above 10^{14} W cm^{-2}, between 0.35π and 0.4π (these values are slightly lower than the optimal phase in Fig. 4.3 due to the much shorter pulse length). The larger value for the optimal phase for the *ab initio* simulation is attributed to rescattering in the long-range potential.

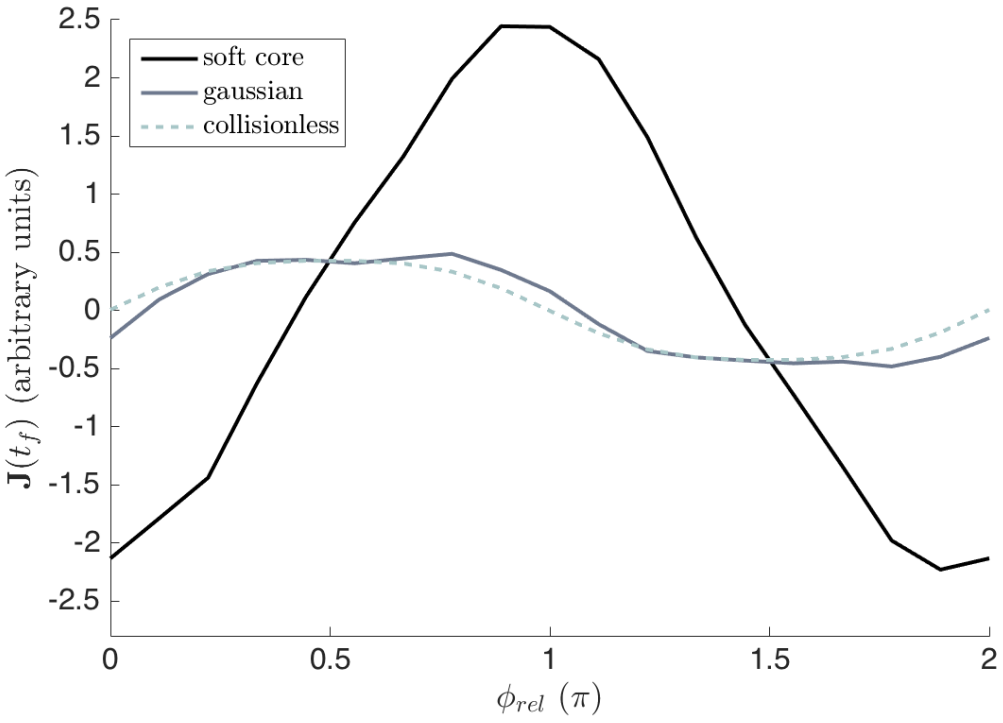

Figure 4.7: The RDC phase dependence for one-dimensionsal PCM simulations to examine the effect of Coulomb-like rescattering/recollision. The classical electron trajectories are calculated, in one-dimension, for electrons in the presence of soft-core (long-range) and gaussian (local, short-range) potentials, and compared with the collisionless PCM results, for $I_1 = 1 \times 10^{14}$ W cm^{-2}, 40 fs sine-squared pulse, $I_2/I_1 = 0.1$. It is observed that the soft-core ($V(x) = -(x^2+2)^{-1}$) potential induces a phase shift that peaks close to $\phi_{rel} = \pi$, rather than $\phi_{rel} = \pi/2$, and increases the RDC yield significantly, while the gaussian (short-range) potential has little effect. The increase in yield for the soft-core potential is partially explained by the reduced dimensionality, whereby ejected electrons must pass directly through the core. Both of these features are also confirmed in [3].

These simulations were carried out in 1D for simplicity; extending to three dimensions would require choosing the position and velocity initial conditions for a more complicated geometry (the turning point is now a locus of points), and the correspondence between the quantum tunneling process and classical birth trajectories is unclear.

The main observations are that the optimum phase of drift current for the long-range potential has been shift from $\phi_{rel} = \pi/2$ to nearly π, and the magnitude of the drift velocity has increased in magnitude compared with the collisionless case. In these simulations, the only difference is the post-ionization interaction with the potential, as the ADK ionization rate is used to weight the classical trajectories in each case. This supports the idea that scattering from the long-range potential is responsible for the trends seen comparing the TDSE, nonlocal and PC models in Figs. 4.6 and 4.5. To rule out the possibility that the reduced dimension was the dominant cause for the observations in Fig. 4.7, the nonlocal model was reformulated in 1D 4.4; the resulting phase dependence of optimal THz generation did not vary significantly from the 3D nonlocal results (not pictured). Experimental data (unpublished) reported by K.Y. Kim *et. al.* was found to be in good agreement with the collisionless and nonlocal model prediction for the optimal phase of THz generation, $\approx .5\pi$. Explanation for this result is currently under consideration.

Chapter 5: Extensions of the nonlocal gaussian potential

The previous chapters examined, in some detail, the response of an atom, modeled with a gaussian nonlocal potential in an external electric field. Effectively, the "strength" parameter V_0 can be adjusted to reproduce a desired bound state energy, while the "width" parameter σ can be used to tune the ionizability of the model atom; together these reproduce a Coulomb-like ionization rate over a wide range of laser frequencies and intensities.

There are a number of additional field-response phenomena that one might wish to accurately model with the nonlocal potential, such as the frequency dependent polarizability and hyper-polarizability, electron scattering dynamics, and high harmonic generation. While the nonlocal potential exhibits these features, it is unlikely to be in quantitative agreement with the Coulomb potential, as we have no free parameters left that may be explicitly fit for this purpose. There also remain a number of physical phenomena which the gaussian nonlocal potential is incapable of modeling; phenomena that rely explicitly on multiple bound states, or nonzero values of angular momentum. These include resonant excitation (Rabi-flopping), modification of ionization rate through excited state pathways, and additional resonances in the linear polarizability at frequencies corresponding to each eigenenergy

(*e.g.* Fig. 3.4, 3.5 in the single state case); such phenomena are strictly outside of the scope of what the single-term gaussian nonlocal potential examined in the previous chapters is capable of modeling.

To model additional phenomena, or quantitatively fit additional properties of the Coulomb potential, we need a more general and flexible framework for using nonlocal potentials. There is no unique approach, but if we wish to extend our model to include extra physics, it is worthwhile to give a closer examination of the nonlocal formulation in connection with potentials we might wish to model, *e.g.* the Coulomb potential. We examine the following in this chapter: 1. Exact representations of local potential with a series of nonlocal potentials. This method is satisfying from a theoretical perspective, as it does not require fitting numerical parameters, but may be difficult to implement in practice. Such systems often require a large (infinite) number of terms for exact equivalence, and truncation of these nonlocal terms will limit the quantitative agreement with *ab initio* approaches, and the number of nonlocal terms becomes increasingly impractical. 2. A heuristic model with gaussians and polynomials that reproduces a handful of eigenstates with similar properties to the hydrogen atom, and 3. A minimal change to the original gaussian formulation, increasing the number of fit parameters without increasing the complexity of the system.

5.1 Nonlocal formulation of local potentials

Until now, the justification given for using a nonlocal model potential has been that it satisfies basic quantum mechanical properties (it is self-adjoint, is linear in the wavefunction, and has a single eigenstate and continuum of free states), and a demonstration that it reproduces some results given by TDSE simulation and the PMPB ionization rate model; but we have offered no concrete connection between local potentials and the nonlocal model investigated. Briefly, we provide a firmer mathematical justification for the introduced model, and by showing a formal connection between local and nonlocal potentials provide some insight into some logical extensions.

A local potential in configuration space can be represented in momentum space as a convolution:

$$\mathscr{F}\{V(\mathbf{x})\psi(\mathbf{x},t)\} = \int d^3k' \phi(\mathbf{k}',t)\tilde{V}(\mathbf{k}-\mathbf{k}') \tag{5.1}$$

where $\phi(\mathbf{k},t)$ and $\tilde{V}(\mathbf{k})$ are the transformed wavefunction and potential. Provided a separable expansion can be found for the potential, $\tilde{V}(\mathbf{k}-\mathbf{k}') = \sum_j u_j^*(\mathbf{k})u_j(\mathbf{k}')$, the potential operator may be rewritten as a series of nonlocal potential terms:

$$\int d^3k' \phi(\mathbf{k}',t)\tilde{V}(\mathbf{k}-\mathbf{k}') = \sum_{j=1}^{N} u_j(\mathbf{k})S_j(t) \tag{5.2}$$

where $S_j(t) \equiv \int d^3\mathbf{k}' u^*(\mathbf{k}')\phi(\mathbf{k}',t)$. These potentials retain nonlocal form when untransformed and (re-)expressed in configuration space, noting that $\int d^3\mathbf{k}' u^*(\mathbf{k}')\phi(\mathbf{k}',t) = \int d^3\mathbf{x}' \tilde{u}^*(\mathbf{x}')\psi(\mathbf{x}',t)$ via Plancherel's Theorem.

This provides an exact representation of local potentials in terms of nonlocal potential terms in the Schrödinger equation. Such a series can be obtained, for example, for the gaussian local potential,

$$\mathscr{F}\{\exp\left(-\mathbf{x}^2/2\right)\psi(\mathbf{x},t)\} = \exp\left(-\mathbf{k}^2/2\right)\int d^3\mathbf{k}\ \exp\left(-\mathbf{k}'^2/2\right)\exp\left(\mathbf{k}\cdot\mathbf{k}'\right)\phi(\mathbf{k}',t),$$

where the factor $\exp(\mathbf{k}\cdot\mathbf{k}')$ must be decoupled to form a series of nonlocal terms. We may rewrite the dot product of the unit vector with spherical harmonics, $Y_\ell^m(\theta,\phi)$, as

$$\hat{\mathbf{k}}\cdot\hat{\mathbf{k}}' = \frac{4\pi}{3}\left(Y_1^0(\theta_k,\phi_k)Y_1^{0^*}(\theta_{k'},\phi_{k'}) + Y_1^{-1}(\theta_k,\phi_k)Y_1^{-1^*}(\theta_{k'},\phi_{k'}) + Y_1^1(\theta_k,\phi_k)Y_1^{1^*}(\theta_{k'},\phi_{k'})\right), \tag{5.3}$$

and Taylor expand the exponential factor

$$\exp(\mathbf{k}\cdot\mathbf{k}') = \sum_{n=0}^{\infty}\frac{\left(|\mathbf{k}||\mathbf{k}'|\hat{\mathbf{k}}\cdot\hat{\mathbf{k}}'\right)^n}{n!}. \tag{5.4}$$

This will produce a series of separable terms, the first several of which are listed here for $n = 0$, and $n = 1$ become:

$$u_1(\mathbf{k}) = c_1\exp(-\mathbf{k}^2/2), \tag{5.5}$$

$$u_2(\mathbf{k}) = c_2\exp(-\mathbf{k}^2/2)|\mathbf{k}|Y_1^{-1}(\theta_k,\phi_k), \tag{5.6}$$

$$u_3(\mathbf{k}) = c_3\exp(-\mathbf{k}^2/2)|\mathbf{k}|Y_1^{0}(\theta_k,\phi_k), \tag{5.7}$$

$$u_4(\mathbf{k}) = c_4\exp(-\mathbf{k}^2/2)|\mathbf{k}|Y_1^{1}(\theta_k,\phi_k). \tag{5.8}$$

It may be noted that the leading term, $u_1(\mathbf{k})$, corresponds to the gaussian nonlocal potential examined in the previous chapters of this thesis. Higher order terms will contain products of spherical harmonic terms, which may be simplified via

well known Clebsch-Gordon coefficients (or similar methods), so that all terms will appear in the form:

$$u(\mathbf{k}) = |\mathbf{k}|^n \exp(-\mathbf{k}^2/2) Y_\ell^m(\theta_k, \phi_k). \tag{5.9}$$

As a general comment, if the momentum and configuration space functions $u(\mathbf{x})$ and $u(\mathbf{k})$ only depend on the magnitude of the vector, they will share the same spherical harmonic dependence, $Y_\ell^m(\theta, \phi)$, $Y_\ell^m(\theta_k, \phi_k)$. This in turn determines the angular dependence of the eigenfunctions, $\psi_0(\mathbf{x})$ and $\phi_0(\mathbf{k})$. This may be seen as a consequence of the symmetry in the spherical harmonic representation of the Fourier transform, and orthogonality properties of the Y_ℓ^m:

$$\mathscr{F}\{u(\mathbf{k})\} = 4\pi \sum_{\ell,m} i^\ell \int d^3\mathbf{k} j_\ell(kx) Y_\ell^{m*}(\theta, \phi) Y_\ell^m(\theta_k, \phi_k) u(\mathbf{k}), \tag{5.10}$$

$$\int d\Omega \; Y_\ell^m(\theta_k, \phi_k) Y_{\ell'}^{m'*}(\theta_k, \phi_k) = \delta_{\ell\ell'}\delta_{mm'}. \tag{5.11}$$

This provides a theoretical connection between explicitly local and non-local potentials, although it is noted that exact representation often requires an infinite sum of nonlocal potentials. It is worth noting that not all (local) potentials are expressed with ease in the nonlocal formulation. This is important because, while the exact representations of local potentials are gauge invariant, as shown in chapter 3 (Eq.(3.5)), approximations (such as truncation of the infinite sum in Eq.(5.2)) will produce gauge-dependent systems. Efficient solution of systems with nonlocal potentials (using the Volterra integral formulation explored in previous chapters) relies on the kernel terms being integrable in either configuration or momentum space (Eqs.(3.14a), (3.14b), (3.15)), so that only the time dependence of $S(t)$ is

computed numerically; this is not a trivial requirement, and is not satisfied for many functions $u(\mathbf{k})$.

5.2 Solution of multi-term nonlocal potential systems

The previous section demonstrated that some local potential systems can be expanded into a series of nonlocal potential terms - this is generally true for systems that admit multiple eigenstates. We wish to use the same integral equation solution method as before, now adapted for a potential consisting of multiple terms in the form of Eq.(5.2).

A truncated expansion of a local potential, or otherwise chosen set of nonlocal potential functions $u(\mathbf{k})$ will support the eigenfunctions and eigenvalues $\{E_n, \phi_n(\mathbf{k})\}$ provided a set of S_k exist that satisfy the field free Schrödinger equation for each E_n:

$$\phi_n(\mathbf{k}) = \sum_k^N \frac{u_k(\mathbf{k}) S_k}{(E_n + \mathbf{k}^2/2)}, \tag{5.12}$$

$$S_k = \int d^3\mathbf{k}' \; u_k^*(\mathbf{k}')\phi_n(\mathbf{k}'). \tag{5.13}$$

The values S_k may be determined by projecting the expression for the eigenfunctions onto each $u_j^*(\mathbf{k})$:

$$S_j = \left(\sum_k^N \int d^3\mathbf{k} \frac{u_j^*(\mathbf{k}) u_k(\mathbf{k})}{(E_n + \mathbf{k}^2/2)} \right) S_k, \tag{5.14}$$

which can be more concisely written in matrix notation,

$$(\mathbb{1} - \mathbf{D}(E_n))\,\mathbf{S} = 0, \tag{5.15}$$

$$\mathbf{S} \equiv \begin{bmatrix} S_1 \\ \vdots \\ S_N \end{bmatrix} \tag{5.16}$$

where the elements $D_{jk}(E_n)$ are given by the integral j,k terms in Eq.(5.14). The values of each S_j, $j = 1, N$ associated each eigenenergy E_n correspond to the components of the eigenvectors $\mathbf{S}$, found through the determinant condition $|\mathbb{1} - \mathbf{D}(E_n)| = 0$. This condition Eq.(5.15) is not guaranteed to have a solution for a given set $\{u(\mathbf{k})\}$ and chosen values $\{E_n\}$, nor do a set of eigenvalues $\{E_n\}$ imply a unique set of $\{u(\mathbf{k})\}$. At most, there are as many eigenstates as separable potential terms ($n \leq N$).

Once an initial bound state ϕ_n is chosen, the system may be initialized to the corresponding eigenvector $\mathbf{S}$. The time evolution of the system can be calculated in a manner analogous to the single state system; here we examine the length-gauge formulation Schrödinger integral equation (based on superior results for predicting the ionization rate shown in chapter 3) with a multi-term potential:

$$\phi(\mathbf{k},t) = i\sum_{j=1}^{N}\int_{-\infty}^{t} dt' \exp\left[-\frac{i}{2}\int_{t'}^{t} dt'' \left(\mathbf{k} - \mathbf{A}(t) + \mathbf{A}(t'')\right)^2\right] u_j(\mathbf{k} - \mathbf{A}(t) + \mathbf{A}(t'))S_j(t'). \tag{5.17}$$

This expression for the wavefunction is projected on each $u_j(\mathbf{k})$ to yield coupled

Volterra-type integral equations for all $S(t)$:

$$S_j(t) = \sum_k^N \int_{-\infty}^{t} dt' K_{jk}(t,t') S_k(t'), \tag{5.18}$$

$$K_{jk} \equiv \int d^3\mathbf{k}\ \exp\left[-\frac{i}{2}\int_{t'}^{t} dt''\left(\mathbf{k}-\mathbf{A}(t)+\mathbf{A}(t'')\right)^2\right] u_j^*(\mathbf{k}) u_k(\mathbf{k}-\mathbf{A}(t)+\mathbf{A}(t')). \tag{5.19}$$

Efficient evaluation of $S_j(t)$ depends critically on obtaining closed form expressions of all K_{jk} after integrating over $d^3\mathbf{k}$; this, in turn, depends sensitively on the functional form of $u(\mathbf{k})$, and the gauge choice (the length gauge kernels are more complicated than those of the velocity gauge, and less likely to be k-integrable - compare Eqs.(3.14a), (3.14b)).

An example may clarify the discussion relating to multi-state systems at this point. We define a system composed of three nonlocal potential functions as follows:

$$u_1(\mathbf{k}) \equiv \mathscr{F}\left\{V_1 \exp\left(-\mathbf{x}^2/(2\sigma_1^2)\right)\right\} = V_1 \exp\left(-\sigma_1^2\mathbf{k}^2/2\right) \tag{5.20}$$

$$u_2(\mathbf{k}) \equiv \mathscr{F}\left\{V_2 z \exp\left(-\mathbf{x}^2/(2\sigma_2^2)\right)\right\} = V_2(ik_z)\exp(-\sigma_2^2\mathbf{k}^2/2) \tag{5.21}$$

$$u_3(\mathbf{k}) \equiv \mathscr{F}\left\{V_3|\mathbf{x}|^2 \exp\left(-\mathbf{x}^2/(2\sigma_3^2)\right)\right\} = V_3(3-\sigma_3^2\mathbf{k}^2)\exp(-\sigma_3^2\mathbf{k}^2/2) \tag{5.22}$$

where $\mathscr{F}\{\}$ denotes Fourier transform, as defined in Eq.(3.10). These functions were chosen to yield kernels for which the $d^3\mathbf{k}$-integral in Eq.(5.18) can be evaluated analytically while supporting wavefunctions with the same angular momentum dependence and eigen-energies $(0.5, 0.125, 0.125$ (a.u.), respectively) as the $1s, 2s, 2p$

hydrogen states. The field free wavefunctions in momentum space are:

$$\phi_1(\mathbf{k}) = (E_1 + \mathbf{k}^2/2)^{-1} \left(S_{11}u_1(\mathbf{k}) + S_{13}u_3(\mathbf{k})\right) \tag{5.23}$$

$$\phi_2(\mathbf{k}) = (E_2 + \mathbf{k}^2/2)^{-1} \left(S_{22}u_2(\mathbf{k})\right) \tag{5.24}$$

$$\phi_3(\mathbf{k}) = (E_3 + \mathbf{k}^2/2)^{-1} \left(S_{31}u_1(\mathbf{k}) + S_{33}u_3(\mathbf{k})\right) \tag{5.25}$$

where we have double subscripted the S coefficients as a reminder that they have different values for different eigenstates $\phi_j(\mathbf{k})$,

$$S_{jk} \equiv \int d^3\mathbf{k}\ u_k^*(\mathbf{k})\phi_j(\mathbf{k}). \tag{5.26}$$

These have integral representation in configuration space:

$$\psi_1(\mathbf{x}) = \frac{4\pi}{(2\pi)^{3/2}} \int_0^\infty dk k^2 \mathrm{sinc}(kr)\phi_1(\mathbf{k}) \tag{5.27}$$

$$\psi_2(\mathbf{x}) = \frac{4\pi}{(2\pi)^{3/2}}\ \partial_z \int_0^\infty dk k^2 \mathrm{sinc}(kr)\phi_2(\mathbf{k}) \tag{5.28}$$

$$\psi_3(\mathbf{x}) = \frac{4\pi}{(2\pi)^{3/2}} \int_0^\infty dk k^2 \mathrm{sinc}(kr)\phi_3(\mathbf{k}) \tag{5.29}$$

The wavefunctions depend on linear combinations of the $u(\mathbf{k})$, are normalized, and orthogonal.

For the chosen system, there are six adjustable parameters (V_i, σ_i; $i = 1, 2, 3$) and three conditions (the eigen-energies). The dispersion relation (Eq.(5.15)) only couples $u(\mathbf{k})$ belonging to the same angular momentum group (ℓ), as the $u_j(\mathbf{k}), u_k(\mathbf{k})$ belonging to different (orthogonal) ℓ groups will yield an integral of zero. Thus for the three state case, there exist two coupled equations for $E_1, E_3, \sigma_1, \sigma_3, V_1, V_3$ (belonging to the $\ell = 0$ group) and one equation that relates parameters E_2, σ_2, V_2 (belonging to the $\ell = 1$ group). The parameters in the three state system may be tuned to produce orbitals similar to that of hydrogen, shown in Fig.5.1.

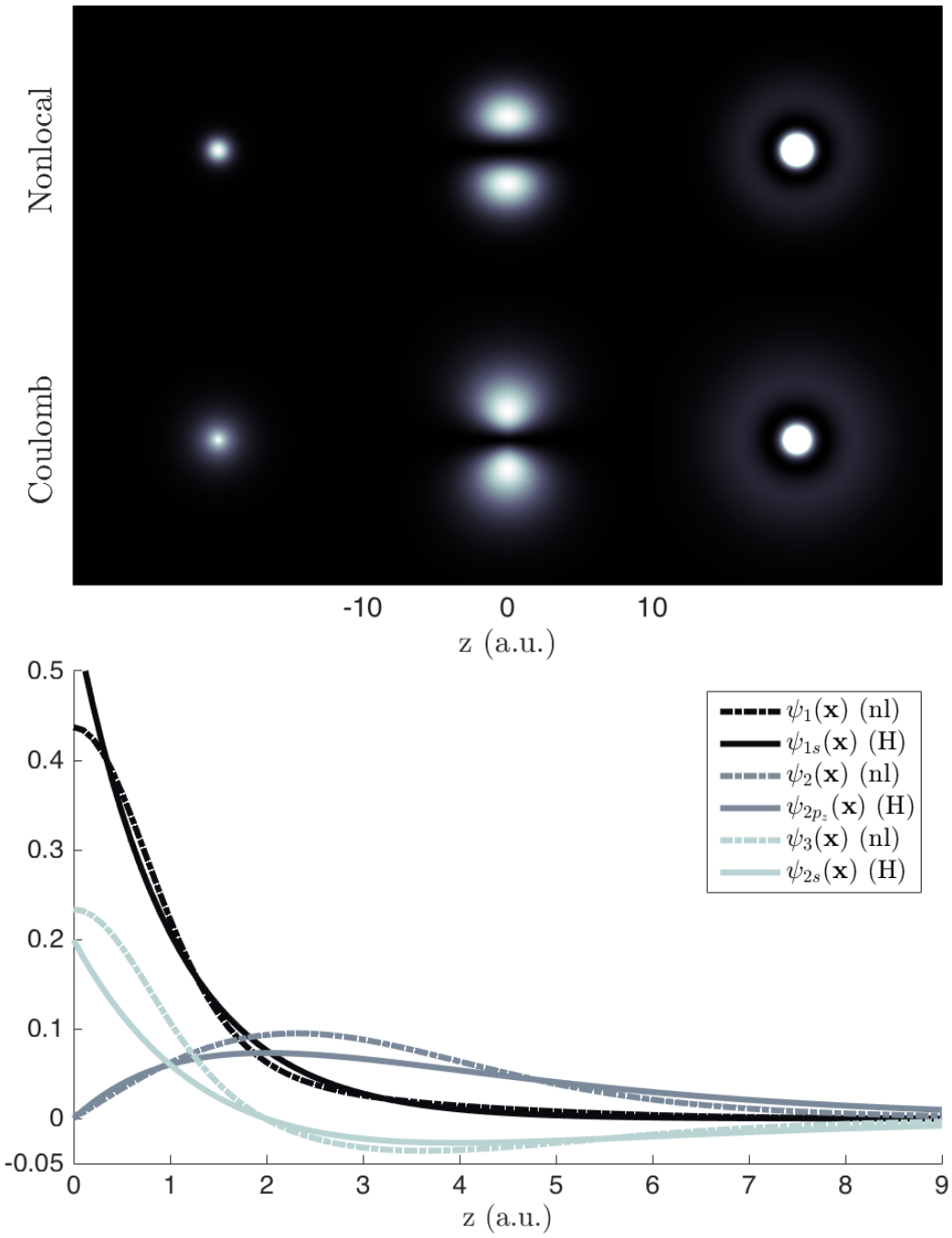

Figure 5.1: Wavefunction ($|\psi(x, y = 0, z)|^2$) comparison of the hydrogen $1s, 2p_z, 2s$ orbitals with the multi-state nonlocal model analogues. A comparison of the radial dependence (along the z-axis) of the eigenstates is shown in the lower plot.

The time evolution of this system is determined by numerically solving Eq.(5.18) for the coupled, complex $S_j(t)$. The probability for the electron to be found in any given state is usually given by projecting onto the eigenfunctions of the field-free system, $\rho_n(t) = |c_n(t)|^2$, where $c_n(t) \equiv \int d^3\mathbf{k}\phi_n^*(\mathbf{k})\phi(\mathbf{k},t)$. For convenience, we approximate the bound state population using the eigenvectors of $\mathbf{S}_0(E_n)$; here the time-dependent vector $\mathbf{S}(t)$ is projected onto these (orthogonal) vectors, and determine the coefficients, $a_n(t)$:

$$\mathbf{S}(t) \approx a_1(t)\mathbf{S}_0(E_2) + a_2(t)\mathbf{S}_0(E_2) + a_3(t)\mathbf{S}_0(E_3). \tag{5.30}$$

The time-dependent probability of each bound state is (approximately) given by $\rho_n(t) = |a_n(t)|^2$; this is the N-state extension of the bound probability measure given in Eq.(3.40). As was true for the single state case, this equation is not an exact equality due to the (often negligible) overlap of scattering states with the functions $u_j(\mathbf{k})$ - that is to say that, $\mathbf{S}(t)$ is only approximately spanned by the eigenvectors S_0.

This system also exhibits additional physical phenomena, such as an additional resonance in the frequency dependence of the linear response ($\omega_0 = 0.125$(a.u.), see Fig. 3.4), and resonant excitation (Rabi-flopping) in the presence of an electric field at the difference frequency $\omega = 0.5 - 0.125$ (Fig. 5.2).

Although this extended nonlocal model includes additional physics, these new features come at a cost of increasing complexity. The set of parameters $\{V, \sigma\}$ that produce the desired response of the model atom may be multi-valued or may not exist at all. Fitting specific phenomena to be Coulomb-like is a time consuming pro-

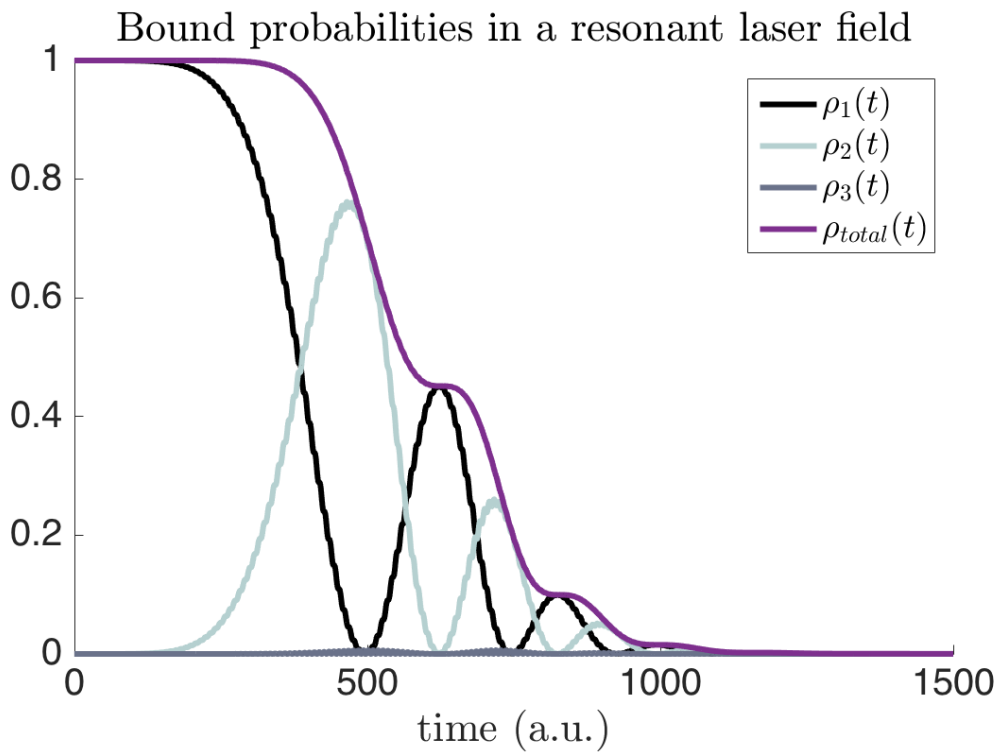

Figure 5.2: The three state system (definitions of $u(\mathbf{k})$ given by Eqs. (5.20)) subject to a laser field at the resonant frequency, $\omega_{laser} = E_1 - E_2 = .375$ (a.u.). The bound probability for each eigenstate, $\rho_n(t)$ (Eq.(5.30)), and the total bound probability $\rho_{total}(t)$, are plotted as a function of time. The wavefunction, initially in the ground state, can be observed to alternate populating states $\phi_1(\mathbf{k})$ (blue) and $\phi_2(\mathbf{k})$ (red), while the total bound probability (purple) decreases due to partial transition to continuum states (ionization). The total population decreases significantly only when the excited state (red) is populated - this is an example of an excited state ionization pathway not observed in the single state model. The field term in the Hamiltonian, $\langle\phi_j(\mathbf{k})|(i\partial_t\mathbf{A}(t)\cdot\nabla_k)|\phi_k(\mathbf{k})\rangle$ is observed to allow transitions for bound states $j,k = 1,2$ but is zero for $j,k = 1,3$; although the laser is resonant for $\omega_{laser} = E_1 - E_3$, transition from the ground state to $\phi_3(\mathbf{k})$. The parameters here are not fit for hydrogen.

cess, as the parameter space grows linearly with each additional $u(\mathbf{k})$, and quickly becomes impractical to specify by inspecting simulation results. Fitting parameters by inspection is also likely to introduce unwanted artifacts in the system as well, which may be difficult to distinguish from actual physical phenomena without validating against *ab initio* simulation.

For this reason, it is preferable to either: 1. obtain a nonlocal representation more directly derived from the Coulomb potential, thereby reducing or eliminating the fitting parameters of the system, or 2. clarify and restrict the scope of phenomena one wishes to model, and create a straightforward extension that is capable of reproducing such effects without introducing unnecessary complication.

5.3 Direct treatment of the Coulomb potential

It would be preferable to directly expand the Coulomb potential (expressed as a Yukawa potential here to perform the Fourier transform),

$$\lim_{m\to 0} \mathscr{F}\left\{\frac{e^{-m|\mathbf{r}|}}{|\mathbf{r}|}\psi(\mathbf{x},t)\right\} = \int d^3\mathbf{k}'\phi(\mathbf{k}',t)\frac{1}{|\mathbf{k}-\mathbf{k}'|^2} \tag{5.31}$$

into a series of nonlocal potentials, in the form of Eq.(5.2), but the (transformed) Coulomb potential is not as easily separated as the local gaussian or sinusoidal potentials. Reduced models have been explored by Nganso *et. al* [37–39] that reproduce N Coulomb eigenstates (and associated eigenenergies) exactly, using N nonlocal potential terms. Their approach was to solve for the functions $u_j(\mathbf{k})$ that

satisfy the condition:

$$(E_n + \mathbf{k}^2/2)\phi_n(\mathbf{k}) = \sum_j^N u_j(\mathbf{k}) S_{nj}(t), \tag{5.32}$$

where E_n and $\phi_n(\mathbf{k})$ are hydrogen eigenenergies and momentum space representation of the hydrogen eigenfunctions to be included, respectively, where S_{nj} represents the overlap of $\phi_n(\mathbf{k})$ and $u_j(\mathbf{k})$. The first few are listed here, corresponding to the transform of the configuration space orbitals, $\mathscr{F}\{\psi_{nlm}(\mathbf{x})\}$:

$$\phi_{100}(\mathbf{k}) = \frac{2^{3/2}}{\pi} \frac{1}{(1+\mathbf{k}^2)^2} \tag{5.33}$$

$$\phi_{200}(\mathbf{k}) = \frac{16}{\pi} \frac{1-4\mathbf{k}^2}{(1+4\mathbf{k}^2)^3}. \tag{5.34}$$

They note that the coefficients S_{nj} that satisfy the above condition are not unique; all eigenfunctions belonging to the same angular momentum group will form families of solutions that have ℓ free parameters that must be specified. That is, the eigenenergies and eigenfunctions alone are not enough to specify the form of all $u(\mathbf{k})$.

The k-dependence is integrated out of the kernels $\mathbf{K}_{jk}$ for this system, but are rather complex, and the system was solved in the velocity gauge. It is unknown (to this author) whether a closed form expression for the kernel terms (5.19) exist in the length gauge for the transformed momentum eigenstates (*e.g.* Eqs.(5.33) and (5.34)); this is of some importance as it was demonstrated in Ch. 3 that the length gauge formulation gives better agreement in the multiphoton and tunnel ionization rates.

Although this method appears to be more systematic than the phenomenological approach, and may ultimately capture more physical phenomena as additional

$u(\mathbf{k})$ are included, it becomes increasing computationally costly and, unless a great number of $u(\mathbf{k})$ are included, will not accurately characterize the ionization rate or polarizability of a desired atom as well as a well-tuned heuristic model.

5.4 Extended gaussian model

In contrast to the above methods, we can create a simple atomic model similar to the gaussian nonlocal model explored in chapters 1-3 that has additional parameters for tuning a wider range of atomic properties. We do this by letting the definition of $u(\mathbf{k})$ contain multiple gaussian terms:

$$u(\mathbf{k}) = \sum_j c_j \exp(-\sigma_j^2 \mathbf{k}^2/2), \tag{5.35}$$

leaving the definition of $S(t)$ unchanged:

$$S(t) \equiv \int d^3\mathbf{k}' u(\mathbf{k}')\phi(\mathbf{k}', t) \tag{5.36}$$

This system admits a single bound state, but adds two additional tuning parameters (c_j and σ_j) for each additional gaussian term. The kernel terms for evaluating $S(t)$ and the dipole moment are slightly modified versions of Eqs.(3.21), (3.25), and

(3.26):

$$K_{jk}(t,t') = ic_j^* c_k \left(\frac{2\pi}{\alpha_{jk}}\right)^{3/2} \ldots \tag{5.37}$$
$$\exp\left[-\frac{\sigma_j^2\mathbf{A}^2(t) + \sigma_k^2\mathbf{A}^2(t') - \alpha_{jk}^{-1}\left(i\Delta\mathbf{x} + \sigma_j^2\mathbf{A}(t) + \sigma_k^2\mathbf{A}(t')\right)^2}{2}\right]$$

$$\mathbf{L}_{jk}(t,t') = \sigma_j^2\Big(\mathbf{n}_{jk}(t,t') - \mathbf{A}(t)\Big)K_{jk}(t,t') \tag{5.38}$$

$$\mathbf{M}_{jk}(t,t') = -\Big(\mathbf{n}_{jk}(t,t') - \mathbf{A}(t)\Big)K_{jk}(t,t') \tag{5.39}$$

$$\mathbf{n}_{jk}(t,t') = \frac{i\Delta\mathbf{x}(t,t') + \Big(\sigma_j^2\mathbf{A}(t) + \sigma_k^2\mathbf{A}(t')\Big)}{\alpha_{jk}(t,t')} \tag{5.40}$$

$$\alpha_{jk} = \big(\sigma_j^2 + \sigma_k^2 + i(t-t')\big) \tag{5.41}$$

$$\Delta\mathbf{x}(t,t') \equiv \int_{t'}^{t} dt''\mathbf{A}(t'') \tag{5.42}$$

where the full terms $K(t,t'), \mathbf{L}(t,t'), \mathbf{M}(t,t')$ that appear in the integral equation for $S(t)$ and expressions for the polarization (Eqs. (3.20), (3.27), and (3.28)) are summed over indices j,k, for all values of c,σ.

We examine the simplest extension, that of two gaussian terms ("double gaussian") in the definition of $u(\mathbf{k})$. A two gaussian potential system has four free parameters and one constraint (a specified eigenenergy); the remaining free parameters may be specified as $c_2/c_1, \sigma_1, \sigma_2$. The two additional parameters allow us to fit, in addition to the ionization rate, the low frequency limit linear polarizability for hydrogen. The solution is not unique in the parameters choice. Figures 5.3, 5.4, and 5.5 depict the dependence of the ionization rate and linear polarizability as a function of the parameter space $\{c_j, \sigma_j\}$.

For a double gaussian potential subject to a short ($\sim$ 10 fs) ionizing electric field at 2×10^{14} W cm^{-2}, the static polarizability ($\alpha(0)$) and final bound electron

probability are plotted as a function of the parameters σ_1, σ_2 for various values of c_2/c_1. The solid black lines are curves of constant (desired) values of the linear polarizability ($\alpha(0) = 4.5$) and the bound probability calibrated with the PMPB ionization model corresponding to that of hydrogen. For the case $c_2/c_1 = .01$ we (nearly) recover the values obtained by the original single state system, and observe that the linear polarizability is approximately $18a_0^{-3}$; there is no simultaneous solution of the ionization rate and value for $\alpha(0)$ that we desire. Solutions are obtained as the value of c_2/c_1 is increased, given by the crossing points (see Figs. 5.4 and 5.5) of the solid black lines. The double gaussian potential characterizes the ionization rate well over a range of laser frequencies and intensities (not shown).

The emitted photon spectrum is also affected by the addition of a gaussian potential term. The radiation spectrum from the accelerated electron wavefunction can be approximated with the frequency dependent Larmor formula in atomic units:

$$E_{THz} = \int_0^{\omega_{max}} \frac{\partial E(\omega)}{\partial \omega} d\omega, \quad \frac{\partial E(\omega)}{\partial \omega} \propto \left| \mathscr{F} \left\{ \frac{d^2 \langle \mathbf{p}(t) \rangle}{dt^2} \right\} \right|^2 \tag{5.43}$$

The existence of high frequency radiation observed here can be discussed in the framework of high harmonic generation (HHG), that suggests energetic photons are created due to continued recollision of the electron (wavefunction) with the atomic potential as it oscillates with the laser field.

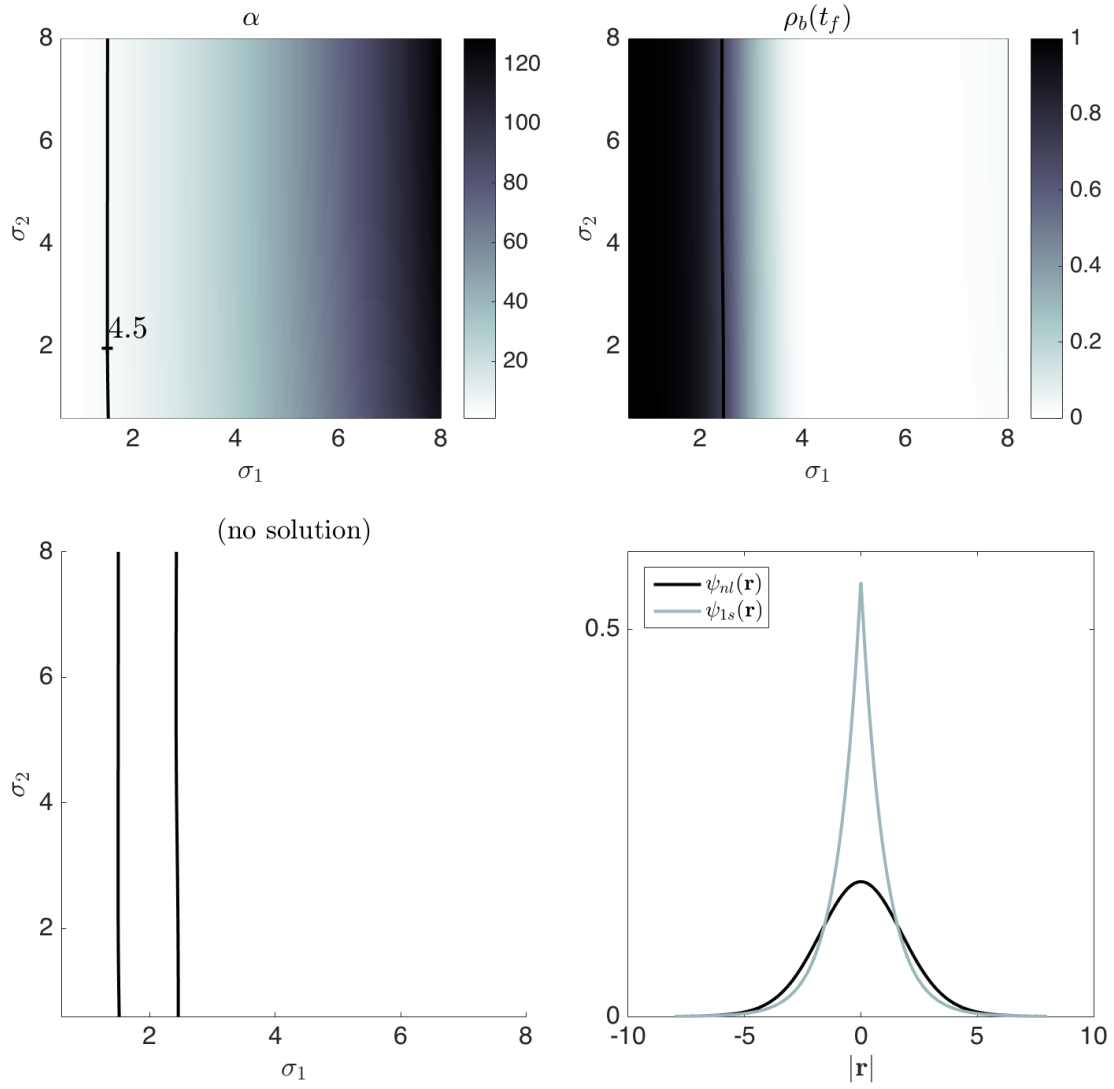

Figure 5.3: (Color online) The linear polarizability α as a function of tuning parameters σ_1, σ_2, for $c_2/c_1 = 0.01$. Here, $u_2(\mathbf{k}) \approx 0$, nearly degenerate with the single potential case. There is therefore little dependence in the ionization rate or linear polarizability on the value of σ_2, and no solution set that satisfies the ionization rate and linear polarizability. The wavefunction is plotted against the ground state of hydrogen for comparison, but matching the profile of the $1s$ state is not the aim.

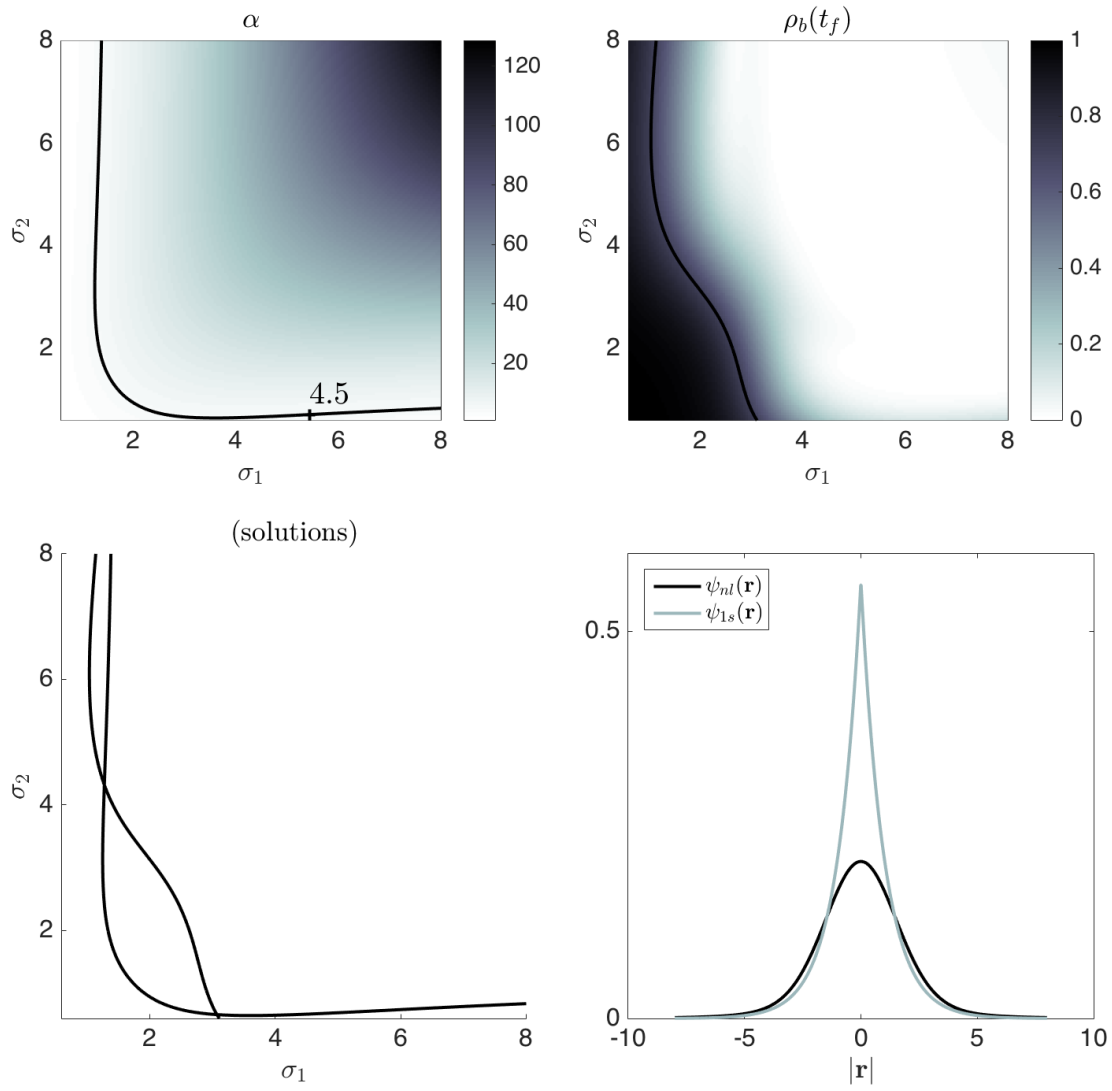

Figure 5.4: (Color online) The $c_2/c_1 = .5$, is close to the minimum for which solutions are observed for which the linear polarizability and ionization rate are matched. There exist two solutions in this case at $\sigma_{1,2} = \{1.28, 4.3\}$, and $\sigma_{1,2} = \{3.07, 0.6\}$.

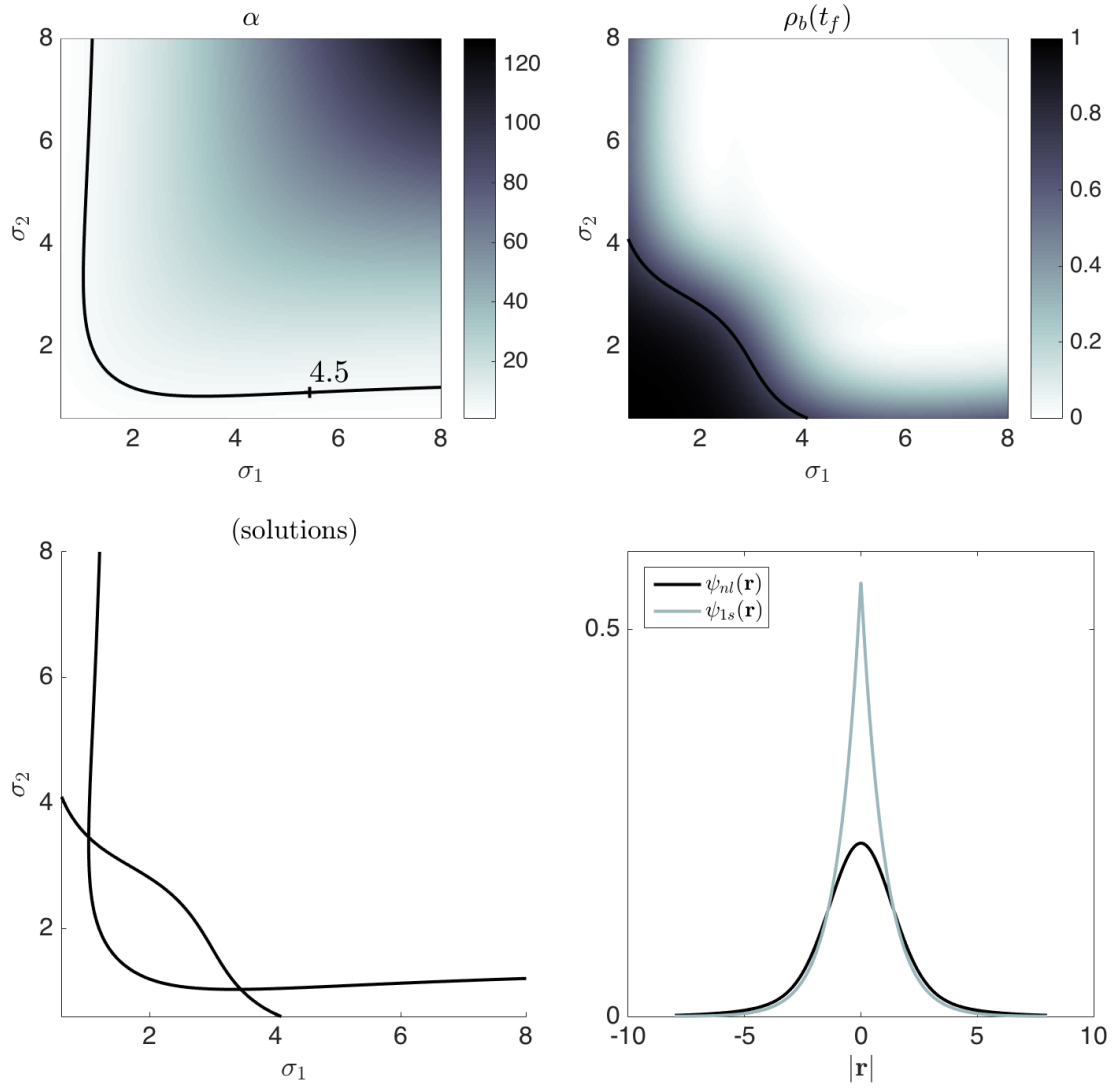

Figure 5.5: (Color online) The solution for $c_2/c_1 = 1$, $\sigma_{1,2} = \{1.097, 3.43\}$, the solution used for the data in Figs. 5.6 and 5.7.

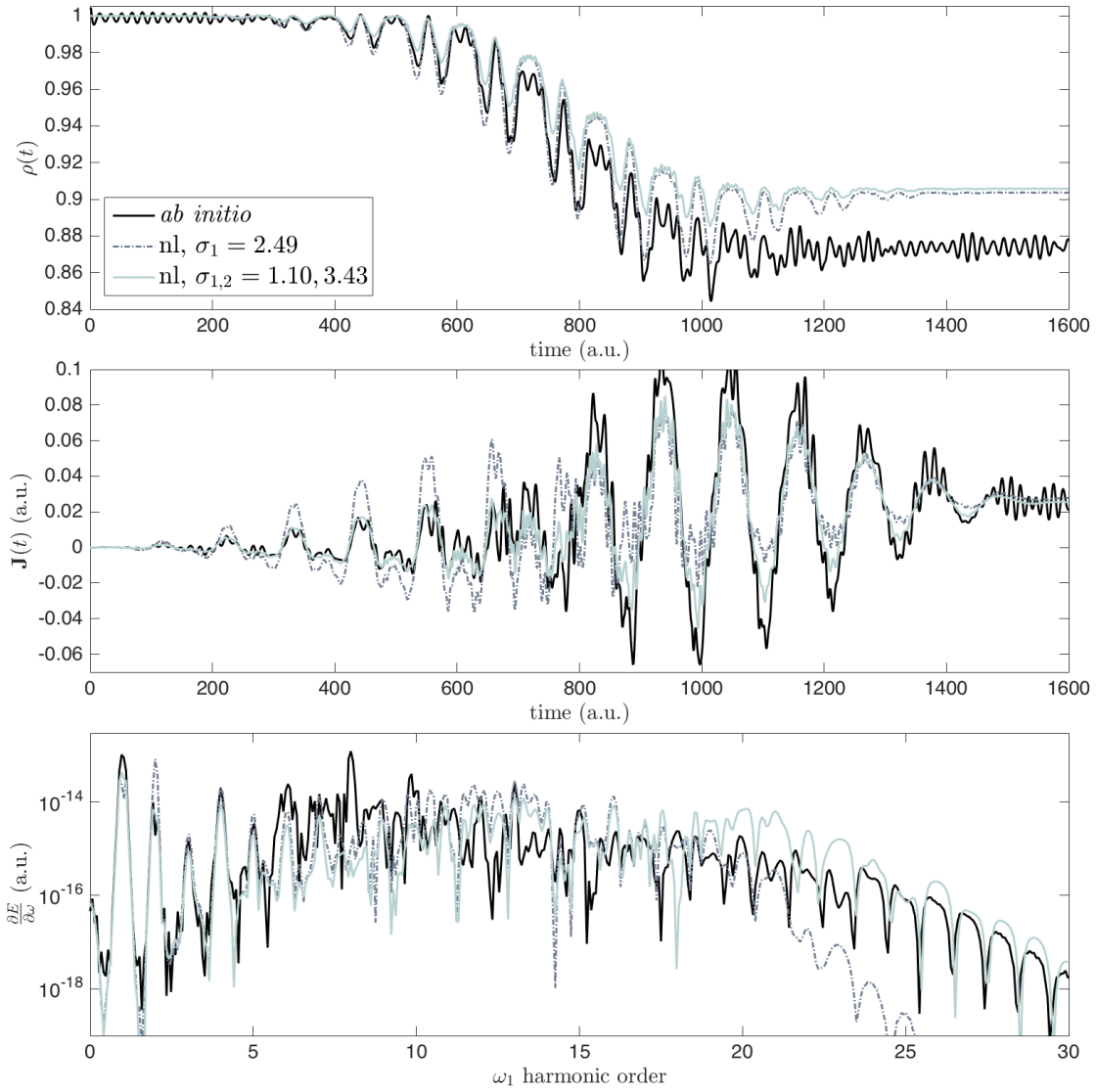

Figure 5.6: Two-color simulation is revisited with the double gaussian model. The field in this case was a 15fs 800 nm pulse at 1×10^{14} W cm^{-2} with a second harmonic at 10 intensity second harmonic, with relative phase $\pi/2$, compared with *ab initio* (softcore) TDSE simulation. The double gaussian model (blue) demonstrates improved polarization current, compared with the *ab initio* results (black) for $t < 700$(au). The frequency content for large harmonic order is also improved with the addition of another gaussian nonlocal potential term.

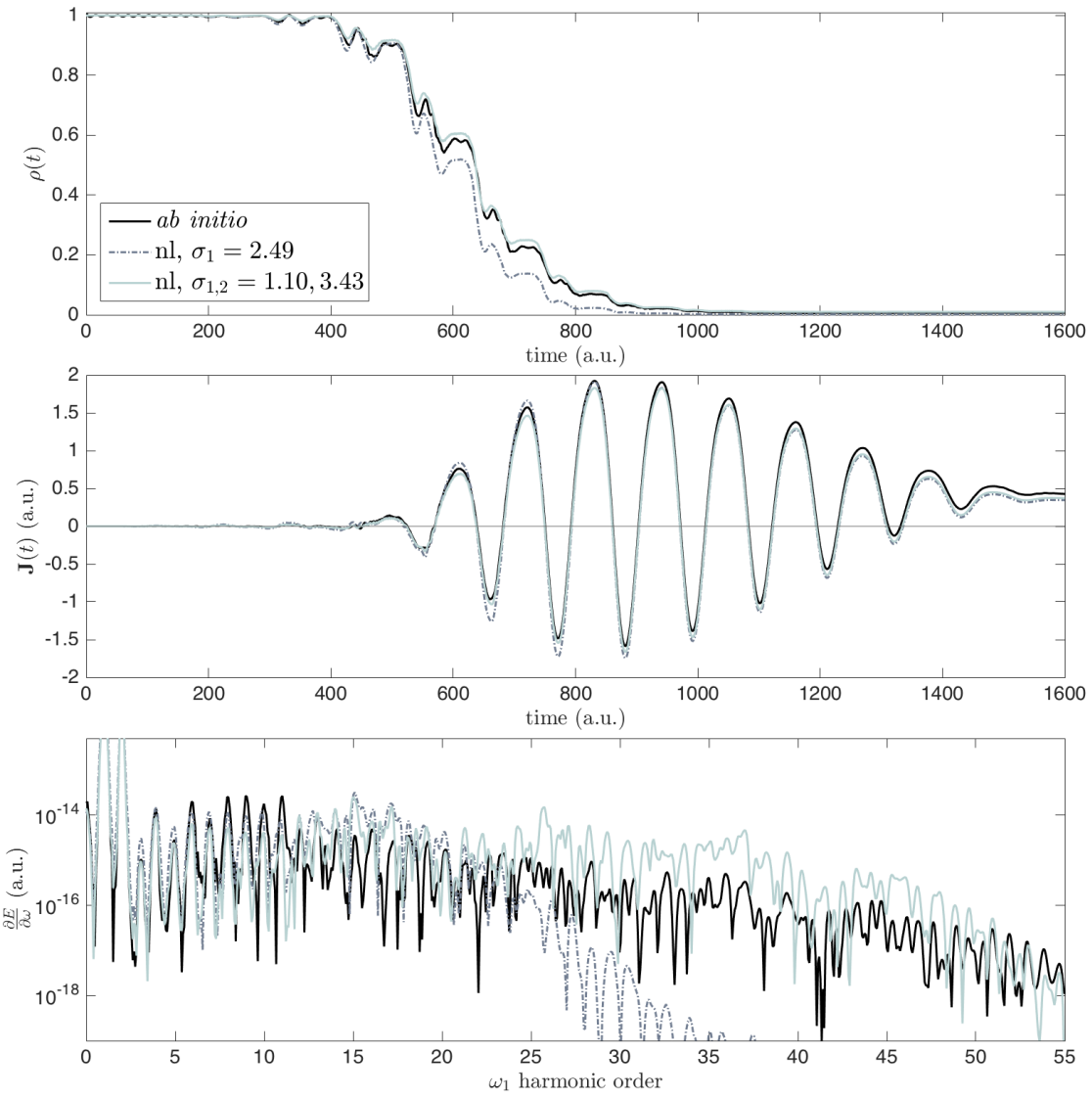

Figure 5.7: For the same pulse profile at 4×10^{14} W cm^{-2}, the double gaussian model shows improved ionization agreement with the *ab initio* result (although the reason for this is unclear). The current (second pane) is almost completely dominated by the plasma response, and all three models show good agreement. As intensity increases, the double gaussian model gives better agreement in the photoelectron spectrum at high harmonics (the single gaussian model drops off at around n = 30).

Chapter 6: Numerical implementation

In this chapter, we consider a numerical treatment of the single term and extended multi-term systems with an emphasis on expedient calculation. The main objective is to find a solution for the time dependence of $S(t)$, or set of $S_j(t)$ (Eq. (5.18)) in a multi-state formulation, from which the wavefunction $\psi(\mathbf{x},t)$ or $\phi(\mathbf{k},t)$, polarization $\mathbf{p}(t)$, and ionization rate $\nu(t)$ may be reconstructed.

We presently examine the kernel term $K(t,t')$ associated with gaussian non-local terms,

$$u_j(\mathbf{k}) \equiv c_j \exp(-\sigma_j^2 \mathbf{k}^2/2), \tag{6.1}$$

$$u_k(\mathbf{k}) \equiv c_k \exp(-\sigma_k^2 \mathbf{k}^2/2). \tag{6.2}$$

This corresponds to the kernel term $K_{jk}(t,t')$ for the multi-gaussian extension (chapter 5), and reduces to the kernel term of the single potential system characterized in chapters 2-4, where $V_0 \propto c_j^* c_k$, and $\sigma_j = \sigma_k$. In these cases, there is a single unknown $S(t)$ which we wish to evaluate via the length gauge integral equation of form:

$$S(t) = \sum_{j,k} \int_{-\infty}^{t} dt' K_{jk}(t,t') S(t') \tag{6.3}$$

where

$$K_{jk}(t,t') = ic_j^* c_k \left(\frac{2\pi}{\alpha_{jk}(t,t')}\right)^{3/2} \dots \tag{6.4}$$
$$\exp\left[-\frac{\left(\sigma_j \mathbf{A}(t)\right)^2 + \left(\sigma_k \mathbf{A}(t')\right)^2 - \alpha_{jk}(t,t')^{-1}\left(i\Delta\mathbf{x}(t,t') + \left(\sigma_j^2 \mathbf{A}(t) + \sigma_k^2 \mathbf{A}(t')\right)\right)^2}{2}\right],$$

where $\alpha_{jk}(t,t') = \sigma_j^2 + \sigma_k^2 + i(t-t')$ and $\Delta\mathbf{x}(t,t') \equiv \int_{t'}^{t} dt'' \mathbf{A}(t'')$. For rapid numerical evaluation, we may employ a trapezoidal integration scheme of fixed step size Δt, where $n\Delta t \equiv t$, and $j\Delta t \equiv t'$:

$$S(n\Delta t) = \Delta t \sum_{j=-\infty}^{(n-1)\Delta t} K_{jk}(n\Delta t, j\Delta t) S(j\Delta t) - \frac{\Delta t}{2} K_{jk}(n\Delta t, n\Delta t) S(n\Delta t), \tag{6.5}$$

that may be employed to solve for the unknown endpoint value $S(n\Delta t)$. This requires $\sim \mathcal{O}(n^2)$ evaluations (owing evaluation over all t' at each time t) with error of order $\mathcal{O}(\Delta t^3)$ convergence to the continuous time solution. There are two main issues that must be addressed when implementing this scheme: 1. as written, we must evaluate an infinite number of grid points in the past, and 2. the system parameters $E_0, c_j, c_k, \sigma_j\sigma_k$, that satisfy the field-free eigenfunction solution for the continuous system are only approximately correct for the finite Δt system. If these parameters are not adjusted to account for discretized time, the field free ($\mathbf{A}(t) = 0$) solution is not an exact eigenstate, and the magnitude of $S(t)$ is observed to "damp" exponentially. In this case, the potential appears "leaky" , and for numerical simulation with a laser field present, the decrease in $|S(t)|$ is impossible to distinguish from field induced ionization. We examine methods for mitigating these issues presently.

6.1 Eigenvalue dispersion relation for finite Δt system

We may evaluate the continuous time integral in Eq.(6.3) at $t = 0$, and move all terms to the left hand side of the equation to define a dispersion function:

$$D(E_0, c_j, c_k, \sigma_j, \sigma_k) = S(0) - \int_{-\infty}^{0} K(0, t')S(t')dt' = 0. \tag{6.6}$$

Assuming the wavefunction is initialized in the ground state of form $\phi_0(\mathbf{k})e^{iE_0 t}$, the solution to $S(t)$ is given by $S(t) = S_0 e^{iE_0 t}$, and a closed form solution to the integral may be found that relates the parameters $c_j, c_k, \sigma_j, \sigma_k$, to the chosen eigenvalue E_0, given by

$$D = 1 - 2^{5/2}\pi^{3/2}c_j^* c_k \left(\left(\sigma_j^2 + \sigma_k^2\right)^{-1/2} - (\pi E_0)^{1/2} e^{(\sigma_j^2+\sigma_k^2)E_0} \text{erfc}\left[(\sigma_j^2 + \sigma_k^2)^{1/2} E_0^{1/2}\right] \right). \tag{6.7}$$

This relationship is exact for the continuous system, but only approximately true for the finite time-step system, resulting in numerical damping in the magnitude of $S(t)$. Smaller step size Δt can reduce this effect, but becomes costly to evaluate.

We seek instead a modified dispersion relation for the eigensystem that additionally depends on the time-step: $D(E_0, c_j, c_k, \sigma_j, \sigma_k \Delta t) = 0$. We obtain such a result by writing the finite time-step approximation of the continuous system, evaluated at $n\Delta t = 0$ via trapezoidal integral approximation:

$$D(E_0, \{c, \sigma\}, \Delta t) = 1 - \Delta t \sum_{j=-\infty}^{0} K(0, j\Delta t)e^{iE_0 j\Delta t} + \frac{\Delta t}{2}K(0, 0), \tag{6.8}$$

$$D(E_0, \{c, \sigma\}, \Delta t) = 0.$$

We wish to find a method for rapidly evaluating this sum, which converges slowly due to the oscillatory exponential and slowly varying envelope of $\alpha_{jk}(t, t')$; the following

algebraic steps are a method to rewrite the sum in a series of closed form expressions that depend on powers of Δt. The summed terms in Eq.(6.26) may be written in a general form:

$$A\Delta t \sum_{j=-\infty}^{0} \frac{e^{iE_0 j\Delta t}}{[B - ij\Delta t]^{m/2}} \tag{6.9}$$

where A, B may be treated as constants, and $m = 3$ in this case. We express the denominator as the result of an m-dimensional gaussian integral over the introduced dummy variable $\mathbf{q}$ for reasons that will be clear in a moment:

$$A\Delta t \sum_{j=-\infty}^{0} e^{iE_0 j\Delta t} \left[\pi^{-m/2} \int d^m\mathbf{q}\ e^{-(B-ij\Delta t)\mathbf{q}^2}\right]. \tag{6.10}$$

Interchanging the order of summation/integration, we may write the sum as an infinite geometric series over j. Using a well known geometric series identity, we obtain

$$A\Delta t \left[\pi^{-m/2} \int d^m\mathbf{q}\ e^{-B\mathbf{q}^2} \frac{1}{1 - e^{-i(E_0+\mathbf{q}^2)\Delta t}}\right]. \tag{6.11}$$

Noting that the integral only depends on $|\mathbf{q}|^2$, the generalized m-dimensional "angular" and "radial" contributions may be separated

$$\int d^m\mathbf{q} = \int d\Omega_m \int dq, \tag{6.12}$$

where the angular integral is given by solid angle subtended by an m-sphere,

$$\int d\Omega_m = 2\frac{\pi^{m/2}}{\Gamma(\frac{m}{2})}, \tag{6.13}$$

leaving only the (1D) "radial" integral to be computed:

$$A\Delta t \left[\frac{2}{\Gamma(\frac{m}{2})} \int_0^\infty dq\ e^{-Bq^2} \frac{1}{1 - e^{-i(E_0+q^2)\Delta t}}\right]. \tag{6.14}$$

At this point, the exponential function in the denominator can be Taylor expanded for small Δt to give an integrable series:

$$\frac{2A\Delta t}{\Gamma(\frac{m}{2})}\int_0^\infty dq e^{-Bq^2}\left(\frac{-i}{(E_0+q^2)\Delta t}+\frac{1}{2}+\frac{i(E_0+q^2)}{12}\Delta t+\mathcal{O}(\Delta t^3)\ldots\right). \tag{6.15}$$

For the gaussian kernel term, the discrete time-step dispersion condition becomes:

$$D(E_0,c_j,c_k,\sigma_j,\sigma_k)=D_0(\Delta t^0)+D_1(\Delta t^1)+D_2(\Delta t^2)+D_3(\Delta t^3)+...=0, \tag{6.16}$$

where

$$D_0=1-2^{5/2}\pi^{3/2}c_j^*c_k\left(\left(\sigma_j^2+\sigma_k^2\right)^{-1/2}-(\pi E_0)^{1/2}e^{(\sigma_j^2+\sigma_k^2)E_0}\mathrm{erfc}\left[(\sigma_j^2+\sigma_k^2)^{1/2}E_0^{1/2}\right]\right) \tag{6.17}$$

$$D_1=0 \tag{6.18}$$

$$D_2=-\pi^{3/2}c_j^*c_k\Delta t^2\frac{3+2E_0(\sigma_j^2+\sigma_k^2)}{6\sqrt{2}(\sigma_j^2+\sigma_k^2)^{5/2}} \tag{6.19}$$

$$D_3=0. \tag{6.20}$$

where each term is linear in $c_j^*c_k$ and increasing in powers of Δt. The leading order term, D_0, is independent of Δt, recovering the result from the continuous-time dispersion relation. The term D_1 cancels with the endpoint term $\frac{\Delta t}{2}K(0,0)$ in Eq.(6.26), and all higher order terms D_n are nonzero only for even powers of Δt^n.

In the case of the single potential system, this equation may be easily inverted to solve for a Δt dependent value of $c_j^*c_k$ (V_0), giving far better approximation of the finite time-step parameters that satisfy the time-independent eigenvalue equation, and, to the extent that numerical correction terms are kept, the numerical error in the magnitude of $S(t)$ is significantly reduced without resorting to smaller values of Δt.

This error correction is critical in reducing computation time to achieve a minimal error in the numerically induced ionization rate - especially critical at low intensities, $\sim 1 \times 10^{13}$ W cm^{-2} at optical wavelengths. The numerical corrections for V_0 were carried out to eighth order for the work that appears in this thesis, that for reasonable values of Δt reduce the field-free error in $|S(t)|$ comparable with that of floating point error.

6.2 Time-history integral approximation

The second issue to address is approximation of the first integral in (6.3), which extends to $t \to -\infty$.

The solution method assumes that, for times $t < 0$, the system remained in the bound state, and no electric field (potential) $\mathbf{A}(t < 0)$ is present, so that the solution $S(t < 0) = S_0 e^{iE_0 t}$ is known. The integral is separated into regions where the solution $S(t)$ is known ($t < 0$), and where $S(t)$ must be found ($t > 0$):

$$S(t) = \int_{-\infty}^{0} dt' K(t,t') S_0 e^{iE_0 t'} + \int_{0}^{t} dt' K(t,t') S(t'). \tag{6.21}$$

Although the form of $S(t)$ is known for $t < 0$, the first term does not yield a closed form solution for arbitrary $\mathbf{A}(t)$. We therefore separate it into an exactly solvable "field free contribution", and a field correction term:

$$S(t) = \int_{-\infty}^{0} dt' \left(K_0(t,t') + \Delta K(t,t')\right) S_0 e^{iE_0 t'} + \int_{0}^{t} dt' K(t,t') S(t'), \tag{6.22}$$

where

$$K_0(t,t') \equiv iV_0 \left(\frac{2\pi}{\alpha(t,t')}\right)^{3/2} \tag{6.23}$$

and

$$\Delta K(t,t') \equiv K(t,t') - K_0(t,t'). \tag{6.24}$$

The first term in Eq.(6.22) can be integrated to give a closed function, $S_i(t)$, while the field dependent contribution for $t < 0$ is truncated and evaluated to some chosen initial time, t_{init}:

$$S(t) = S_i(t) + \int_{t_{init}}^{0} \Delta K(t,t') S_0 e^{iE_0 t'} + \int_{0}^{t} dt' K(t,t') S(t'). \tag{6.25}$$

As with the dispersion relation, we wish to find the corresponding integral contributions for the discrete time system. The numerically corrected quantity $S_i(t)$ can be found following the same algebraic steps used to calculate the numerically corrected dispersion relation above, $D(E_0, c_j, c_k, \sigma_j, \sigma_k, \Delta t)$, with the substitution $j \to j - n$; this results in the same terms $D_n(\Delta t)$ given in Eqs (6.17 - 6.20) with the substitution $(\sigma_j^2 + \sigma_k^2) \to (\sigma_j^2 + \sigma_k^2 + i\ n\Delta t)$.

6.3 Numerical corrections for the multi-state system

The multi-state system introduced in chapter 5 can be treated with the method outlined above. The evolution equation becomes a matrix integral equation of dimension $N \times N$ for N separable potentials, for which the dispersion relation becomes:

$$D(E_n, \{c,\sigma\}, \Delta t) = \det \| \mathbb{1} - \Delta t \sum_{j=-\infty}^{0} \mathbf{K}(0, j\Delta t) e^{iE_n j\Delta t} + \frac{\Delta t}{2} \mathbf{K}(0,0) \| = 0, \tag{6.26}$$

where the symbol $\mathbb{1}$ represents the identity matrix. Each matrix element will have a series of Δt correction terms analogous to the single potential state; the form of

Eq.(6.26) remains valid for all terms in the three state case examined in chapter 5, including the polarization kernel terms. It may be pointed out here that, as the number of nonlocal potentials grows, the number of numerical correction terms that must be calculated grows rapidly ($\sim N^2$ multiplied by the desired number of correction terms), and, if the form of $u(\mathbf{k})$ are each different, quickly becomes impractical to implement.

6.4 Runge-Kutta 4th order numerical treatment

The time-dependent equation $S(t)$ may also be computed by more standard methods, such as a fourth-order accurate Runge-Kutta method (RK4), adapted to Volterra integral equations via the following scheme:

$$\begin{aligned} S(t) = S_i(t) + \frac{\Delta t}{6} \sum_{j=0}^{n-1} \Bigg(& K(n\Delta t, j\Delta t)\, Y_1 + \dots \\ & 2K\big(n\Delta t, (j+\tfrac{1}{2})\Delta t\big)\, Y_2 + \dots \\ & 2K\big(n\Delta t, (j+\tfrac{1}{2})\Delta t\big)\, Y_3 + \dots \\ & K(n\Delta t, (j+1)\Delta t)\, Y_4 \Bigg) \end{aligned} \tag{6.27}$$

where

$$\begin{aligned} Y_1 &\equiv S(j\Delta t), \\ Y_2 &\equiv S\big((j+\tfrac{1}{2})\Delta t\big) + \frac{\Delta t}{2} K\big((j+\tfrac{1}{2})\Delta t, j\Delta t\big)\, Y_1, \\ Y_3 &\equiv S\big((j+\tfrac{1}{2})\Delta t\big) + \frac{\Delta t}{2} K\big((j+\tfrac{1}{2})\Delta t, j\Delta t\big)\, Y_1, \\ Y_4 &\equiv S((j+1)\Delta t) + \Delta t K((j+1)\Delta t, j\Delta t)\, Y_1 \end{aligned}$$

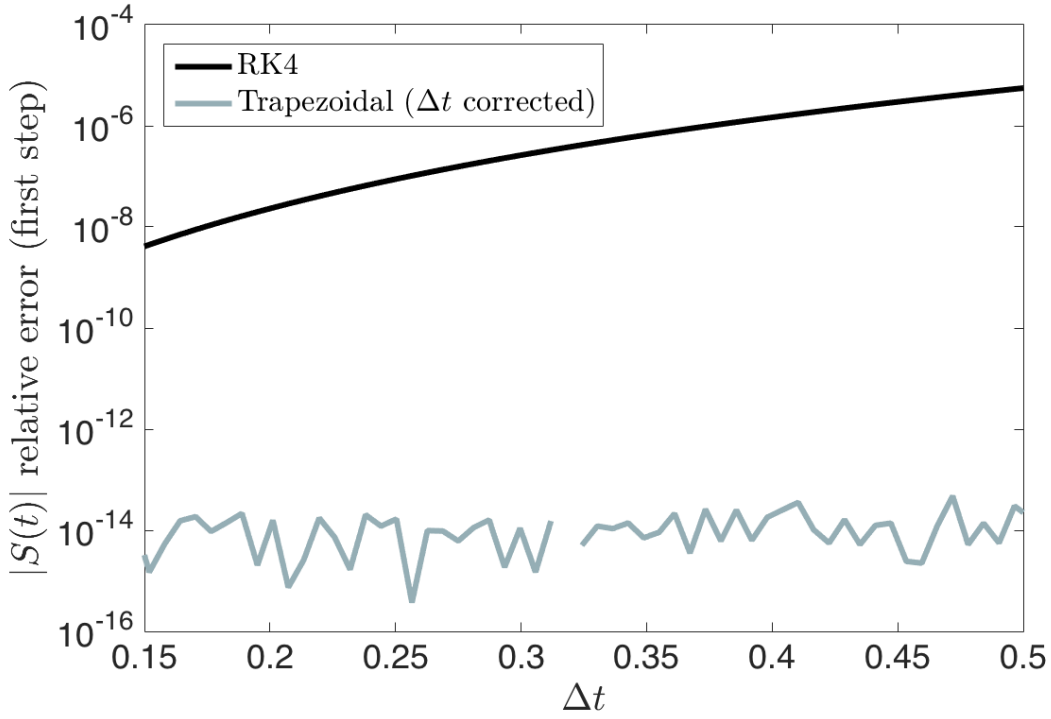

Figure 6.1: Relative error in $|S(t)|$ at the first time-step evaluation. The RK4 implementation is actually $\mathcal{O}(\Delta t^5)$ accurate: the error curve above has a polynomial fit $\alpha \Delta t^{\beta}$, for $\alpha = 0.0003562$, and $\beta = 5.995$ (r-square value of 0.999997). The trapezoidal integration included dispersion correction terms and integral contributions $S_i(t)$ up to $\mathcal{O}(\Delta t^8)$ via the expressions above. For the values of Δt plotted, $S(t)$ is machine precision limited; the largest step sizes are reasonable for computing field dependent simulations, however.

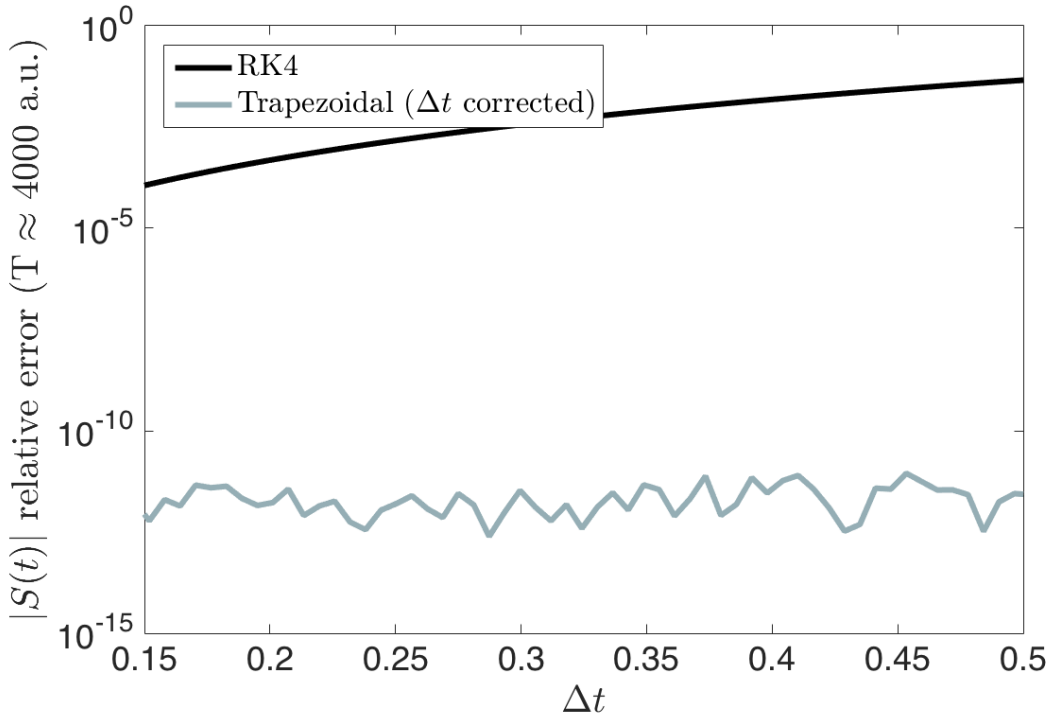

Figure 6.2: The accumulated error in $|S(t)|$ at $\sim 4000au$ is shown for field free simulation using the RK4 and dispersion corrected trapezoidal integration implementations. The modulus $|S(t)|$ shows numerical damping when the continuous time dispersion values (used with the RK4 implementation), compared with the numerically (Δt) corrected dispersion relation (used in trapezoidal implementation). for $\Delta t = 0.5$, the $|S(t)|$ has reduced by 5% for the RK4 calculation.

as found in [49]. This method is easier to implement, and more easily applied to systems that may involve more complicated $u(\mathbf{k})$, for which the method of modifying the parameters to satisfy the numerical eigenvalue equation would not be possible. Although this numerical treatment is accurate in $\mathcal{O}(\Delta t^5)$, the field free system still does not satisfy the eigenvalue equation, and will suffer numerical damping due to residual numerical error; compared with the previous method, this may be significant (see Fig. 6.2).

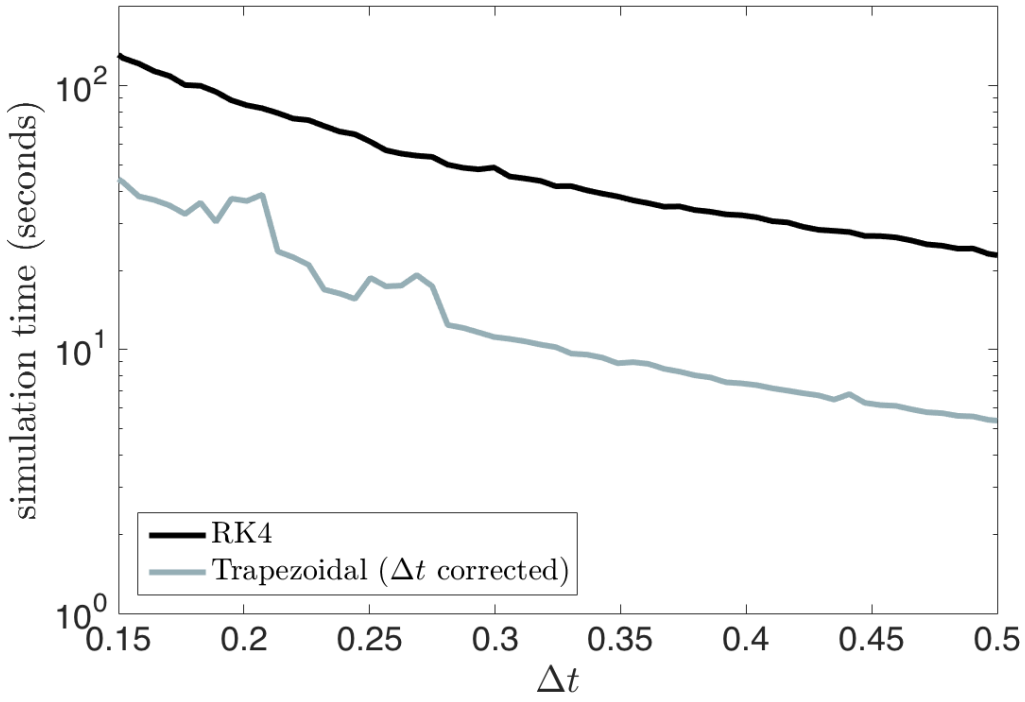

Figure 6.3: Calculation time of numerical simulation of $S(t)$ for $T \approx 4000$ au (100 fs). Simulation performed on a National Energy Research Scientific Computing Center (NERSC) "Cori" node with code written in Matlab. Similar results can be obtained on a modern desktop computer (no multi-core optimization is implemented). The RK4 implementation is between two and four times slower than the trapezoidal integration, in part due to the required half-step evaluations of the kernel. At the largest time-steps, evaluation of $S(t)$ for a 100 fs pulse can be done in ~ 5 seconds with the trapezoidal integration algorithm.

Chapter 7: Conclusion

This work examines the utility of nonlocal potentials for studying quantum mechanical laser-atom interactions in the strong-field regime. It was demonstrated that the gaussian nonlocal potential can be used to model many observed phenomena, including photo-ionization, nonlinear polarization, and photo-emission spectra.

Specifically, the single gaussian nonlocal potential model is shown to reproduce the PMPB [2] ionization rate as a function of laser frequency and intensity, spanning the multi-photon and tunnel ionization regimes in the non-relativistic and single active electron approximations. Averaged quantities such as the predicted electron bound probability $\rho(t)$ and (total) nonlinear polarization $\langle \mathbf{p}(t) \rangle$ were benchmarked against *ab initio* simulation of the time-dependent Schrödinger Equation, and later compared with *ab initio* and photocurrent model (PCM) predictions for the microscopic two-color method of THz radiation generation. The nonlocal model demonstrates improved ionization characteristics at low intensity when compared to the PCM at low intensities, for which no suitable multi-color ionization rate exists in the multi-photon regime.

The greatest observed shortcoming of the nonlocal potential appears to be due to the the short range of the gaussian, in contrast to the Coulomb potential.

Electron recollision/rescattering is thought to play a key role in determining the optimum relative phase ϕ_{rel} of the first and second harmonic pulses for generating THz radiation in the two-color model. Simulation shows that the nonlocal model and collisionless PCM give an optimal phase of ϕ_{rel} between $.35\pi - .5\pi$ at intensities above 10^{14} W cm^{-2}, while the *ab initio* gives between $.6\pi - .75\pi$.

Extensions to the gaussian nonlocal model were briefly examined, including a three potential three-eigenstate system. Although multi-state systems permit the inclusion of more physical properties, such as resonant population (Rabi-flopping) and the inclusion of angular momentum states, it becomes increasingly difficult to fit the parameter space onto desired physical properties without inducing unwanted effects. Some additional parameters without complication to the model are desirable, however; a multi-gaussian (single eigenstate) formulation was shown to permit a tunable linear polarizability and improved spectrum over the single term model when compared with *ab initio* two-color results.

The greatest value of the nonlocal model presented in this thesis is rapid evaluation of approximate strong field-atom phenomena. The method employed for calculating spatially averaged quantities (such as the total polarization $\langle \mathbf{p}(t) \rangle$ and ionization rate $\nu(t)$) include the complete evolution of the wavefunction, and thus offer a more sophisticated description than simplified photocurrent or ionization models. The nonlocal model may also be used to examine the effect of more complicated electric field response, such as multiple colors, or broadband frequency content and arbitrary laser polarization that is generally beyond the scope of ionization rate models. Although the proposed gaussian nonlocal model cannot reproduce every as-

pect of an *ab initio* treatments, quantitative agreement of the ionization rate, linear response, and qualitative characterization of several other features with significantly reduced computation time make it an appealing model for simulating strong-field laser-atom interaction.

Bibliography

[1] M. V. Ammosov, N. B. Delone, and V. P. Krainov, JetP **64**, 1191 (1986).

[2] S. V. Popruzhenko, V. D. Mur, V. S. Popov, and D. Bauer, Phys. Rev. Lett. **101**, 1 (2008), ISSN 0031-9007, 0807.2226.

[3] W. Chen, Y. Huang, C. Meng, J. Liu, Z. Zhou, D. Zhang, J. Yuan, and Z. Zhao, Phys. Rev. A **92** (2015), ISSN 10941622, 1503.07588.

[4] D. Gordon and B. Hafizi, J. Comput. Phys. **231**, 6349 (2012), ISSN 00219991.

[5] D. Strickland, G. Mourou, and o. E. Lutrr, Opt. Commun. **56** (1985).

[6] J. Krall, A. Ting, E. Esarey, and P. Sprangle, Phys. Rev. E **48**, 2157 (1993), ISSN 1063-651X, URL http://link.aps.org/doi/10.1103/PhysRevE.48.2157.

[7] M. Uiberacker, T. Uphues, M. Schultze, a. J. Verhoef, V. Yakovlev, M. F. Kling, J. Rauschenberger, N. M. Kabachnik, H. Schröder, M. Lezius, et al., Nature **446**, 627 (2007), ISSN 1476-4687, URL http://www.ncbi.nlm.nih.gov/pubmed/17410167.

[8] A. Macchi, M. Borghesi, and M. Passoni, Rev. Mod. Phys. **85**, 751 (2013), ISSN 0034-6861, URL http://link.aps.org/doi/10.1103/RevModPhys.85.751.

[9] K.-Y. Kim, J. H. Glownia, A. J. Taylor, and G. Rodriguez, Opt. Express **15**, 4577 (2007), ISSN 1094-4087.

[10] D. Zhang, Z. Lü, C. Meng, X. Du, Z. Zhou, Z. Zhao, and J. Yuan, Phys. Rev. Lett. **109**, 1 (2012), ISSN 00319007.

[11] L. A. Johnson, J. P. Palastro, T. M. Antonsen, and K. Y. Kim, Phys. Rev. A **88**, 063804 (2013), ISSN 1050-2947, URL http://link.aps.org/doi/10.1103/PhysRevA.88.063804.

[12] J. Krause, K. Schafer, and K. Kulander, Phys. Rev. Lett. **68**, 3535 (1992).

[13] M. Lewenstein, P. Balcou, M. Y. Ivanov, A. L'Huillier, P. B. Corkum, A. L'Huillier, and P. B. Corkum, Phys. Rev. A **49**, 2117 (1994), ISSN 10502947, 1106.1603, URL http://link.aps.org/doi/10.1103/PhysRevA.49.2117.

[14] F. Krausz and M. Ivanov, Rev. Mod. Phys. **81**, 163 (2009), ISSN 0034-6861, URL http://link.aps.org/doi/10.1103/RevModPhys.81.163.

[15] J. M. Dahlstrom, D. Guenot, K. Klunder, M. Gisselbrecht, J. Mauritsson, A. L'Huillier, A. Maquet, R. Taieb, M. Dahlström, D. Guenot, et al., Chem. Phys. **414**, 53 (2013), ISSN 03010104, 1112.4144.

[16] R. Potvliege, Comput. Phys. Commun. **114**, 42 (1998), ISSN 00104655, URL http://linkinghub.elsevier.com/retrieve/pii/S0010465598000733http://www.sciencedirect.com/science/article/pii/S0010465598000733.

[17] D. Bauer and P. Koval, Comput. Phys. Commun. **174**, 396 (2006), ISSN 00104655.

[18] M. K. Nazeeruddin, F. De Angelis, S. Fantacci, A. Selloni, G. Viscardi, P. Liska, S. Ito, B. Takeru, and M. Grätzel, J. Am. Chem. Soc. **127**, 16835 (2005), ISSN 0002-7863, URL http://www.ncbi.nlm.nih.gov/pubmed/16316230.

[19] R. W. Boyd, *Nonlinear Optics, Third Edition* (Academic Press, 2008), 3rd ed., ISBN 0123694701, 9780123694706.

[20] P. Sprangle, J. Peñano, and B. Hafizi, Phys. Rev. E **66**, 046418 (2002), ISSN 1063-651X, URL http://link.aps.org/doi/10.1103/PhysRevE.66.046418.

[21] A. Couairon and A. Mysyrowicz, Phys. Rep. **441**, 47 (2007), ISSN 03701573.

[22] A. Couairon, E. Brambilla, T. Corti, D. Majus, O. de J. Ramírez-Góngora, M. Kolesik, O. Ramírez-Góngora, and M. Kolesik, Eur. Phys. J. Spec. Top. **199**, 5 (2011), ISSN 1951-6355, URL http://www.springerlink.com/index/10.1140/epjst/e2011-01503-3http://link.springer.com/10.1140/epjst/e2011-01503-3.

[23] J. P. Palastro, T. M. Antonsen, and H. M. Milchberg, Phys. Rev. A **86**, 033834 (2012), ISSN 1050-2947.

[24] J. P. Palastro, Phys. Rev. A - At. Mol. Opt. Phys. **013804**, 1 (2014).

[25] M. Kolesik and J. V. Moloney, Rep. Prog. Phys. **77**, 016401 (2014), ISSN 1361-6633, URL http://www.ncbi.nlm.nih.gov/pubmed/24366913.

[26] J. D. Jackson, http://dx.doi.org/10.1119/1.19136 (1999).

[27] E. Lorin, S. Chelkowski, and A. D. Bandrauk, Commun. Comput. Phys. **9**, 406 (2011), ISSN 18152406.

[28] E. Lorin, S. Chelkowski, E. Zaoui, and A. Bandrauk, Phys. D Nonlinear Phenom. **241**, 1059 (2012), ISSN 01672789, URL http://dx.doi.org/10.1016/j.physd.2012.02.013.

[29] L. V. Keldysh, JETP **20**, 1307 (1965), ISSN 00385646.

[30] A. M. Perelomov, V. S. Popov, M. V. Terentev, and Terent'ev M. V., JETP **23**, 924 (1966).

[31] T. C. Rensink, T. M. Antonsen, J. P. Palastro, and D. F. Gordon, Phys. Rev. A - At. Mol. Opt. Phys. **89**, 1 (2014), ISSN 10502947, 1311.5600, URL http://link.aps.org/doi/10.1103/PhysRevA.89.033418.

[32] A. Teleki, E. M. Wright, and M. Kolesik, Phys. Rev. A **82**, 065801 (2010), ISSN 1050-2947.

[33] H. Kono, A. Kita, Y. Ohtsuki, and Y. Fujimura, J. Comput. Phys. **130**, 148 (1997), ISSN 00219991.

[34] N. Delone and V. Krainov, Physics-Uspekhi **42**, 669 (1999).

[35] Y. C. Han and L. B. Madsen, Phys. Rev. A - At. Mol. Opt. Phys. **81**, 063430 (2010), ISSN 10502947, URL http://link.aps.org/doi/10.1103/PhysRevA.81.063430.

[36] T. C. Rensink and T. M. A. Jr (2016).

[37] H. M. Tetchou Nganso, S. Giraud, B. Piraux, Y. V. Popov, and M. G. Kwato Njock, J. Electron Spectros. Relat. Phenomena **161**, 178 (2007), ISSN 03682048.

[38] H. M. Tetchou Nganso, Y. V. Popov, B. Piraux, J. Madroñero, and M. G. K. Njock, Phys. Rev. A **83**, 013401 (2011), ISSN 1050-2947.

[39] H. M. Tetchou Nganso, A. Hamido, M. G. Kwato Njock, Y. V. Popov, and B. Piraux, Phys. Rev. A - At. Mol. Opt. Phys. **87**, 1 (2013), ISSN 10502947.

[40] C. S. Lai, J. Phys. A Math. Gen. **16**, 181 (1983), URL http://iopscience.iop.org/0305-4470/16/6/002.

[41] P. Schwerdtfeger (2013).

[42] B. M. Karnakov, V. D. Mur, S. V. Popruzhenko, and V. S. Popov, Physics-Uspekhi **58**, 3 (2015), ISSN 1063-7869, URL http://iopscience.iop.org/article/10.3367/UFNe.0185.201501b.0003.

[43] E. E. Serebryannikov and a. M. Zheltikov, Phys. Rev. Lett. **116**, 123901 (2016), ISSN 0031-9007, URL http://journals.aps.org/prl/abstract/10.1103/PhysRevLett.116.123901.

[44] M. Tonouchi, Nat. Photonics **1**, 97 (2007), ISSN 1749-4885.

[45] J. Liu, J. D. J. Dai, S. L. C. S. L. Chin, and X.-C. Zhang, Lasers Electro-Optics Quantum Electron. Laser Sci. Conf. (QELS), 2010 Conf. **4**, 627 (2010), ISSN 1749-4885, URL http://dx.doi.org/10.1038/nphoton.2010.165.

[46] K.-Y. Kim, Phys. Plasmas **16**, 056706 (2009), ISSN 1070-664X, URL http://aip.scitation.org/doi/10.1063/1.3134422.

[47] I. Babushkin, S. Skupin, and J. Herrmann, Opt. Express **18**, 9658 (2010), ISSN 1094-4087, 1002.4582.

[48] A. N. Pfeiffer, C. Cirelli, A. S. Landsman, M. Smolarski, D. Dimitrovski, L. B. Madsen, and U. Keller, Phys. Rev. Lett. **109** (2012), ISSN 00319007, 1111.6033.

[49] E. Hairer, C. Lubich, and M. Schlichte, SIAM J. Sci. Stat. Comput. **6**, 532 (1985), ISSN 0196-5204.